Title
AN APPARATUS FOR INVESTIGATING LOW ENERGY ION-MOLECULE REACTORS AND ITS APPLICATION TO THE REACTIVE SCATTERING OF N+ BY H2

Permalink
https://escholarship.org/uc/item/26j3n56p

Author
Fair, James Alan.

Publication Date
1974-11-01

LBL-3178
c.1

AN APPARATUS FOR INVESTIGATING LOW ENERGY ION-MOLECULE REACTORS AND ITS APPLICATION TO THE REACTIVE SCATTERING OF N^+ BY H_2

James Alan Fair
(Ph. D. thesis)

November, 1974

Prepared for the U. S. Atomic Energy Commission
under Contract W-7405-ENG-48

DISCLAIMER

AN APPARATUS FOR INVESTIGATING LOW ENERGY ION-MOLECULE REACTORS AND ITS APPLICATION TO THE REACTIVE SCATTERING OF N^+ BY H_2

Contents

AN APPARATUS FOR INVESTIGATING LOW ENERGY ION-MOLECULE REACTIONS AND ITS APPLICATION TO THE REACTIVE SCATTERING OF N^+ BY H_2

James Alan Fair

Inorganic Materials Research Division, Lawrence Berkeley Laboratory
and Department of Chemistry; University of California,
Berkeley, California 94720

ABSTRACT

An apparatus was designed and constructed for measuring the scattering of ions from neutral molecules in a laboratory energy range of 6 to 50 eV. A beam of monoenergetic ions of a specified mass is generated by ionizing the parent neutral in an electron impact source and then passing the resulting ions through a magnetic momentum analyzer and electrostatic focusing system. The ion beam then passes through a collision cell which contains the neutral target molecules. The scattering ions are detected by a detection system which consists of a crossed electric and magnetic field velocity filter, a quadrupole mass filter and a magnetic electron multiplier. The primary ion source and collision cell are mounted on a rotable table in a large vacuum chamber and the detection system is mounted on the side of the vacuum chamber. This arrangement allows intensity distributions as a function of angle, mass and velocity to be determined.

The apparatus was used to study the reactive scattering of N^+ from H_2 to form NH^+. At laboratory energies above 20 eV the product intensity distribution peaked at approximately the position predicted from the spectator stripping model. As the relative energy was decreased the product intensity distribution became more symmetric around the center-of-mass and the peak intensity moved toward lower velocities until it coincided with the center-of-mass at a laboratory energy of 6.2 eV. This transition from a direct impulsive mechanism to a long-lived complex mechanism is explained by the characteristics of the electronic state correlation diagram.

I. INTRODUCTION

One of the major goals of chemical kinetics is to satisfactorily explain why chemical reactions proceed as they do. This problem was first approached by examining what happens when one ensemble of particles reacts with another ensemble of particles. In an attempt to reduce the number of experimental variables down to a manageable number, a great deal of effort has gone into the study of what happens when only one particle reacts with one other particle. The development of molecular beams has been a logical outcome of the evolution of chemical kinetics. Molecular beam techniques allow one to isolate and study bimolecular processes.

Ion-molecule reactions in the gas phase have been known to occur for many years and take place in flames in electric discharges and in space and the upper atmosphere.[1] These reactions were first studied extensively in mass spectrometers. In an effort to more effectively isolate elementary processes molecular beam techniques have more recently been applied to the study of ion-molecule reactions.

Ion-molecule reactions have been extensively studied at thermal energies in mass spectrometers. Molecular beam techniques have also been utilized to study these reactions at high laboratory energies (generally over 40 eV). At the present time little work has been done at intermediate energies. For this work an apparatus capable of studying ion-molecule reactions at energies ranging from 5 to 50 eV was designed and constructed.

The apparatus uses an electron impact source to generate ions which then pass through a magnetic momentum analyzer and a lens system in order to form a beam of ions of known mass and energy. The neutral reactants are contained in a collision cell. The primary ion source and collision cell are mounted on a rotatable table inside of a vacuum chamber. The detection system which consists of a crossed electric and magnetic field velocity filter, quadrupole mass filter and a magnetic electron multiplier is mounted on the side of the vacuum chamber. This arrangement allows ion distributions as a function of velocity, mass and angle to be determined. An attempt was made to keep the path length of the ions as short as possible in order to obtain maximum intensity. The ions were also shielded from stray electric and magnetic fields.

This apparatus was then used to examine the reactive scattering of N^+ from H_2 at laboratory energies ranging from 6 to 30 eV. The system $N^+(H_2,H)NH^+$ has been previously studied by Fehsenfeld et al.[2] at thermal energies and by Gislason et al.[3] at energies above 30 eV, but no work has been done in the intermediate energy regime.

At higher energies investigated in this project the product intensity distribution peaked at a position predicted by the spectator stripping model. As the relative energy was decreased the intensity distribution became more symmetric around ±90° in the center-of-mass reference frame with the peak intensity moving closer to the center-of-mass. At the lowest energy investigated the intensity distribution became very symmetric around ±90° with the position of maximum intensity coinciding with the center-of-mass. This symmetry around ±90° implies that the reaction probably proceeds through a long-lived intermediate complex.

The electronic state correlation diagram showing some of the predominant features of the accessible potential energy surfaces is constructed. Examination of the correlation diagram indicates two major pathways on which the

reaction may proceed. One pathway is relatively flat and leads directly to products. The other pathway yields access to a deep (6 eV) potential well which then leads to products. The probability of entering the potential well is shown to increase with decreasing energy.

II. EXPERIMENTAL

A. General Description

The basic components of the apparatus that was used in performing the experiments contained in this thesis consist of the main chamber and vacuum system, the primary ion source, the collision cell, the product ion detection train, and associated electronics. The apparatus was originally used for electron scattering from neutral molecules. The only parts of the apparatus that has remained in its original form are the main chamber and the vacuum system. Minor modifications were still made on both of these components for this work.

B. Main Chamber and Vacuum System

The main chamber and vacuum system are similar to that described by Gentry,[4] so only a brief description will be presented here. The main chamber is a box with internal dimensions of 21 in. × 21 in. (width) × 11 in. (height). A 7 in. diameter port in which various components are mounted is located in the center of each vertical face.

A 20 in. diameter hole was machined in the top of the vacuum chamber and a circular lid which was supported by a ball bearing insert was fitted into the hole. Figure 1 shows a cross sectional view of the chamber with the lid in position. A double Tec-ring seal A around the lid B provided a vacuum seal. The ball bearing C provides support for the lid and allows the lid to rotate freely when the chamber is placed under a vacuum. Also indicated is the port D for evacuating the space between the two Tec-rings with the aid of a small mechanical pump. The lid is graduated around its circumference in degrees and a vernier

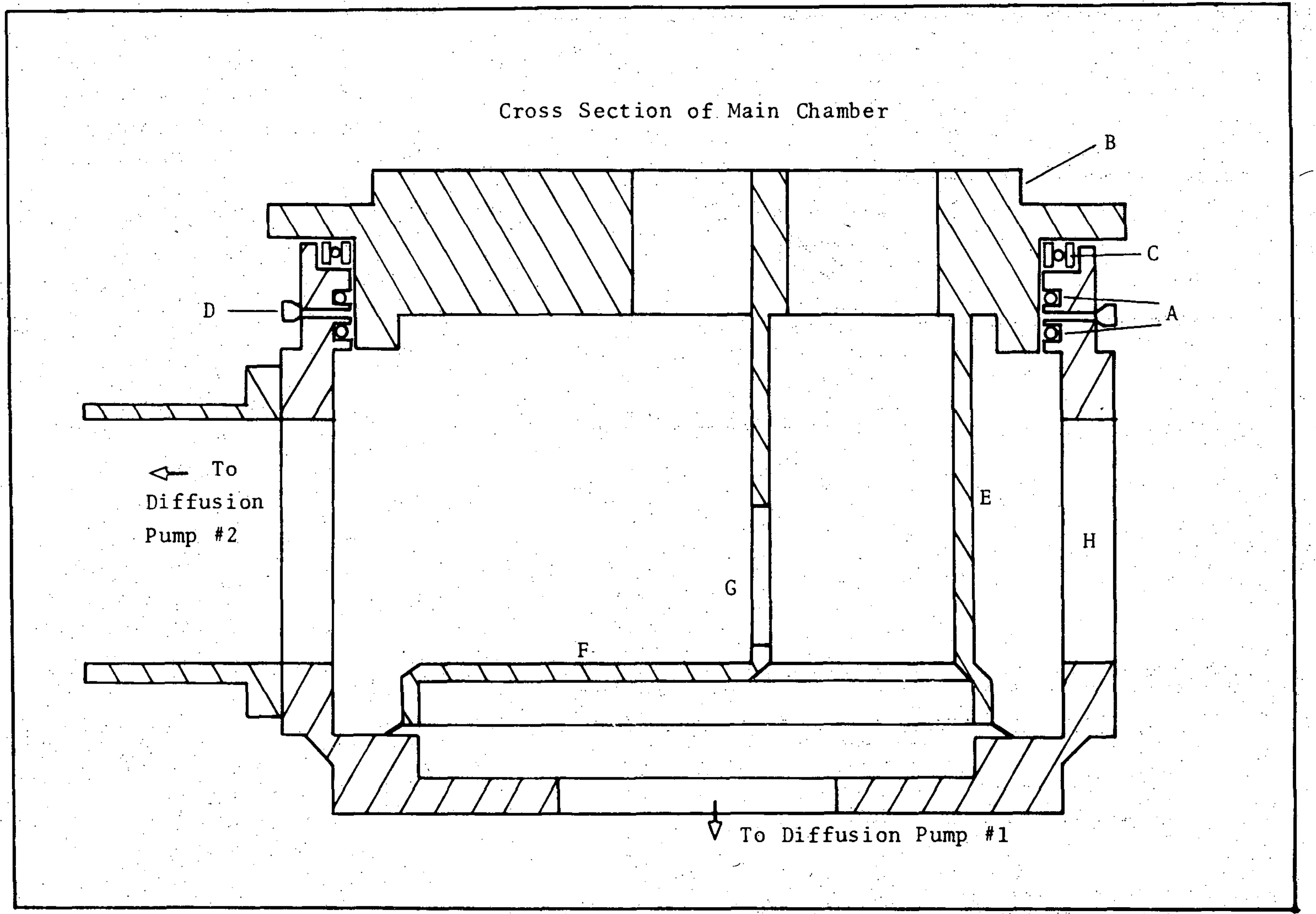

Fig. 1. A. Tec-ring seal; B. Lid; C. Ball bearing; D. Tec-Ring evacuation port; E. Pillar; F. Bottom plate; G. 4 in. square hold; H. 7 in. diameter port.

XBL 749-7243

inscribed on a ring (not shown) surrounding the lid allows accurate positioning of the lid.

The lid is connected by a hollow pillar, E, to a bottom plate, F, that is used to separate the main chamber from diffusion pump #1. The pillar allows the bottom plate to rotate along with the lid. The apparatus was originally designed to have a neutral beam mounted inside the pillar, which could be pumped separately from the main chamber. An attempt was made to mount a neutral beam source inside the pillar, but a beam of sufficient intensity to perform a scattering experiment could never be obtained. After the neutral beam components were discarded, a 4 in. square hold G was cut in the pillar, so that diffusion pump #1 could then also pump on the main chamber.

The main chamber is also pumped by diffusion pump #2, which is attached by an elbow to one of the 7 in. ports on the side of the chamber. Both diffusion pumps #1 and #2 are 6 in. NRC diffusion pumps with a liquid nitrogen cold trap between each diffusion pump and the chamber. A pumping speed of approximately 1100 liters per second is obtained by this arrangement. The output from the diffusion pumps goes to an exhaust manifold which is pumped by two mechanical pumps. A third mechanical pump evacuates the space between the two Tec-ring seals.

The pressure at various locations in the vacuum system is monitored by several thermocouple gauges. The pressure in the main chamber and pillar is monitored by two ion gauges. If the pressure in the system rises too high, an interlock system sounds an alarm and shuts off the diffusion pumps. If the pressure in the main chamber reaches an excessively high value, a second interlock shuts off any electronic components that may be damaged, e.g., the electron multiplier. If the pressure of the water that is used to cool the diffusion pumps drops or the diffusion pump temperature rises too high, then the diffusion pumps are automatically shut off.

The primary ion source is bolted onto the bottom plate (see Fig. 2) and aligned so that the ion beam crosses the center of rotation of the lid and center of the 7 in. ports. The collision cell is also located on the bottom plate and is centered about the center of rotation of the lid. The product ion detection system is mounted on one of the 7 in. ports on one of the vertical faces of the chamber. This arrangement allows the angle between the ion beam and the detector to be varied precisely, so that angular distributions may be measured.

C. Primary Ion Source

The primary ion source (Fig. 3) consists of an electron impact ion source, magnetic momentum analyzer, and various focusing elements. The location of the ion source has been described previously and is also shown in Fig. 2.

1. Electron Impact Source

The electron impact ion source is similar to one marketed by Extra Nuclear Products Corporation. Basically, the only major modification that was made in making the ion source was one of scaling it down in size, so that it would conveniently fit inside of the vacuum chamber.

The gas to be ionized enters the electron impact source through an inlet tube B into the ionization region A. Electrons are emitted from

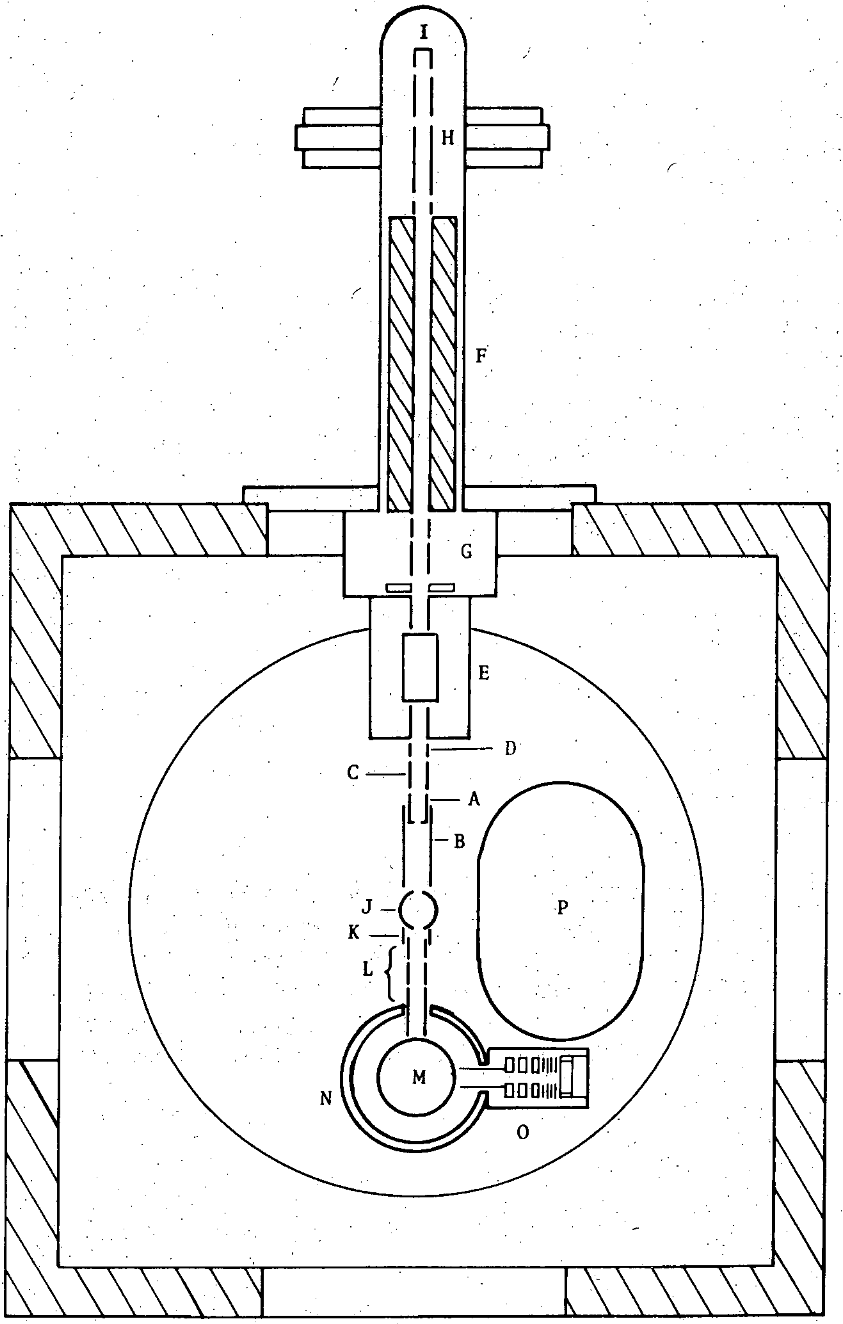

Figure 2. Top View of Vacuum Chamber and Internal Components

XBL 749-7245

Fig. 2. A. Defining aperture; B. Shield; C. Cylindrical lens element (cut into quarters); D. Lens element; E. Velocity filter; F. Mass filter; G. Intermediate focusing elements; H. Final focusing elements; I. Electron multiplier; J. Collision cell; K. Deflection plates; L. Three element lens; M. Magnet pole face; N. Momentum analyzer; O. Electron impact ion source; P. Pillar.

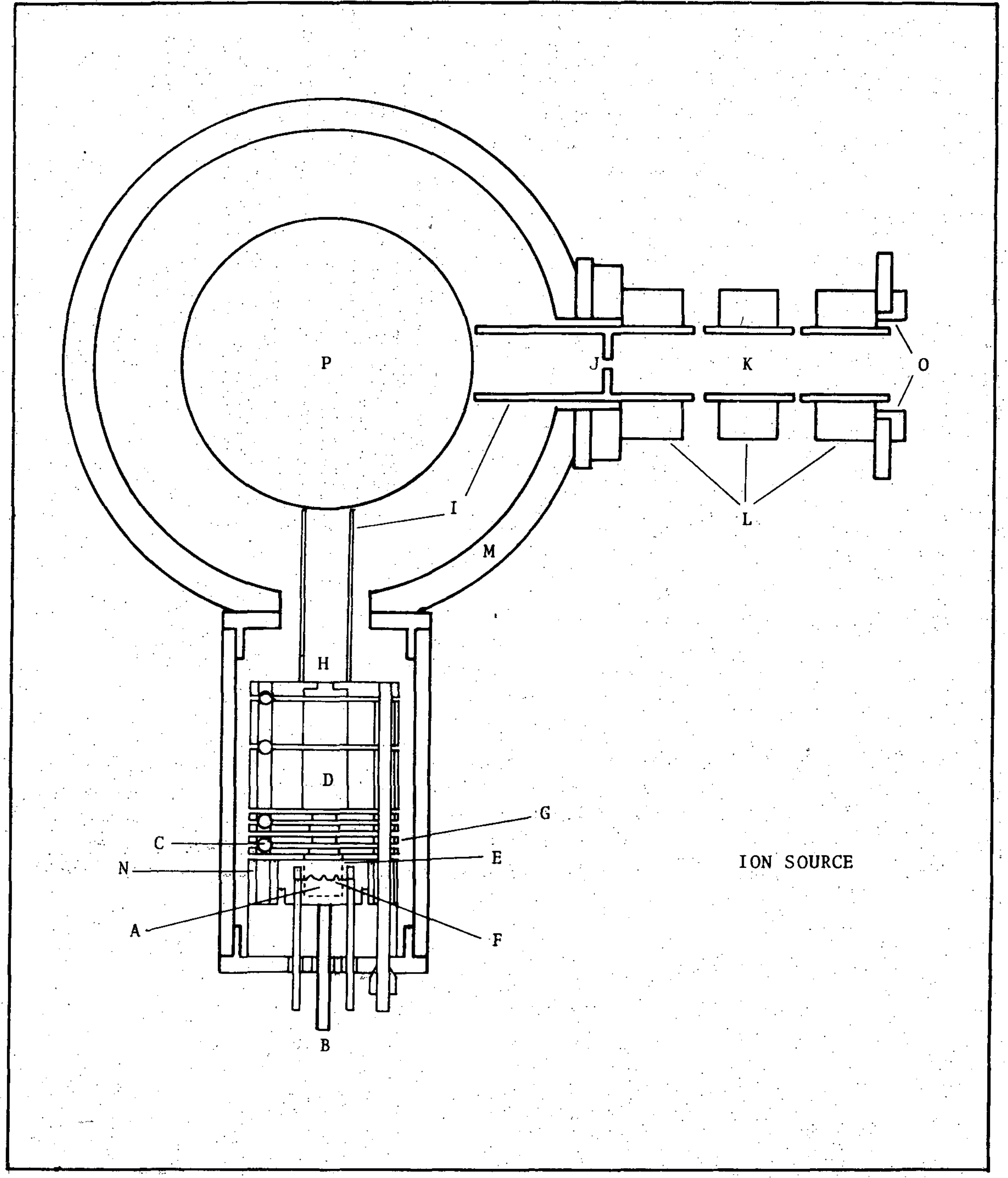

XBL 749-7246

Fig. 3. A. Ionization region; B. Gas inlet tube; C. Sapphire ball; D. Electron impact source lens elements; E. Tantalum grid; F. Tungsten filament; G. Extractor; H. Entrance aperture; I. Shield tubes; J. Exit aperture; K. Three element cylinder lens; L. Lens supports; M. Magnet yoke; N. Filament shield; O. Deflection plates; P. Magnet pole piece.

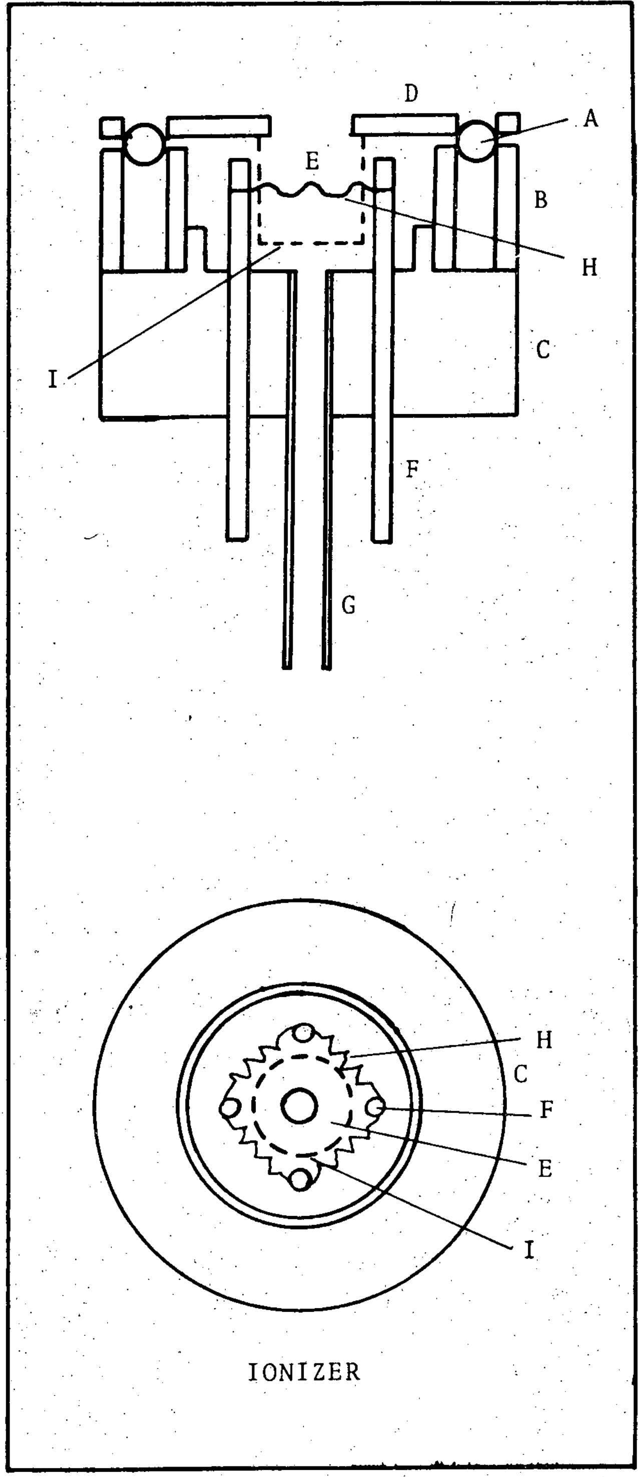

XBL 749-7247

Fig. 4. A. Sapphire ball; B. Filament shield; C. Ceramic Filament support; D. Grid support; E. Ionization region; F. Filament rod; G. Gas inlet tube; H. Filament; I. Tantalum grid.

a 0.005 in. diameter tungsten filament and are accelerated through a tantalum grid E into the ionization region where the parent gas is ionized (see also Fig. 4).

Electrons that are not used to ionize the gas then pass out through the grid and are repelled back into the ionization region by the filament shield, N, which is floated at a slightly more negative potential than that of the filament. This arrangement allows each electron to make several passes through the ionization region, which increases the effect path length of the electrons and thus the probability of ionization. The transmission of the grid is about 64%, so that only 64% of the electrons make it through the grid on each pass.

The final energy of the ions in a region of ground potential is determined by the potential of the region in which the ions are formed. The potential of the ionization region is defined by the voltage applied to the grid. For a 15 eV ion beam the grid is floated at approximately 15 volts. The larger the spread of potential in the ionization region, the larger the spread of energy that is present in the ion beam that emerges from the ionizer. The tantalum grid defines the equipotential ionization region in which the ions are formed.

The ions are extracted from the ionization region with the extractor, G, which is constructed from a 1/16 in. thick stainless steel plate. After the ions are extracted, they are focused into the entrance collimator, H, of the momentum analyzer, M, by several electrostatic lenses, D. The defining aperture in the collimator is 3 mm in diameter.

The filament of the ionizer is wound by hand around a 1 mm form, so that five turns will extend between the molybdenum filament supports.

The filament supports are mounted in a machined block of AD-99 ceramic. Accurate alignment of the focusing elements is achieved by using precision 1/8 in. sapphire balls to separate the hold the elements into place. The sapphire balls are set into 0.120 in. diameter holes. The entire ionizer assembly is mounted inside of an aluminum case, which is then bolted to the side of the momentum analyzer.

2. Momentum Analyzer

The main purpose of the momentum analyzer is to separate the various masses that are present in the ion beam that emerges from the electron impact source. For example, $^{14}N^+$, $^{15}N^+$ and N_2^+ were observed to be present in the original beam that was obtained by using N_2 as the parent gas. With the aid of the momentum analyzer it was possible to separate all of the above ions. The $^{14}N^+$ was then used for the experiments in this thesis.

The momentum analyzer was similar to one described by Kerwin[5] and was essentially just a magnetic mass spectrometer. It was required that the magnet produce a reasonably strong, variable, uniform magnetic field in the region between the pole faces with a very small field extending beyond the magnet itself. Another requirement was that the region containing the magnetic field be able to be floated at a variable potential. This potential, as well as the magnetic field, must then be shielded from the rest of the apparatus.

The assembled analyzer is shown in Fig. 5a. Each pole piece was wound with 250 turns of #18 enameled copper wire. The coils were then embedded in epoxy resin. A magnetic field that was continuously variable from 100 to 4100 Gauss was thus obtained. The magnet coils,

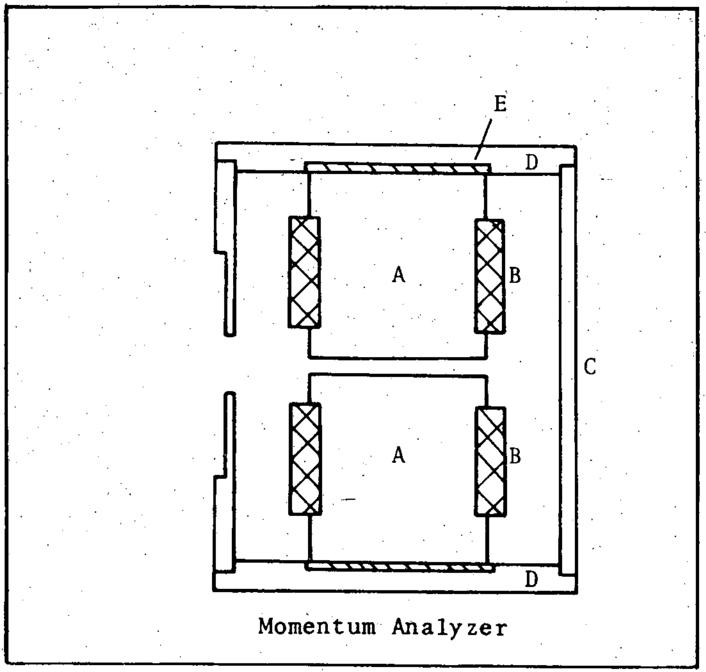

Fig. 5a. A. Pole piece; B. Electromagnet windings; C. Yoke; D. End cap; E. NEMA G-10 insulator.

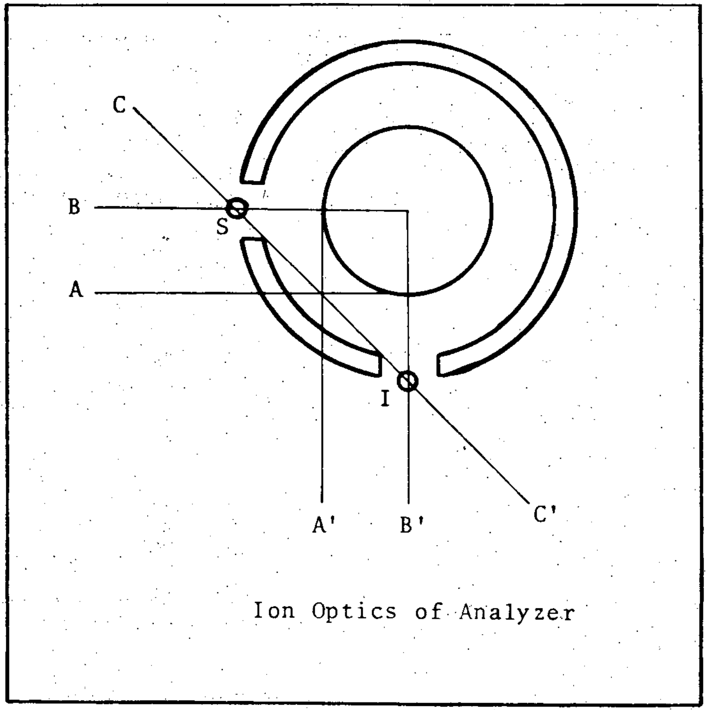

XBL 749-7248

Fig. 5b. Lines A and A' tangent to the magnetic field cross at the field apex. Source S and image I are located symmetrically around the field apex on straight line C-C'.

which could be connected in either a parallel or series configuration, were usually wired in parallel for this work. More current was drawn in the parallel configuration as compared to the series configuration for the same magnetic field. The power supply that was used to drive the magnet coils was more stable at the higher current settings.

The pole pieces, A, end caps, D, and yoke, C, were made out of low carbon steel (1010 or better) and plated with gold to prevent oxidation of the steel, when it was exposed to the atmosphere. Another reason for plating the steel was to ensure equipotential conditions between the poles. The pole pieces were insulated from the end caps with a disk of NEMA G-10, so that the pole pieces could be floated at a variable potential. The end caps and yoke were always grounded to prevent the electric field from the pole pieces from interferring with the rest of the apparatus.

The entrance and exit apertures were mounted inside of stainless steel tubes that extend right up to the pole pieces (see Figs. 2 and 3). The stainless steel tubes allowed a uniform potential to be maintained throughout the entire analysis region and prevented the ground potential of the yokes and end caps from interferring with the ion beam, while still allowing any magnetic field to penetrate freely. The tubes were constructed from type 304 non-magnetic stainless steel.

The spread of the ion beam (see Section II-G) varied from a minimum of 0.45 eV to a maximum of 0.68 eV (FWHM), if the entrance and exit apertures of the momentum analyzer were varied an order of magnitude in size. The maximum size of the entrance aperture was 1.5 mm and the maximum size of the exit aperture was 3 mm. This relative independence of the ion beam spread from aperture size implied that the source and image sizes of the momentum analyzer were not really determined by the actual physical entrance and exit aperture sizes. In order for this situation to occur the source and image sizes would have to be virtual images determined by the focusing properties of the ion lenses. The actual source size was probably determined by the focus of the aperture of the grid support of the ionizer onto the entrance aperture of the momentum analyzer. The image size of the analyzer was probably determined by the focus of the analyzer image onto the defining aperture of the collision cell.

For normal operation the large entrance and exit apertures were used and a spread of 0.68 eV in the primary ion beam was obtained. The maximum mass resolution of the analyzer was estimated to be about 15-20. This resolution was just sufficient to effectively separate mass 14 from mass 15.

Due to the shape of the pole pieces, the magnet has approximately the focusing properties of a normal circle prism lens.[6] The magnet has two foci which are placed symmetrically around the effective magnetic field. The positions of the foci are shown in Fig. 5b, where R is the radius of the magnetic field and S and I are the source and image, respectively. The foci are separated by 90° and are located at twice the radius of the magnetic field out from the center of the magnetic field.

3. Focusing System

The final focusing of the ion beam was accomplished by a three element cylindrical electrostatic lens. Originally, a series of aperture lenses was mounted between the momentum analyzer and the collision cell. However, aperture lenses have smaller diameter openings than cylinder lenses, so it was determined that a beam of greater intensity could be formed using large diameter cylinder lenses. The purpose of this lens system was to convert the ion beam which passes through a focus at the exit aperture of the momentum analyzer to a parallel beam with a focus at infinity. It was necessary to achieve these focusing conditions irrespective of the initial energy of the ions.

The design of the cylinder lens was based on a paper by Heddle.[7] The three elements of the cylinder lens K are shown in Fig. 3. The lens elements were mounted in Plexiglas insulators, L, which were mounted on brass rods that were fastened to the magnet yoke. The three lens elements were fabricated from 1/2 in. I.D. type 304 stainless steel tubes with a 1/16 in. wall thickness. There is a separation of 0.050 in. between each lens element. A 1.5 mm exit slit, J, for the momentum analyzer was mounted inside the first lens element. The first lense element was made to extend all the way up to the magnet pole face and was floated at the same potential as the magnetic pole pieces. This enabled the ion beam to be shielded from any stray electric fields, such as that from the magnet yoke, which may be present.

The last lens element was grounded. The middle lens element was floated at a variable potential. The potential of the middle lens was varied in order to obtain maximum intensity of the beam at the detector.

In order to prevent surface charges from building up on the various lens elements, all the lens elements were coated with a solution of colloidal graphite which is marketed under the name Aquadag.

A set of vertical and horizontal deflection plates, O, were mounted after the last lens element. The deflection plates were used to center the beam on the entrance aperture of the collision cell. The potentials applied to the deflection plates were centered around ground. In later experiments the deflection plates were used to chop the primary beam, so that a time-of-flight spectrum could be obtained.

D. Collision Cell

The collision cell was mounted in the center of the chamber, so that the center of rotation of the collision cell coincided with the center of rotation of the lid. A diagram of the collision cell is shown in Fig. 6. The entrance aperture, which was also used as the defining aperture for the main beam, was 1.5 mm in diameter. The exit aperture for the collision cell was a horizontal slit which was 1.5 mm high and extended for 17° to each side of the axis of the main beam. The diameter of the collision cell was 32 mm. The interior of the cell was also coated with a solution of colloidal graphite to prevent the build-up of surface charges.

The scattering gas was admitted to the collision cell through a stainless steel inlet tube fastened to the top of the cell. The gas inlet tube entered the vacuum chamber through the lid and the flow was controlled by a Granville-Phillips variable leak valve. All the gases used for the experiments came from a gas cylinder, with the exception of

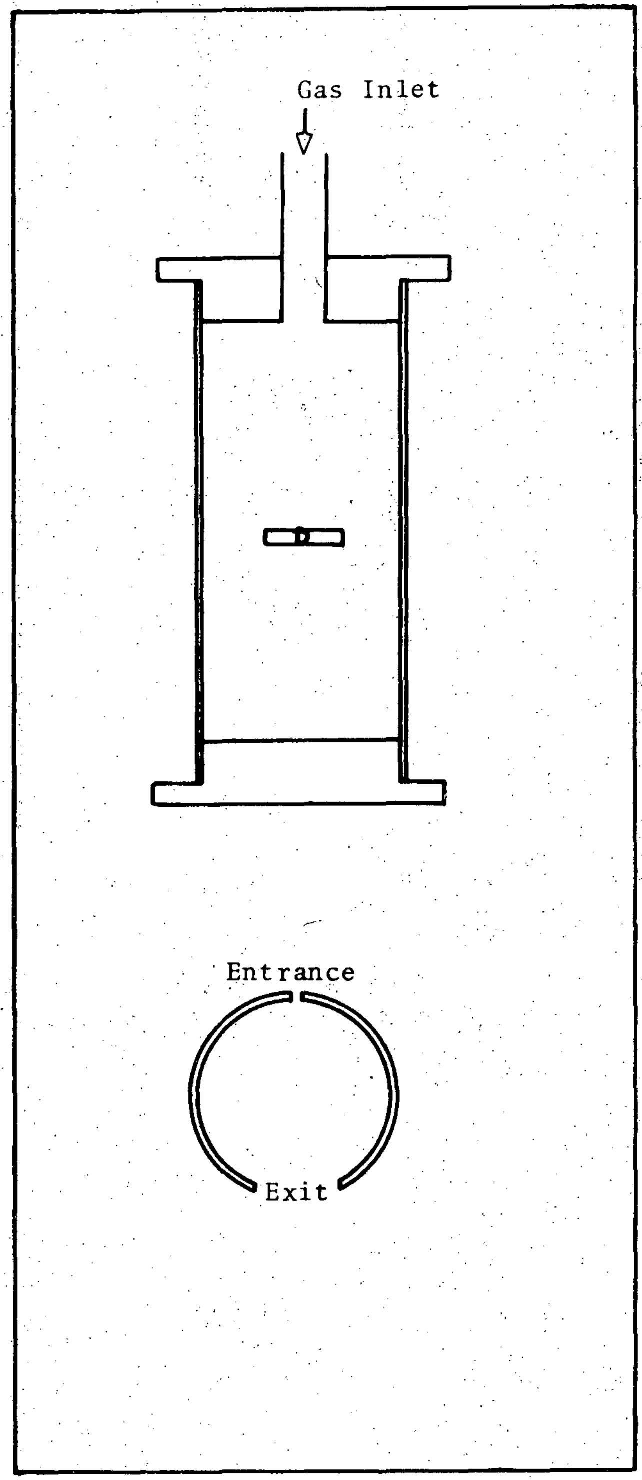

XBL 749-7249

Fig. 6. Collision cell.

HD which was obtained from a glass bulb.

The pressure in the inlet line to the cell was measured with a capacitance manometer. The manometer was attached to the gas supply line where it entered the lid on top of the vacuum chamber. The actual pressure in the collision cell was calculated from the pressure at the manometer and the conductance of the line between the manometer and the collision cell. The conductance of the line and collision cell was calculated by using various formulas given in Dushman and Lafferty.[8] Once the pressure in the cell was known, the variable leak valve was calibrated, so that in the future the pressure in the cell could be determined from the setting of the variable valve. The calibration was performed using hydrogen as the gas in the collision cell. Most of the experiments in this thesis were performed at a pressure of 1-2 microns in the collision cell.

E. Product Ion Detection System

1. General Description

The product ion detection system is fastened to one of the 7 in. ports on the side of the main chamber, so that it is stationary, whereas the source and collision cell can be rotated. This arrangement allows the measurement of angular distributions for scattering events. The detection system consists of several discrete components which are a velocity filter, a quadrupole mass filter, and an electron multiplier through which the ions pass in the same order. These components are linked together by a series of electrostatic ion lenses.

2. Velocity Filter

The velocity filter is a variation of a Wien filter type, which consists of crossed electric and magnetic fields. A similar filter has been used as an electron velocity filter by Legler.[9]

a. Theory. The electric field of the velocity filter is formed by two cylindrical electrodes of radius r_1 and r_2 (see Fig. 7). V is the potential at various points between the cylindrical elements.

$$V(x,y) = E_o\, a\left\{\frac{x}{a} - \frac{1}{2}\left(\frac{x}{a}\right)^2 + \frac{1}{2}\left(\frac{y}{a}\right)^2 + C\left[\frac{1}{3}\left(\frac{x}{a}\right)^3 - \frac{xy^2}{a^3}\right]\right\} \quad . \tag{1}$$

E_o is the field strength along the z axis and a is the radius of curvature of the equipotential surface that contains the z axis. The coordinate system is defined in Fig. 7. Equation 1 can be derived by expanding V in a power series of x and y and applying Laplace's equation and the boundary conditions of the cylindrical electrodes. The radius of curvature ρ of the equipotential surfaces is related to the constant C by Eq. (2).

$$\frac{\partial\rho}{\partial x} = 2C - 1 \quad . \tag{2}$$

For a series of concentric equipotentials $C = +1$.

The equation of motion of a charged particle in crossed electric and magnetic fields is

$$\ddot{r} = -\frac{e}{m}\,(E + \dot{r}xB) \quad . \tag{3}$$

where r is the position vector of the particle, E the electric field, and B the magnetic field. Given the conditions that the magnetic field

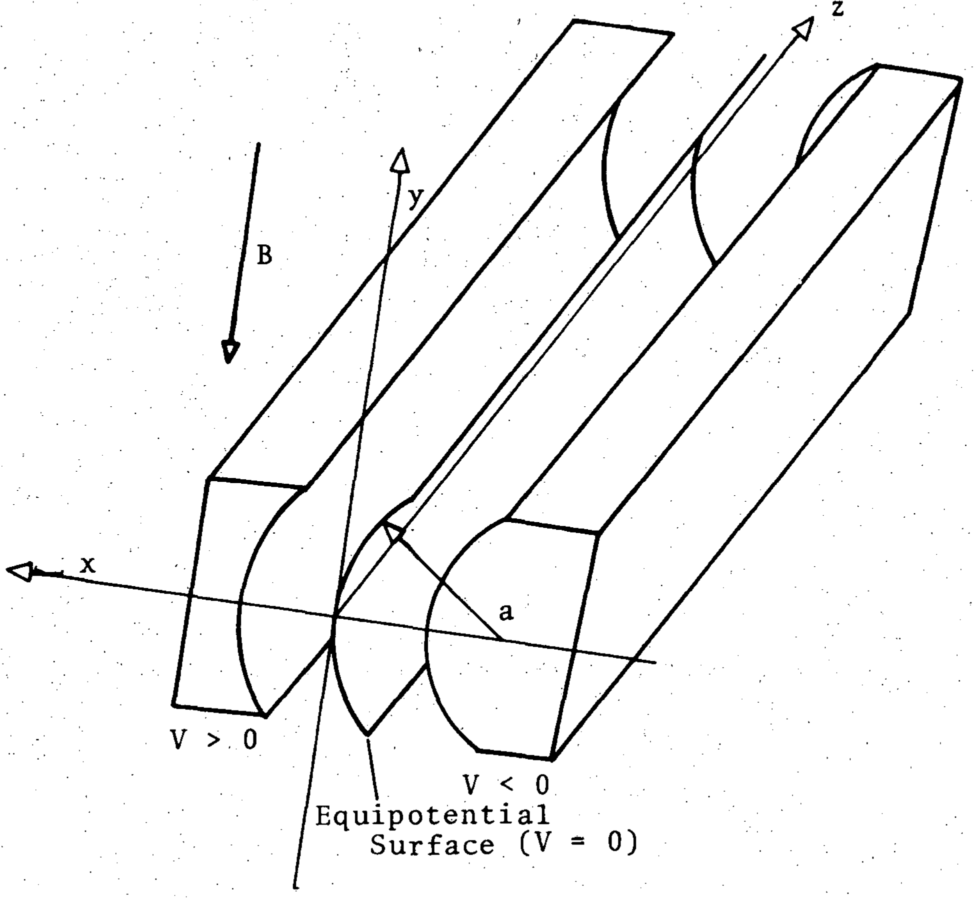

XBL 749-7250

Fig. 7. Velocity filter electrodes.

points in the y direction and the electric field points in the x direction, then a particle with an initial velocity v_o along the z axis (optical axis) will continue to move along the z axis with its velocity unchanged, if

$$B = \frac{E_o}{v_o} \tag{4}$$

The magnetic field implies a cyclotron frequency, $\omega_o = \frac{e}{m} B$.

By taking partial derivatives of V, the electric field components in the x and y directions may be determined

$$E_x = -E_o \left\{ 1 - \frac{x}{a} + C\left[\left(\frac{x}{a}\right)^2 - \left(\frac{y}{a}\right)^2\right] \right\} \tag{5}$$

$$E_y = -E_o \left\{ \frac{y}{a} - 2C\,\frac{xy}{a^2} \right\} \quad . \tag{6}$$

From the above electric field components, the complete equations of motion may be obtained.

$$\ddot{x} = -\omega_o v_o \left\{ 1 - \frac{x}{a} + C\left[\left(\frac{x}{a}\right)^2 - \left(\frac{y}{a}\right)^2\right] \right\} + \omega_o \dot{z} \tag{7}$$

$$\ddot{y} = -\omega_o v_o \left\{ \frac{y}{a} - 2C\,\frac{xy}{a^2} \right\} \tag{8}$$

$$\ddot{z} = +\omega_o \dot{x} \quad . \tag{9}$$

In order to proceed further, the entrance aperture is placed at $x = y = z = 0$ and the particle passes the entrance aperture at $t = 0$. If the ion beam enters the filter in the z direction as a cone of half angle α, then

$$\dot{z}(0) = \frac{v_o}{\sqrt{1 + \alpha^2}} \simeq v_o \tag{10}$$

and integration of Eq. (9) immediately yields

$$\dot{z} = v_o - \omega_o x \quad . \tag{11}$$

To first order in x and y, Eqs. (7) and (8) reduce to

$$\ddot{x} + \omega_o\left(\omega_o - \frac{v_o}{a}\right) x = 0 \tag{12}$$

$$\ddot{y} + \omega_o\left(\frac{v_o}{a}\right) y = 0 \quad . \tag{13}$$

Solution of the equations of motion shows that there is a harmonic oscillation about the z axis in the x and y directions. For simultaneous focusing in both the x and y directions at the same time requires that both frequencies of oscillation ω be the same, so

$$\omega^2 = \omega_o\left(\omega_o - \frac{v_o}{a}\right) = \frac{\omega_o v_o}{a} \qquad \omega_o = \omega_o/\sqrt{2} \quad . \tag{14}$$

It can be seen now that directional focusing may be obtained in both the x and y directions with this type of velocity filter. If the equations of motion for a conventional Wien filter, which has plane electrodes instead of cylindrical electrodes, are solved, it is observed that there can be focusing in only the x direction and none in the y direction.[10]

In the velocity filter described here the radius of curvature of the V = 0 equipotential surface can then be calculated by

$$a = \frac{2v_o}{\omega_o} = 4\,\frac{U_o}{E_o} \quad , \tag{15}$$

where U_o is the initial energy of the ions. The first focusing point occurs after 1/2 an oscillation, or at $t = \frac{\pi}{\omega}$. The focusing distance ℓ can then be solved for,

$$\ell = \frac{\pi a}{\sqrt{2}} = \sqrt{2}\ \pi\left(\frac{m}{e}\right)\frac{E_o}{B^2} \quad . \tag{16}$$

The electrode separation may be calculated from integration of Eqs. (12) and (13) and the half angle α;

$$\bar{r}_{max} = \alpha a/\sqrt{2} \quad . \tag{17}$$

The energy dispersion of a particle of $e\Delta U$ away from the tuned energy eU_o may be calculated by solving the equations of motion to first order, subject to the following boundary condition,

$$\dot{z}(0) = v_o\left(1 + \frac{1}{2}\ \frac{\Delta U}{U_o}\right) \quad . \tag{18}$$

Integration of Eq. (9) then gives

$$\dot{z} = v_o\left(1 + \frac{1}{2}\ \frac{\Delta U}{U_o}\right) - \omega_o x \tag{19}$$

Equations (7) and (8) then become

$$\ddot{x} + \omega^2\left(x - \frac{a}{2}\ \frac{\Delta U}{U_o}\right) = 0 \tag{20}$$

$$\ddot{y} + \omega^2 y = 0 \quad . \tag{21}$$

The solutions of the equations of motion indicate that the particle now oscillates about an axis which is displaced from the optical axis by a $\Delta U/2U_o$ in the x-direction (see Fig. 8). The exit plane is reached in

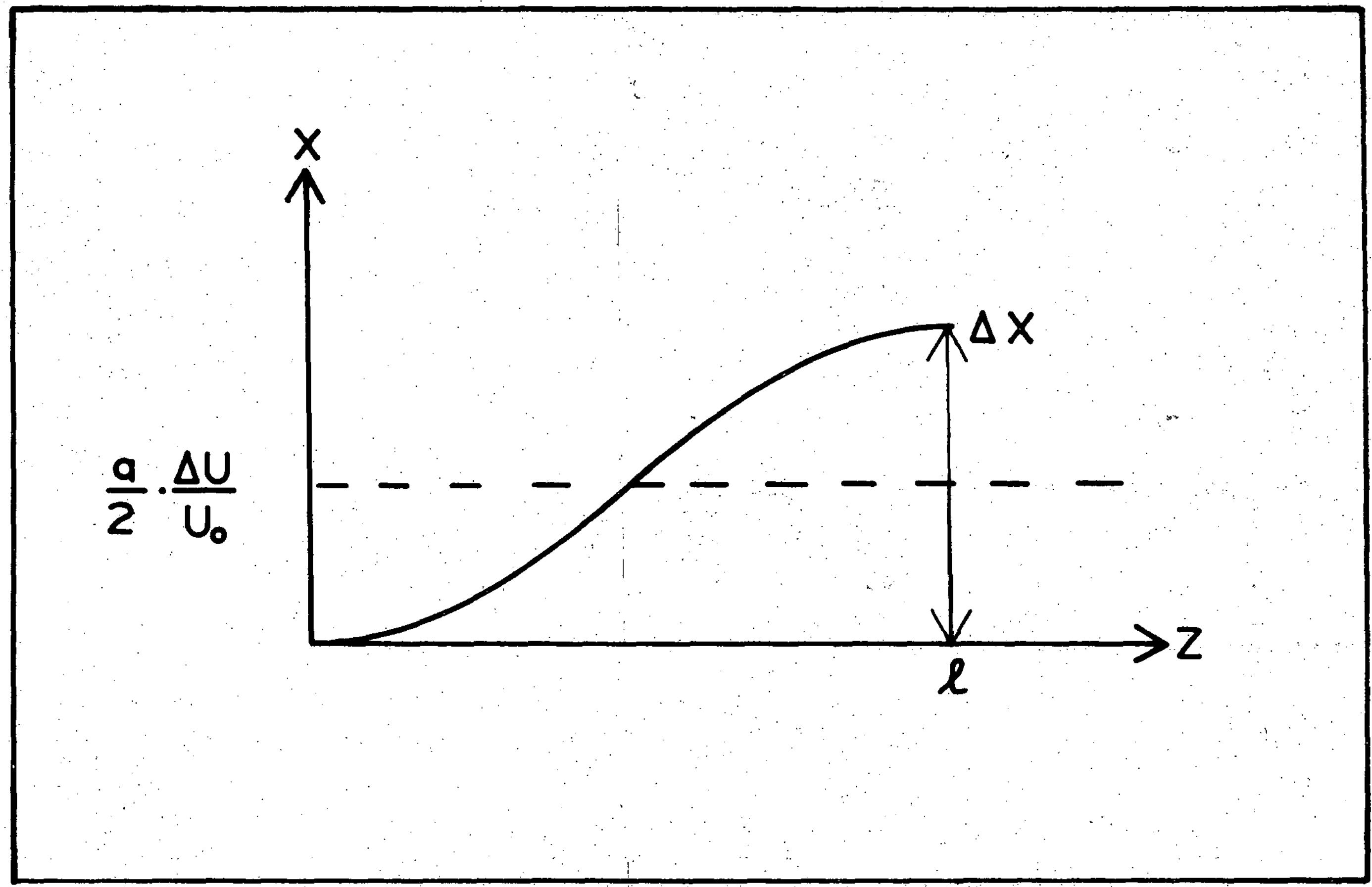

XBL 749-7244

Fig. 8. Energy dispersion.

$\frac{1}{2}$ an oscillation, so the particle, so the particle has been displaced from the optical axis by $(a\cdot\Delta U)/U_o$. The direction of dispersion is in the same direction as the electric field and the energy dispersion may be calculated directly,

$$D = \frac{\Delta X}{\Delta U} = \frac{a}{U_o} \quad . \tag{22}$$

In order to find where particles of initial energy U_o and filling a cone of half angle α strike the exit plane, the equations of motion must be solved to second order. The extreme rays of the cone make an angle α with the optical axis and have an azimuthal angle ψ with respect to the x axis. The initial velocity conditions of the particles in question are

$$\dot{x}(0) = v_o \cos\psi \quad ,$$

$$\dot{y}(0) = v_o \sin\psi$$

and

$$\dot{z}(0) = v_o\left(1 - \frac{1}{2}\alpha^2\right) \quad . \tag{23}$$

Equation (9) can be integrated directly to give

$$\dot{z} = v_o\left(1 - \frac{1}{2}\alpha^2\right) - \omega_o x \quad . \tag{24}$$

The complete equations of motion in the x and y coordinates are now

$$\ddot{x} + \omega^2 x = -\omega^2 a\left\{\frac{x^2}{2} + C\left[\left(\frac{x}{a}\right)^2 - \left(\frac{y}{a}\right)^2\right]\right\} \tag{25}$$

$$\ddot{y} + \omega^2 y = \omega^2 a \cdot \frac{2Cx}{a} \cdot \frac{y}{a} \quad . \tag{26}$$

In order to obtain a solution for Eqs. (25) and (26), the first approximation of

$$x = \frac{a\alpha}{\sqrt{2}} \cos\psi \sin\omega t$$

and

$$y = \frac{a\alpha}{\sqrt{2}} \sin\psi \sin\omega t \tag{27}$$

will be substituted in the right hand side of Eqs. (25) and (26) to obtain the separated equations of motion.

$$\ddot{x} + \omega^2 x = -\omega^2 a \cdot \frac{\alpha^2}{2} \{1 + C \cos 2\psi \sin^2 \omega t\} \tag{28}$$

$$\ddot{y} + \omega^2 y = \omega^2 \frac{a\alpha^2}{22} C \sin 2\psi \sin^2 \omega t \quad . \tag{29}$$

The time at which the particles pass ℓ may be obtained by using a first approximation for x and integrating Eq. (24) to get

$$v_o\left(1 - \frac{1}{2}\alpha^2\right) t - a\alpha \cos\psi(1 - \cos\omega t) = \ell = \frac{\pi a}{\sqrt{2}} \quad . \tag{30}$$

Solving Eq. (30) for t yields

$$t = \frac{1}{\omega} (\pi + 2\sqrt{2}\, \alpha \cos\psi) \quad . \tag{31}$$

The solutions of the equations of motion at time t gives the displacements in Δx and Δy.

$$\Delta x = -a\alpha^2 \left\{2 + \left(1 + \frac{2C}{3}\right) \cos 2\psi\right\} \tag{32}$$

$$\Delta y = -a\alpha^2 \left(1 - \frac{2C}{3}\right) \sin 2\psi \quad . \tag{33}$$

The boundary rays make an ellipse at the exit plane, whose center lies at $x = -2a\alpha^2$. If C is greater than 0, the ellipse is the x direction; if C is less than 0 the ellipse is in the y direction; if C is equal to 0, a circle is obtained (see Fig. 9). If the aperture error is characterized by the middle point location, $2\ a\alpha^2$, of the ellipse, the ultimate resolution is limited by

$$\frac{\Delta U}{U} = 2\alpha^2 \quad . \tag{34}$$

b. Construction. The location of the velocity filter is shown in Fig. 2. The filter is mounted inside of a mild steel box in order to contain the magnetic field. This prevents the production of stray magnetic fields throughout the rest of the apparatus which could possibly interfer with the normal operation of the other components that are present in the apparatus.

The magnetic field is produced by two 225 turn coils of enameled copper wire, which are then epoxied into position around the pole pieces. By this technique a magnetic field that is continuously variable between 0 and 1000 Gauss is generated. Steel tubes, which are used to shield the ions from the fringing magnetic field until they reach the analysis region, extend up to the pole pieces.

The cylindrical electrodes are mounted between the pole faces and extend the length of the pole pieces. The positive electrode has a radius of curvature 21.5 mm and the negative electrode has a radius of curvature of 25.4 mm. The electrodes are separated by 5 mm at the center.

Entrance and exit apertures are mounted on the outside of the steel box. Originally an aperture size of 1.5 mm was used, but it was later

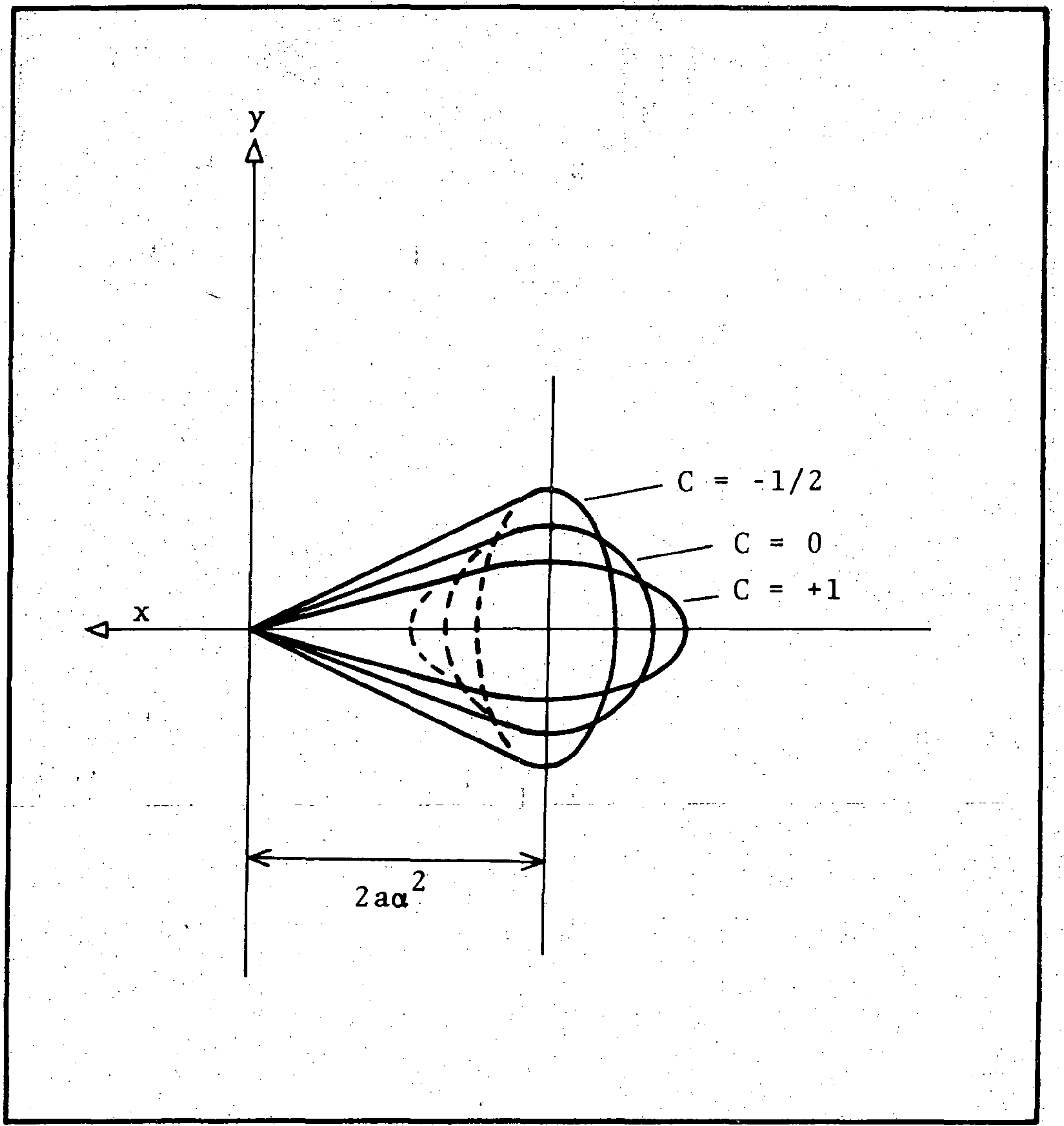

XBL 749-7252

Fig. 9. Aperture error.

determined that the aperture size could be increased to 12 mm without appreciably affecting the resolution. The intensity increased significantly with increasing aperture size.

The independence of resolution from aperture size implies that there are virtual apertures on the velocity filter other than real apertures. The entrance aperture is defined by the image that is formed by the focus of the ion lenses on the exit aperture of the collision cell. The exit aperture of the velocity filter is likewise defined by the image that is formed by focusing on the entrance of the mass filter.

3. Mass Filter

After the ions pass through the velocity filter, they are focused onto the entrance of the quadrupole mass filter. The function of the mass filter is to remove all ions except those of a particular $\frac{e}{m}$ ratio.

The mass filter that was used in this experiment is of the same design as that used by Wilson[11] and is described in detail in that work. The operation of the quadrupole depends on the superposition of steady and alternating electric fields upon four hyperbolic cylinders.

The generalized potential for a quadrupole field[6] is

$$\phi = U(t)(ax^2 + by^2 + cz^2) \tag{35}$$

where U(t) is a time dependent potential (see Fig. 10). By applying Laplace's equation $\nabla^2\phi = 0$, the relationship between the constants a, b and c are obtained.

$$a + b + c = 0 \quad . \tag{36}$$

For a cylindrical hyperbolic electric field that lies in the z direction,

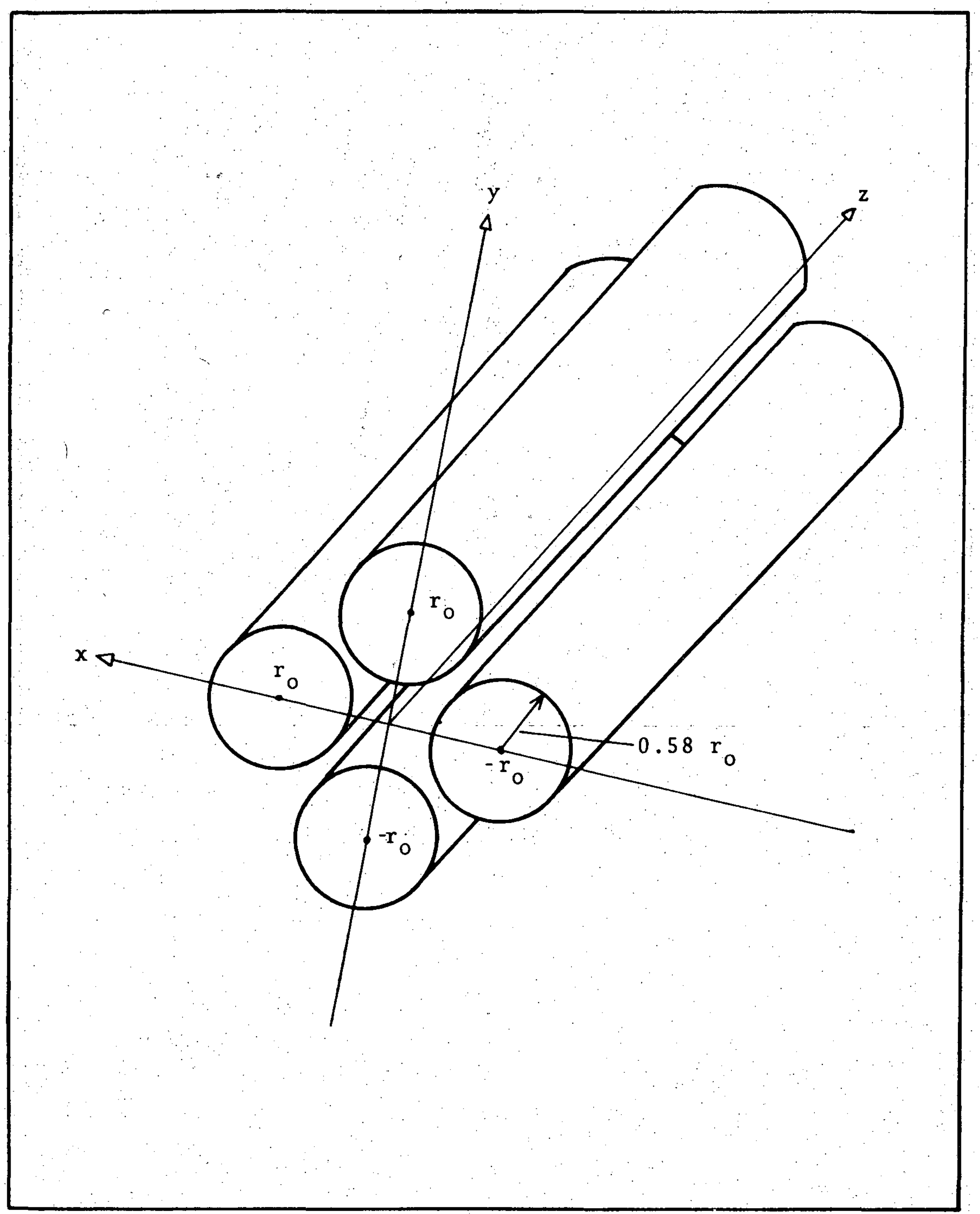

XBL 749-7253

Fig. 10. Quadrupole mass filter.

$$c = 0 \tag{37a}$$

$$a = -b \quad . \tag{37b}$$

A cylindrical hyperbolic field may be approximated by four parallel rods of circular cross section with opposite rods $2r_o$ apart. The best approximation to an ideal hyperbolic field with cylindrical pole pieces is accomplished by using rods with a radius of $0.58\ r_o$, which then makes

$$a = \frac{1}{r_o^2} \tag{38a}$$

$$b = \frac{1}{r_o^2} \quad . \tag{38b}$$

For an applied potential difference of $U + V\cos\omega t$

$$\phi = (U + V\cos\omega t)\ \frac{x^2 - y^2}{r_o^2} \tag{39}$$

The equations of motion for a particle of mass m and charge e then become

$$\ddot{x} - \frac{2e}{mr_o^2}(U + V\cos\omega t)\ x = 0 \tag{40}$$

$$\ddot{y} + \frac{2e}{mr_o^2}(U + V\cos\omega t)\ y = 0 \tag{41}$$

$$\ddot{z} = 0 \quad . \tag{42}$$

The above equations of motion are special cases of Mathieu's differential equations.[12] Two solutions exist; one of these corresponds to an ion with an exponentially increasing amplitude of oscillation which results in the ion being collected on one of the four cylinders. The other solution describes an ion with a stable oscillation that passes all the way through the mass filter with a constant velocity along the axis of the filter. Only the ions which fall into a small range of $\frac{e}{m}$ ratios form stable oscillations.

4. Detector

After the ions leave the quadrupole mass filter, they are accelerated by a series of lens elements into the detector. The detector is a Model 306 Bendix magnetic electron multiplier.[13]

A magnetic electron multiplier utilizes a strip of semiconductive metallic oxide rather than the more conventional multielement dynode design. The basic part of the multiplier consists of two glass plates which are coated with a semiconductive material. The plates, which are separated by a few millimeters (see Fig. 11), have the same potential difference of approximately 1800 volts applied along their long dimension. The field strip is floated about 200 volts positive to the dynode strip, which causes the equipotential lines in the volume between the surfaces to be parallel to each other and have the direction indicated in Fig. 11. The entire assembly is placed in a uniform magnetic field perpendicular to the plane of the figure.

An electron that is released from any point along the dynode strip follows a cycloidal motion down the strip, until it strikes the dynode strip again. Every time an electron strikes the strip, several electrons are emitted from the strip. This process occurs again for each electron emitted. The electrons emitted in this fashion are finally collected as a current pulse on a collector at the end of the

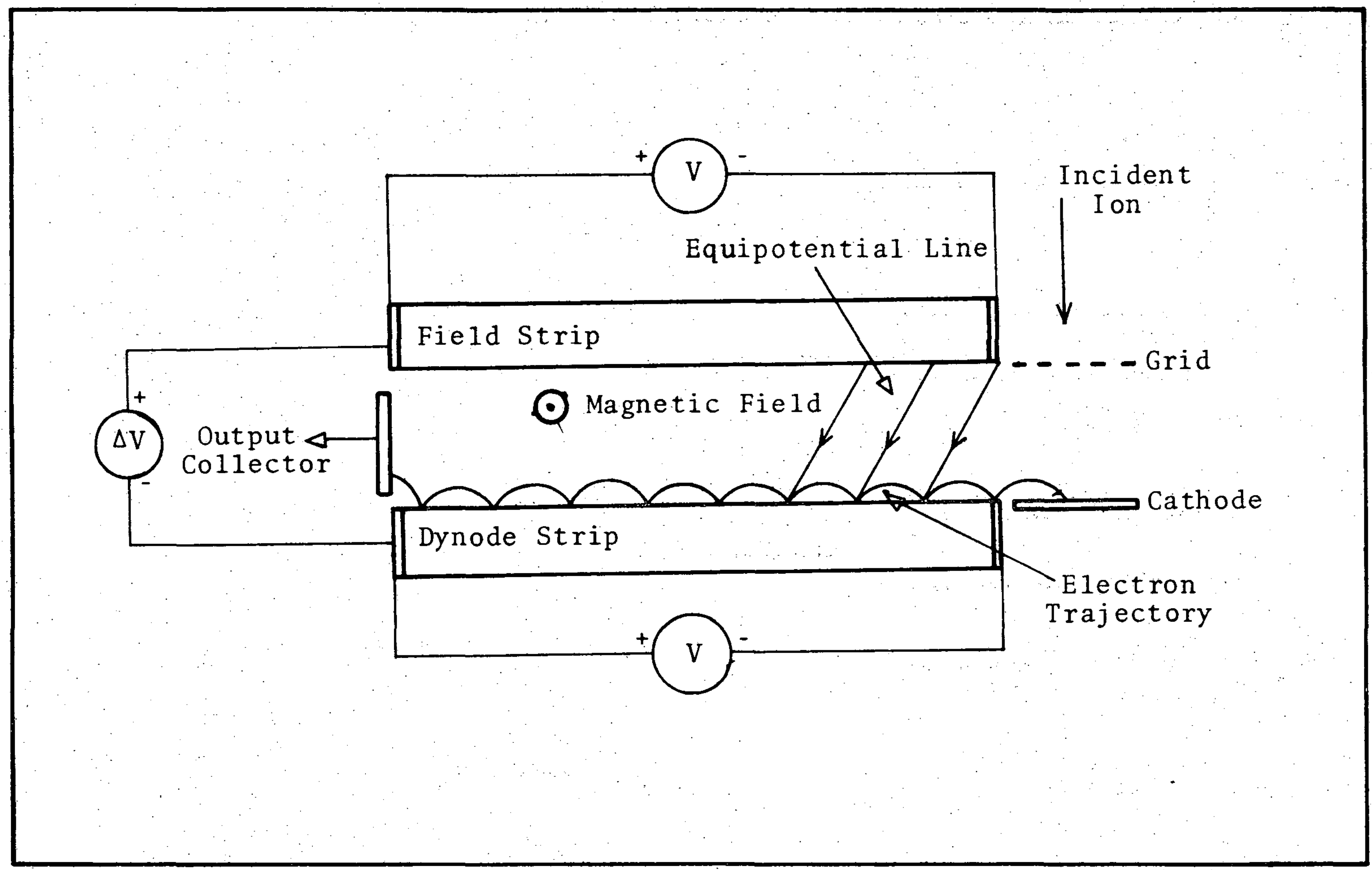

XBL 749-7255

Fig. 11. Magnetic electron multiplier.

strip. The whole process starts when an incident ion passes through the grid and strikes the cathode and emits an electron from the cathode. A gain of $10^6 - 10^7$ is usually obtained with this type of multiplier.

The electron multiplier is fairly indestructible and may be left exposed to the atmosphere for extended periods of time without any noticeable detrimental effects. In practice the output current of the multiplier must be limited to less than 10^{-7} amps because carbonaceous deposits build up and cause sporadic operation.

If the multiplier becomes dirty, it may be restored to its original condition by cleaning. In order to clean the multiplier, it is disassembled and scrubbed with a soft rubber eraser in soap and water. It is then rinsed in distilled water, methyl alcohol, and acetone in that order. The multiplier is then air dried and reassembled.

5. Focusing Elements

After the ions leave the collision cell, they travel approximately 5 cm inside a field free region to a 3 mm defining aperture (see Fig. 2). The detection system thus subtends an angle of ±1.5° at the collision region. The 5 cm path is shielded by an aluminum tube, which is grounded in order to prevent stray electric fields from interfering with the trajectories of the ions.

The 3 mm defining aperture which forms the first lens element, is attached to a Keithley electrometer in order to monitor the ion current. The electrometer biases the defining aperture at approximately ground. The ions are then focused by lens elements C and D into the velocity filter.

Lens element C is a 1/2 in. I.D. stainless steel cylinder that has been cut lengthwise into quarters. The four quarters are biased around the focusing voltage, so that they may be used as horizontal and vertical deflection plates.

After the ions leave the velocity filter, they are focused by three intermediate lens elements into the quadrupole mass filter. When the ions leave the mass filter they are focused and accelerated to about 2000 volts into the cathode of the electron multiplier, I, by another series of lens elements.

When assembling all electrostatic elements, great care must be taken to assure that all of the lens elements are clean and free of grease, dirt, and fingerprints. In order to prevent the buildup of surface charges, all exposed electrostatic surfaces are coated with a solution of colloidal graphite just before assembling.

F. Electronics

A block diagram of the electronics that are associated with the apparatus are shown in Fig. 12. The electronics is essentially divided into two semi-independent sections. One section controls the primary ion source and the other controls data collection and the ion detection system.

1. Primary Ion Source

A diagram of the electronics associated with the primary ion source is shown in Fig. 13. Ions are generated from the collision of electrons that are emitted from a hot Tungsten filament. After the ions are formed, they are focused into the momentum analyzer by several focusing elements. The analyzed ions are then focused into the collision cell by a three ele-

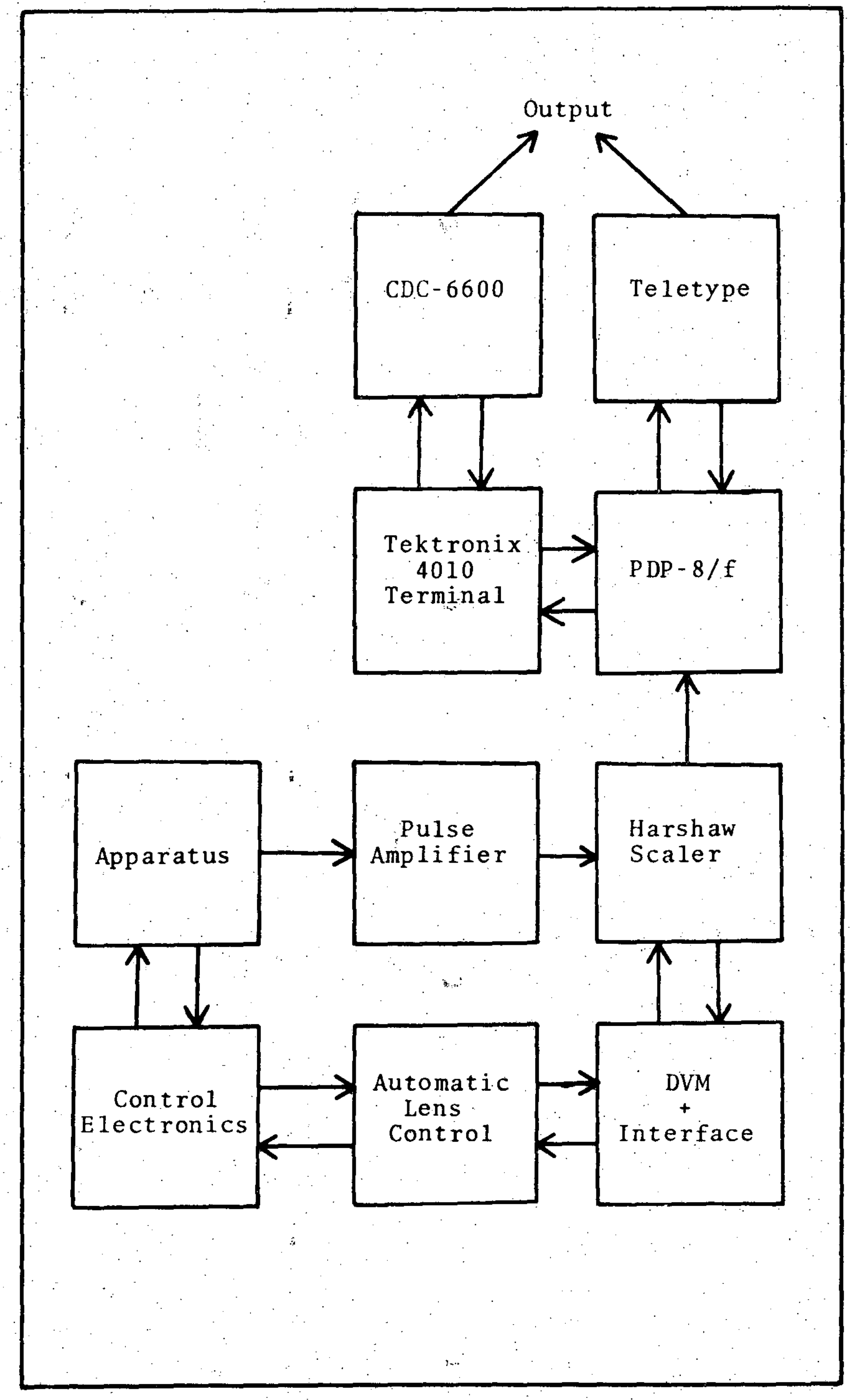

XBL 749-7254

Fig. 12. Block diagram of electronics.

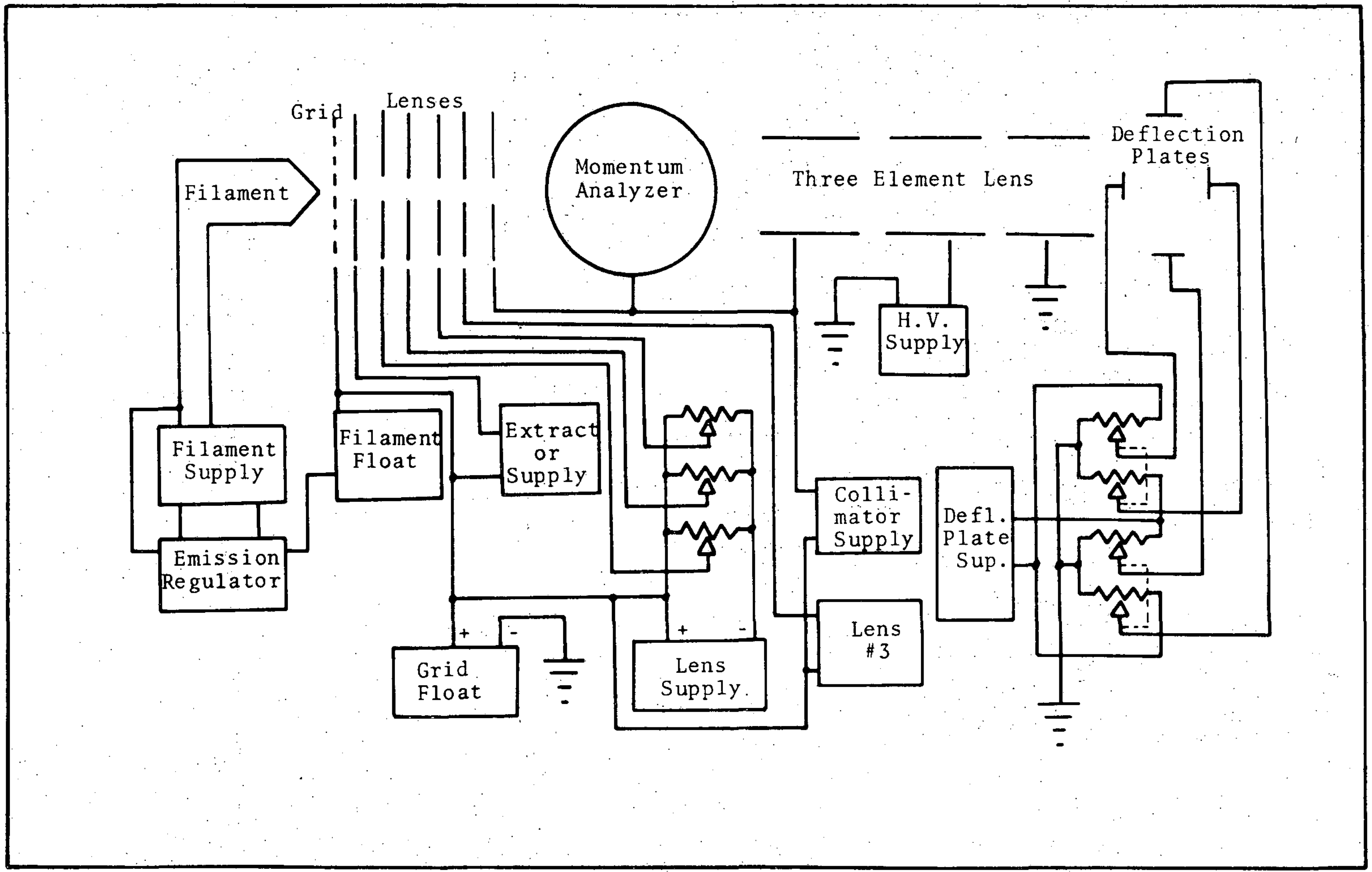

Fig. 13. Primary ion source electronics.

XBL 749-7256

ment cylindrical electrostatic ion lens. Centering of the beam on the collision cell is ensured by a set of horizontal and vertical deflection plates mounted between the final lens element and the collision cell.

Electrons are generated by running 3-5 amps through the filament. The electrons are then accelerated by a potential difference applied between the grid and the filament. The absolute potential of the grid with respect to ground determines the final energy of the ions. In order to maintain a steady beam the emission current between the filament and the grid is regulated by the emission regulator. The emission current is usually set at 50 milliamps and if it starts to drop below this value, the emission regulator increases the current that heats the filament in an effort to offset the drop in emission current.

The potentials applied to the ion lenses come from several different sources. Whenever possible, voltage dividers were used to bias the lenses The use of voltage dividers was only feasible, when the current drawn by the ion lens was very small as compared to the current running through the divider network itself. A separate power supply was used to bias each of the ion lenses that drew more than a few microamperes current.

The electromagnets of the momentum analyzer were powered by a constant current power supply. However, it was found that it still took several hours for the magnetic field to stabilize after initially turning on the magnets.

The deflection plates that are located between the final lens elements and the collision cell are powered by a synchronized voltage divider network. The plates were adjusted so that the central region between the plates was always held at ground potential.

2. Product Ion Detection System

The electronics for the product ion detection system are somewhat more complicated than the electronics for the primary ion source (See Fig. 14). It was determined that the focusing characteristics of the ion lenses depended upon the initial energy of the ions. This problem was not observed in the ion source because there was a fairly small spread in ion energies for any given ion beam. The product ions on the other hand had a fairly large spread of ion energies.

For a given mass the velocity filter passes only ions of one particular energy which has been determined by the operating parameters of the filter (see Section II-E-2). The energy inside the filter of an ion that emanates from the collision cell depends only on the energy of the ion as it leaves the collision cell and the potential of the velocity filter. For example, if the filter is floated at a potential of -10 volts with respect to ground, a singly charged positive ion that leaves the collision cell at an energy of 5 eV will have an energy of 15 eV inside of the filter. If the filter is tuned to pass an energy of 15 eV, only those ions with an energy of 15 eV will pass through the filter without being deflected and ions of all other energies will not make it through the filter without being deflected. Energy analysis is performed by tuning the filter to an optimum energy and then changing only the potential at which the filter is floated.

The only problem with this technique is that the focusing properties of the ion lenses are also velocity dependent. Therefore, the potentials applied to the ion lenses must be changed as well as the potential of the velocity filter. This is accomplished by the automatic lens control, which

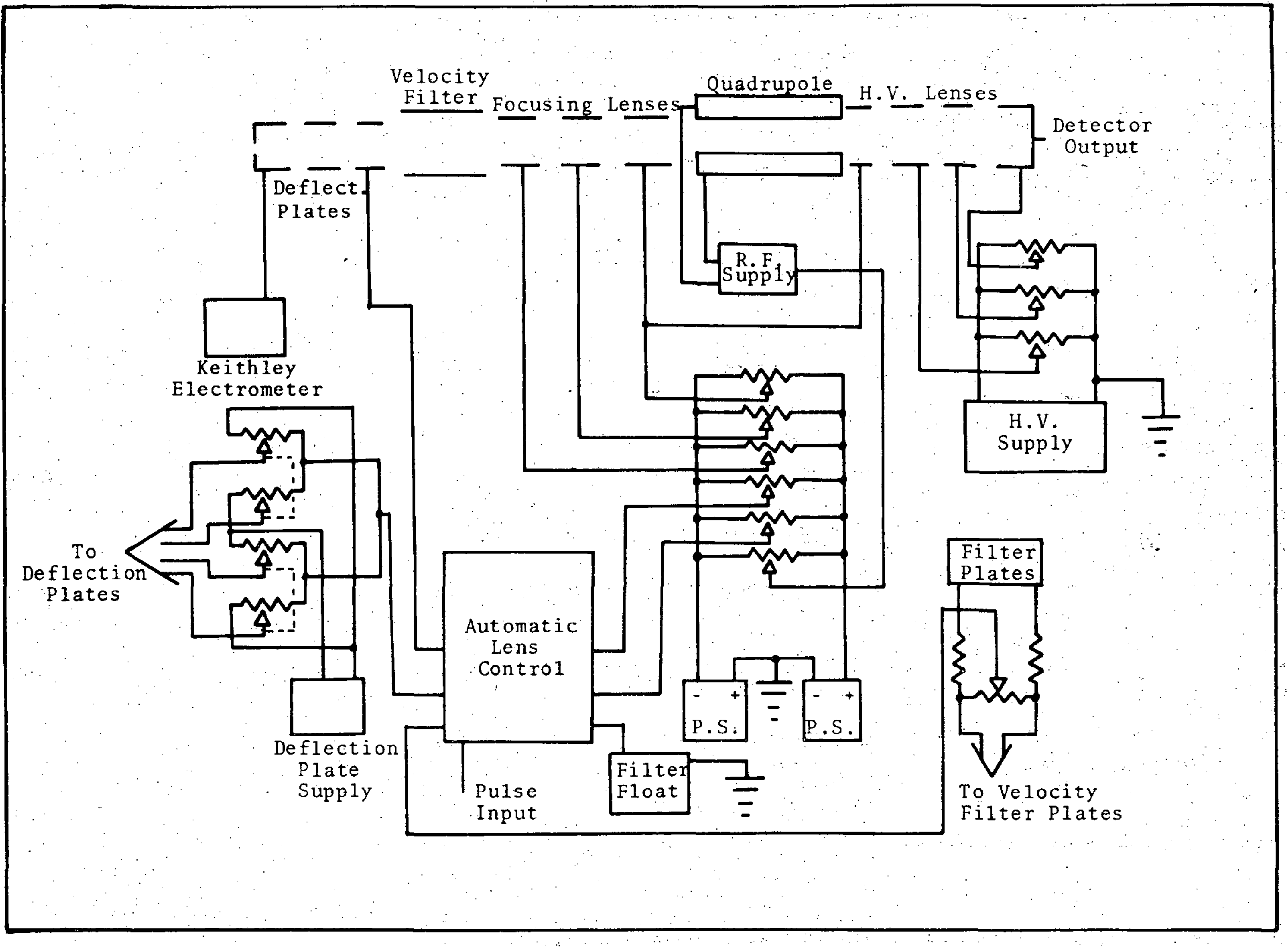

XBL 749-7257

Fig. 14. Product ion detection electronics.

changes the potential of the ion lenses and the velocity filter, so as to maintain optimum focusing for all the ions that pass through the filter.

The potentials that need to be applied to the various lens elements are assumed to vary linearly with the potential of the velocity filter. The approximation appears to hold fairly well as long as the analysis is not performed over a wide energy range.

The schematic for the automatic lens control is shown in Figs. 15 and 16. The linear approximation is set by the float input, which determines the intercept, and the 30K adjustable feedback resistor on the 741 operational amplifier, which determines the slope.

The detection system analyzes at a new energy every time the automatic lens control receives a pulse from the DVM (digital volt meter) interface. Each pulse increments a four bit binary counter (SN74L93) by one. The outputs from the binary counter are routed to a digital to analog converter (DAC-01) which drives the 741 output amplifier. The automatic lens control cycles through 16 different potentials and then it resets back to the beginning automatically on every sixteenth pulse. The lens control may be set or reset manually, if the need arises.

It was determined that after initial tuning only two lenses appreciably affected the focus of the ions as the potential of the velocity filter was changed. All other lenses were biased by voltage divider networks (Fig. 14).

After the ions pass through the velocity filter, they enter the quadrupole mass filter. The power supply for the mass filter has been described in detail by Wilson.[11] After the ions leave the quadrupole, they are accelerated to approximately 2000 volts by the time they reach the

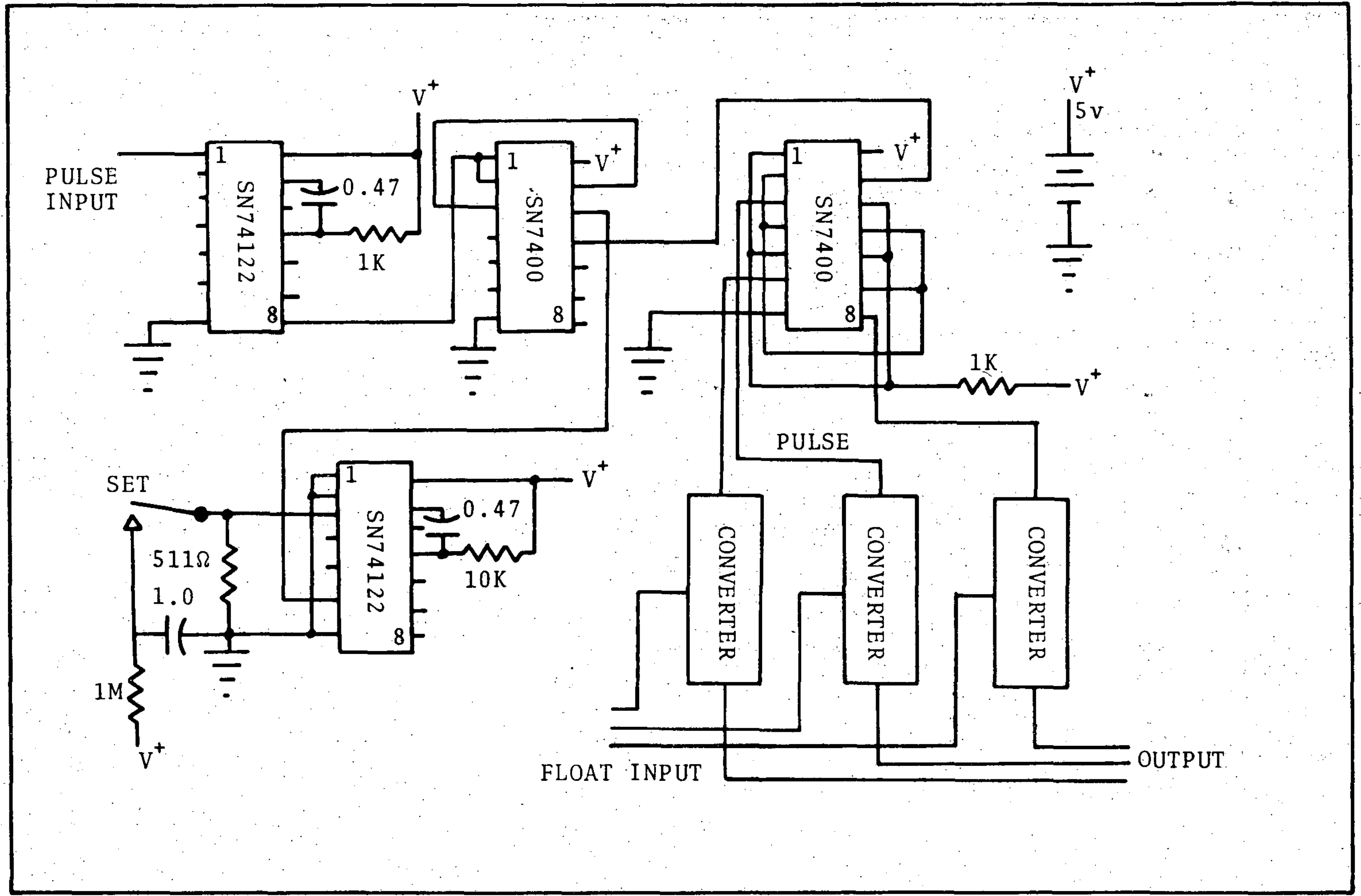

XBL 749-7258

Fig. 15. Automatic lens control.

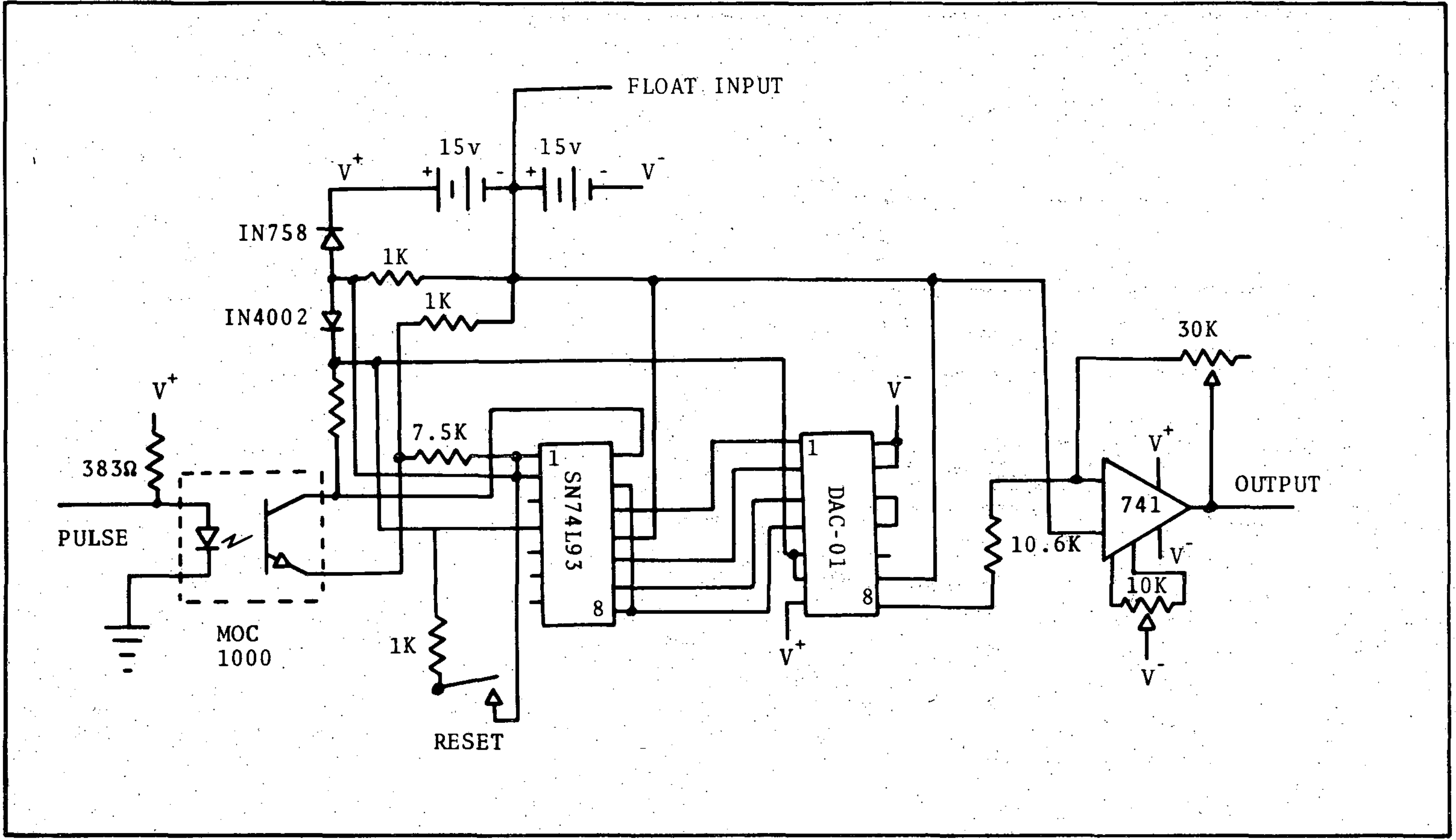

XBL 749-7259

Fig. 16. Converter.

Bendix magnetic electron multiplier.

Each time an ion impinges upon the electron multiplier, an output in the form of a current pulse is obtained. The current pulses are converted into voltage pulses and amplified by two amplifiers in series before being fed into the Harshaw scaler for counting. Each amplifier, whose schematic is shown in Fig. 17, has a gain of approximately 90.

The Harshaw scaler is equipped with a crystal clock time base which enables it to count pulses for a preset period of time. The time period may be varied from 0.1 seconds to 9×10^5 seconds. After the end of each counting period the output is sent to a PDP-8/f computer. The output consists of the number of counts, the time period; and the velocity filter potential. The velocity filter potential is monitored by a digital voltmeter and at the end of each counting period the volt meter interface sends a pulse to the automatic lens control, thereby incrementing all appropriate voltages for the next counting period.

G. Performance

The primary ion source was generally run under the same conditions, as far as possible, for all experiments in order to preserve some degree of uniformity between the individual experiments. The electrons that were used to ionize the neutral gas in the ionizer generally had an energy of approximately 85 eV. The electron emission current was regulated at 50 milliamps. Mass selection was performed in the momentum analyzer at a constant energy of 27 eV and the magnetic field was varied in order to obtain ions of the desired mass. Due to the fact that all of the above conditions were held constant, the width of the energy distribution of the ion beam was independent of the final energy of the ions.

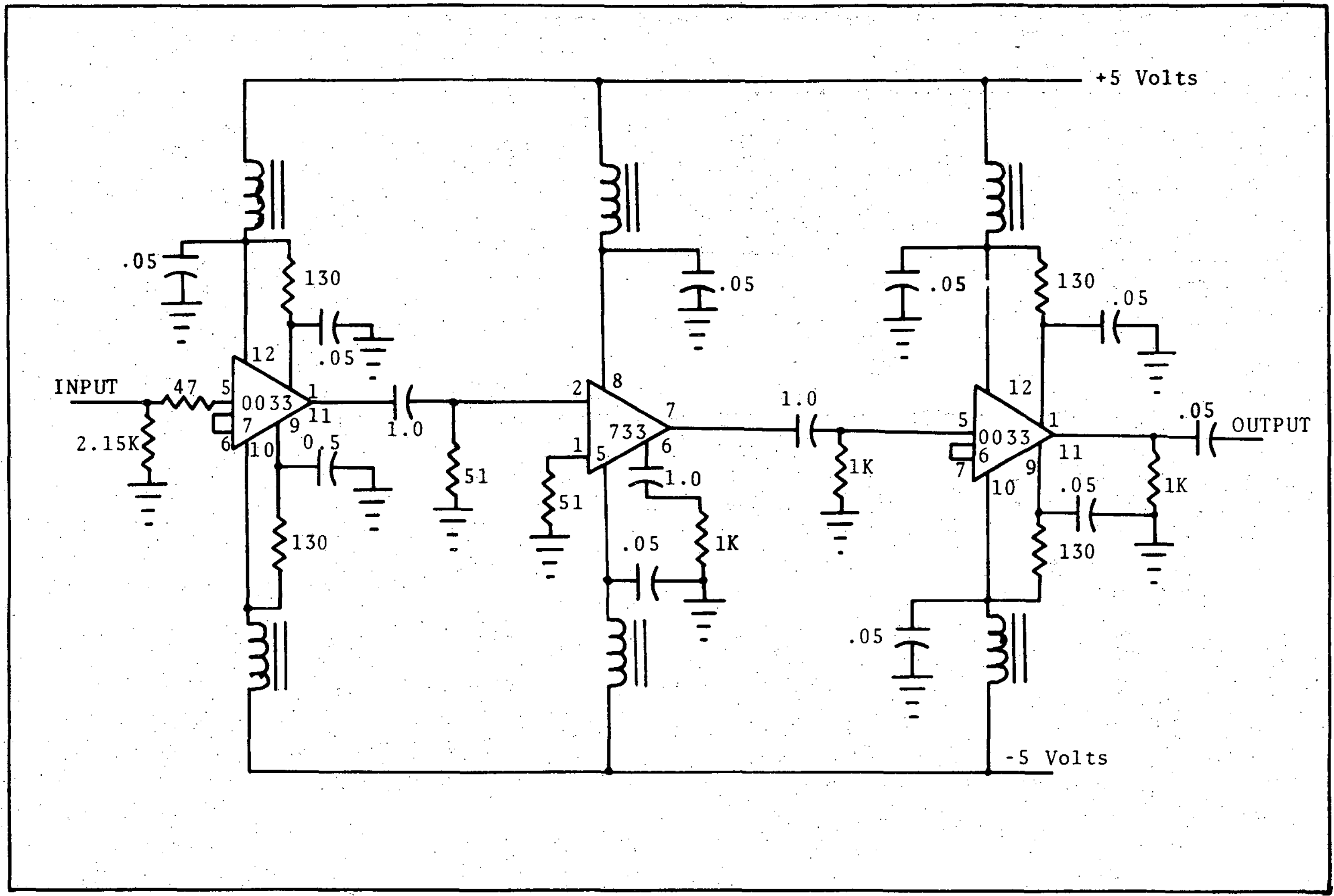

XBL 749-7260

Fig. 17. Pulse amplifier.

In order to determine the energy characteristics of the primary ion source the product ion detection system that was used for all the scattering experiments was replaced with a retarding potential analyzer. While it was not assumed that it is possible to obtain a perfect energy distribution measurement from a retarding potential analyzer, it was assumed that it will be considerably better than the velocity filter and the following results indicate that it is a valid assumption.

Figure 18 shows a typical N^+ energy distribution beam that was derived from the retarding potential analyzer. The peak energy was 9.65 eV with an entensity of 3×10^{-11} amps. The width of the beam (FWHM) was approximately 0.65 eV. A comparison may be made to the energy distribution obtained from the velocity filter with the product ion deflection system in place (Fig. 19). The peak energy is 12.31 eV and the width of the beam is 0.96 eV. Figure 20 shows an angular distribution of an N^+ beam. The width of the angular distribution is 1.8 degrees.

The velocity filter was operated at a magnet current of 4 amps and a potential difference of 1.32 volts between the cylindrical electrodes. The velocity that is passed by the filter is given by Eq. (10) and the energy that is passed is given by

$$E_{filter} = \frac{1}{2} mv^2 = \frac{1}{2} m \left(\frac{E_o}{B}\right)^2 \tag{43}$$

This may be related to the energy E_{ion} of the ion in the collision cell by

$$E_{ion} = E_{filter} + E_{float} \tag{44}$$

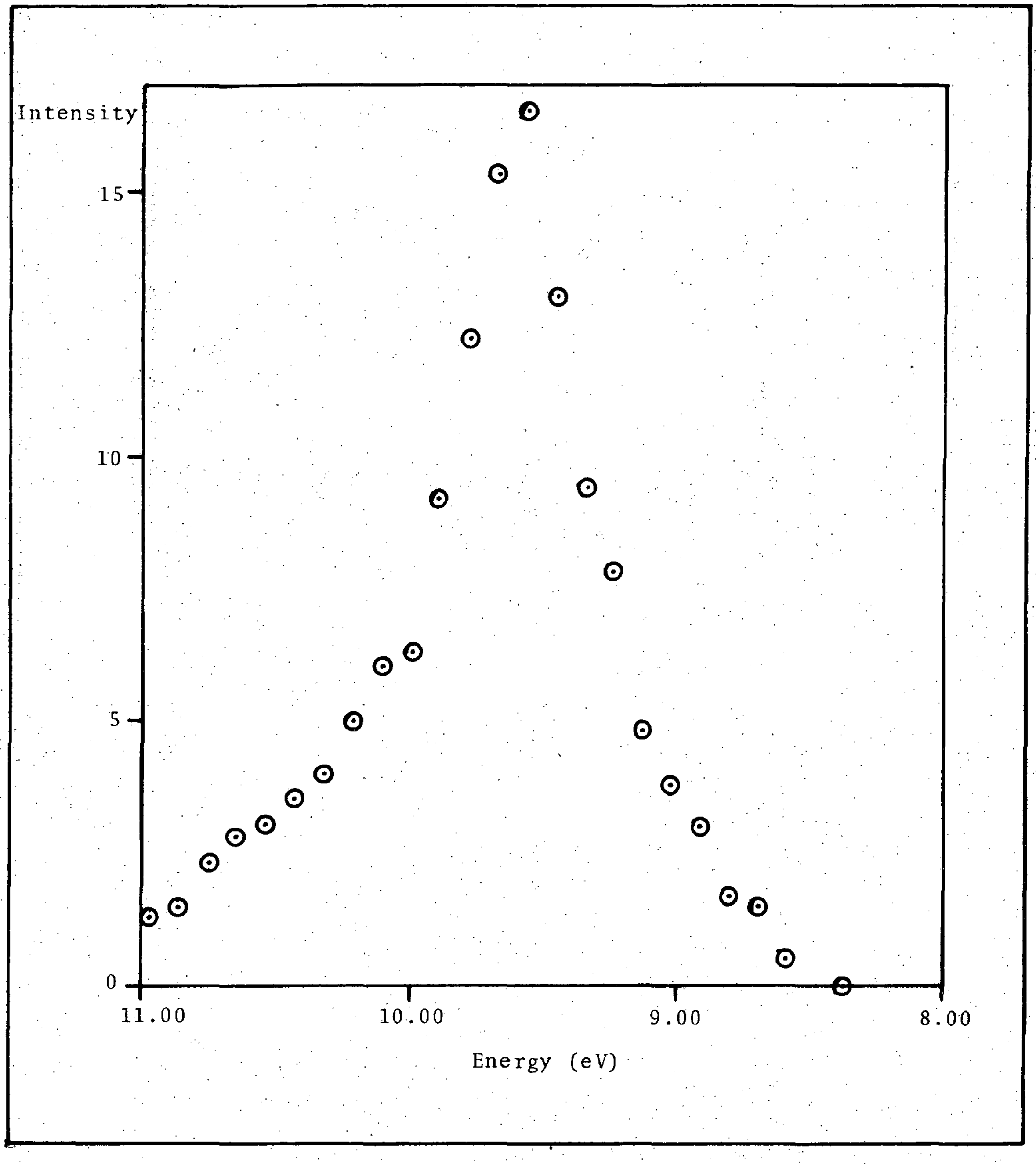

XBL 749-7261

Fig. 18. N^+ energy distribution from retarding potential analyzer.

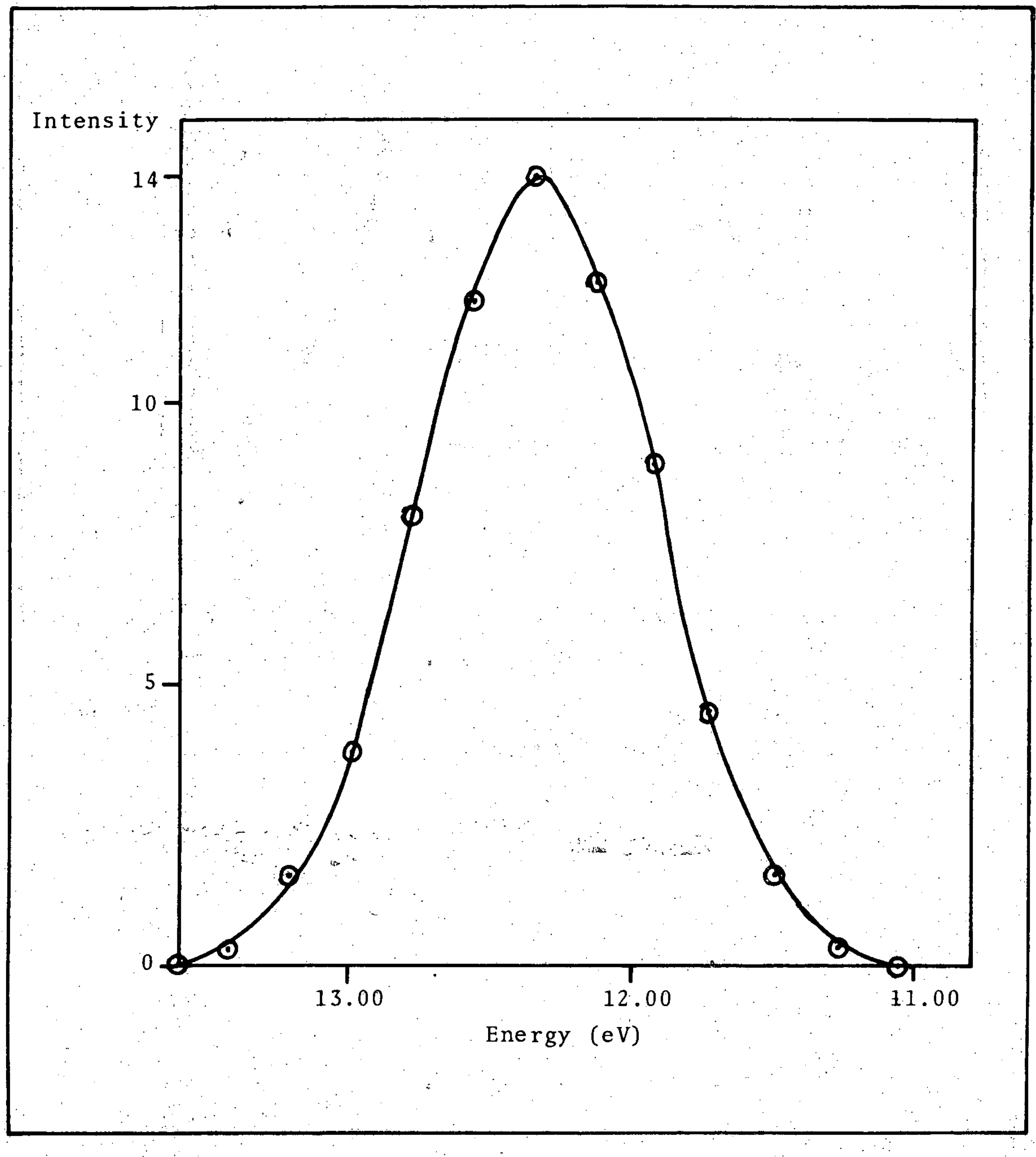

XBL 749-7242

Fig. 19. N^+ energy distribution from velocity filter.

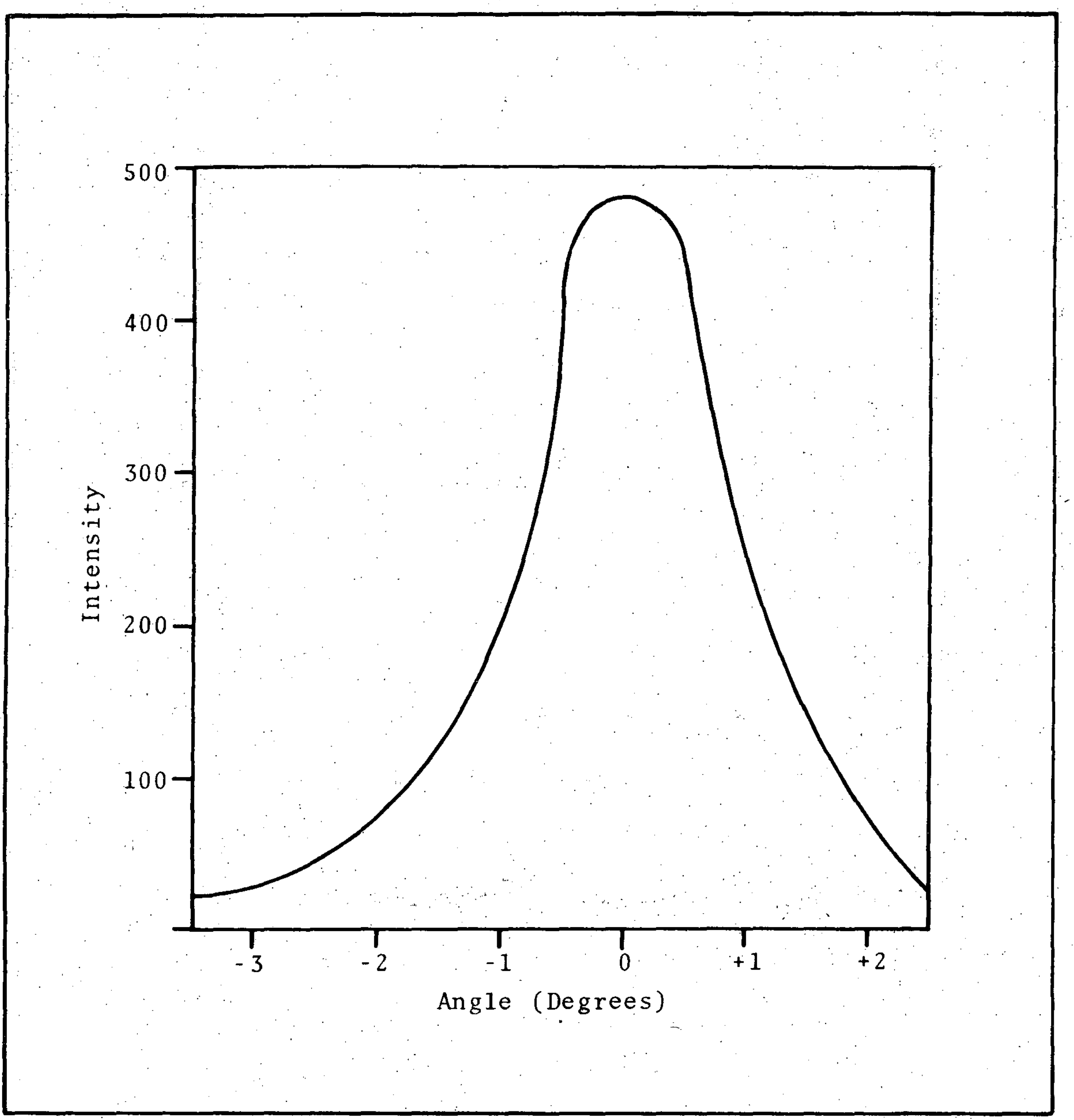

XBL 749-7241

Fig. 20. N^+ angular distribution.

where E_{float} is the potential with respect to ground at which the filter is floated. The electric field E_o may be given by

$$E_o = \frac{\Delta V}{L} \tag{45}$$

where ΔV is the potential difference between the cylindrical electrodes and L is the electrode separation. By substituting Eqs. (43) and (45) into Eq. (44) the following result is obtained

$$E_{float} = E_{ion} - \frac{1}{2} m \left(\frac{\Delta V}{LB}\right)^2$$

$$E_{float} = E_{ion} - k\, \Delta V^2 . \tag{46}$$

If E_{float} versus ΔV^2 is plotted for a stable ion beam, a straight line with slope k and intercept E_{ion} is obtained. For a stable primary beam values of E_{float} vs ΔV^2 may be obtained and the velocity filter thus calibrated. A typical calibration and curve is shown in Fig. 21.

The velocity filter was calibrated in the above manner for every experiment. Values of k ranged between 9.5 and 10.5 eV/volt^2 for a $^{14}N^+$ beam with E_{float}, E_{ion} and ΔV expressed in volts. k would vary slightly from day to day, but the variation was deemed small enough not to interfer with an experiment.

The quadrupole mass filter was very stable and only had to be adjusted once every few years.[11] If the mass filter was tuned to mass 15, the mass 14 signal was attenuated by about a factor of 1000, which was sufficient for this work.

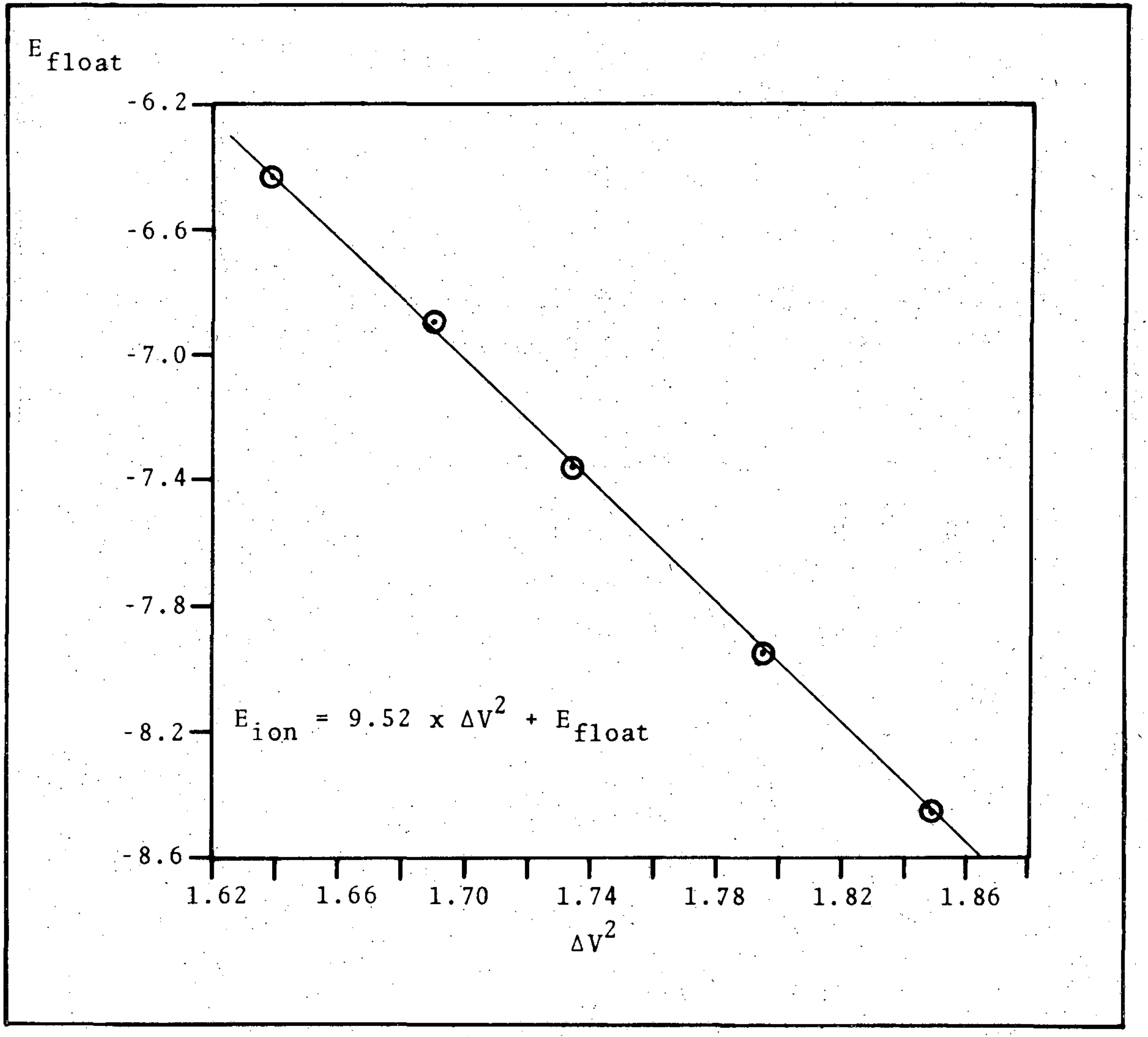

XBL 749-7240

Fig. 21. Velocity filter calibration.

III. DATA COLLECTION AND REDUCTION

A. Collection

In order to run an experiment, a set of focusing conditions for the product ion detection system must first be obtained. A well defined primary ion is generated and focused through the detection system. Focusing is accomplished by adjusting each ion lens until an intensity maximum is reached. This is repeated for each lens again and again until no further increase in intensity is observed. The potential on each lens and the energy of the ion beam is recorded. This process is repeated over again and again for primary beams of different energies, until a complete table of lens potentials vs ion energy is obtained. It was found that only two lens elements had an appreciable effect on the focusing.

For future experiments one need only refer to this table to determine the focusing conditions for each lens as a function of the ions being detected. In order to simplify operation a plot of lens potential vs ion energy was made. A straight line that was the best fit for the points plotted was drawn and the slope determined.

When it came time to actually run an experiment, the primary beam was first turned to maximum intensity. The ALC (automatic lens control) was then programmed for operation. The ALC steps through 16 equally spaced voltages. The step size for the velocity filter floating potential is set on the ALC. The step size for the two critical lenses was then calculated from the slopes derived earlier and set on the ALC. The ALC enables one to obtain an energy distribution of 16 equally spaced points.

A computer program (written by Ralph Terkowitz of this group) that simulates a multichannel analyzer was then initiated in the PDP-8 computer. The computer just accepts data as it is received from the Harshaw scaler and does nothing in the way of actually controlling the progress of the experiment.

Scattering distributions at a given angle are obtained by first setting the angle between the main beam and the detector. The scaler is then started and data collection begins. The scaler counts the number of ions of a given mass and velocity filter potential for the first time period and then stops and transmits the number of counts, the time period, and velocity filter potential to the computer. While the data is being transmitted, the ALC is incremented to the next velocity filter potential. This process is repeated until data is taken at 16 different energies or channels. After the sixteenth time period the ALC is cycled back to the first channel and the process repeats.

After each channel is accessed a second time, the number of accounts are added by the computer to the number of counts already in that channel. This process is repeated until the signal-to-noise ratio attains a satisfactory value. This technique enables one to obtain an intensity distribution at a given angle that is entirely independent of intensity fluctuations in the primary beam.

At the end of each series of scans at a given angle the filter floating potential and the totals for each channel are printed out onto a teletype unit. The data also remains stored in the memory of the computer.

The angle between the detector and the main beam is then changed and an energy distribution obtained for a new angle. This process is repeated for each angle of interest until the entire product scattering distribution is obtained.

The rest of the experiment is controlled manually. The ALC is now locked onto one channel, so that it will not be incremented after each counting period. The same process as before is repeated except that this time the velocity filter potential is held constant and the angle varied manually after each counting period. The angular scanning of only one channel enables all the other energy scans to be normalized so that a final intensity distribution, which is independent of intensity fluctuations, may be obtained.

After the intensity distribution has been obtained, the velocity filter is calibrated in the manner described earlier. At this point the experiment has been completed and all of the data necessary to describe the scattering at a given relative energy is stored in the memory of the PDP-8 computer. The data may then be reduced to a more meaningful form by the PDP-8 or the data may be sent directly over a high speed data communications line to a CDC-6600 computer for reduction and permanent storage.

B. Data Reduction

The most convenient and illustrative way of presenting the data from a beam scattering experiment is in the form of the differential cross section for scattering into an element $d^3\underset{\sim}{v}$ of particle velocity vector space where

$$d^3\underset{\sim}{v} = v^2 \sin\theta \; d\theta \; d\phi \; dv \quad . \tag{47}$$

ϕ is the azimuthal angle and θ is the angle between the incident beam and the scattered product. The number of particles scattered into $d^3\underset{\sim}{v}$ per second is

$$dC = N(\theta,\phi,v) \; d^3\underset{\sim}{v} \tag{48}$$

where $N(\theta,\phi,v)$ is the distribution of particle flux in units of particles per second per unit detection volume.

The differential cross section is

$$I(\theta,\phi,v) \; d^3\underset{\sim}{v} = \frac{N(\theta,\phi,v) \; d^3\underset{\sim}{v}}{N^\circ \rho \ell} = \frac{dC}{N^\circ \rho \ell} \tag{49}$$

where N° is the number of particles per second incident on the target of thickness ℓ and density ρ. The differential cross section is not a readily calculated quantity due to the fact that the detector does not subtend an infinitesimal increment of volume $d^3\underset{\sim}{v}$. In reality the detector has a volume z of finite size, which may be calculated by integrating $d^3\underset{\sim}{v}$ over the detector boundary.

$$z = \int_{\text{det}} d^3\underset{\sim}{v} = \int_{\text{det}} v^2 \sin\theta \; d\theta \; d\phi \; dv \quad . \tag{50}$$

The cross section that is measured is not a true differential cross section, but the cross section for scattering into a detector of finite size. This cross section is

$$I' = \int_{\text{det}} I(\theta,\phi,v) \; d^3\underset{\sim}{v} = \frac{C}{N^\circ \rho \ell} \tag{51}$$

where the number of particles striking the detector is expressed by

$$C = \int_{\text{det}} dC = \int_{\text{det}} N(\theta,\phi,v)\, d^3\underset{\sim}{v} \quad . \tag{52}$$

The value which is calculated from the data obtained in these experiments is $\bar{I}$ which converges to the true differential cross section in the limit of infinitesimal detector size. This is accomplished by normalizing Eq. (51) to the detector volume so that

$$\bar{I}(\theta,\phi,v) = \frac{\int_{\text{det}} I(\theta,\phi,v)\, d^3\underset{\sim}{v}}{\int_{\text{det}} d^3\underset{\sim}{v}} = \frac{C}{N^\circ \rho \ell z} \quad . \tag{53}$$

z may be calculated from Eq. (4) be integrating over the detector volume. Since the aperture of the detector is circular,

$$z = \int_0^{2\pi} d\phi \int_0^{\Theta} \sin\theta\, d\theta \int_{v_1}^{v_2} v^2 dv \quad . \tag{54}$$

If the approximation is made that $\Delta v = v_2 - v_1$ is small and that θ is small and that Θ is the angular width of the detector, one obtains

$$z = \pi\Theta^2 v^2 \Delta v \quad . \tag{55}$$

The detector performs energy analysis by analyzing at a constant energy; therefore, ΔE must be a constant for all ion energies. ΔE may then be expressed as

$$\Delta E = mv\Delta v$$

or

$$\Delta v = \frac{\Delta E}{mv} \quad . \tag{56}$$

Equation (9) may then be written as

$$z = \frac{2^{1/2}\pi\Theta^2 E^{1/2}\Delta E}{m^{3/2}}$$

and $\bar{I}$ as

$$\bar{I}(\theta,\phi,v) = \frac{Cm^{3/2}}{N°\rho\ell 2^{1/2}\pi\Theta E^{1/2}\Delta E} \quad . \tag{57}$$

In order to calculate relative cross sections all the constant factors may be dropped and ℓ expressed as the ratio of the scattering volume subtended by the detector at 0° and the scattering volume subtended by the detector at an angle θ. This gives the final form of $\bar{I}$ which is used in presenting the data obtained in these experiments.

$$\bar{I} = \text{constant} \times \frac{C}{E^{1/2}\ell(\theta)} \quad . \tag{58}$$

A contour map is generated by plotting $\bar{I}$ vs the Cartesian velocity coordinates the connecting points of the same intensity. The reduced data points were plotted by hand or by a Calcomp plotter on the CDC-6600.

IV. REACTION MODELS

Elementary dynamic processes that lead to chemical reactions may be divided into three classifications. These classifications are characterized by the ratio of the time over which the interaction leading to scattering occurs, t_{scat}, to the characteristic rotational period, t_{rot}, of the reaction intermediate. If $t_{scat}/t_{rot} < 1$, the process is said to occur by a direction interaction. If $t_{scat}/t_{rot} > 1$, the process is said to occur via a long-lived intermediate complex. A gray region develops, when $t_{scat}/t_{rot} \simeq 1$ and the reaction has some of the characteristics of both a long-lived intermediate and a direction interaction.

A. $t_{scat}/t_{rot} < 1$

The simplest direction scattering model is known as the spectator stripping model (SS).[14] Most ion-molecule reactions that have been studied display a spectator stripping feature, in addition to less intense large angle scattering associated with rebound processes.

This model is most easily explained by having one of the reactants at rest in a laboratory reference frame, which, for a first approximation, is the situation that occurs in the apparatus that was constructed for this thesis. If an ion A approaches a diatomic BC which is initially at rest, the total momentum that the system has comes from the motion of A. A then strips away B from BC and leaves C unaffected. The atom C is merely a "spectator" and takes no part in the actual dynamics. All of the momentum that the system has leaves on AB. Hence,

$$\underset{\sim}{P}_{\text{initial}} = m_A \underset{\sim}{V}_A \tag{59}$$

and

$$\underset{\sim}{P}_{\text{final}} = (m_A + m_B)\, \underset{\sim}{V}_{AB} \quad , \tag{60}$$

where $\underset{\sim}{P}$ is the momentum and m is the mass and V the velocity. By conservation of momentum

$$\underset{\sim}{P}_{\text{initial}} = \underset{\sim}{P}_{\text{final}} \tag{61}$$

and

$$m_A \underset{\sim}{V}_A = (m_A + m_B)\, \underset{\sim}{V}_{AB} \quad . \tag{62}$$

The ratio of the velocity of the product AB to the initial velocity of A can then simply be expressed as

$$\frac{\underset{\sim}{V}_{AB}}{\underset{\sim}{V}_A} = \frac{m_A}{m_A + m_B} \tag{63}$$

and the ratio of the laboratory energies is given by

$$\frac{E_{AB}}{E_A} = \frac{m_A}{m_A + m_B} \quad . \tag{64}$$

Thus, the product is forward scattered at an angle of zero degrees and at a velocity greater than that of the center-of-mass.

An energy that does not appear as translational energy of the products appears as internal energy of AB. By conservation of energy

$$\begin{aligned} E_{\text{initial}} &= E_{\text{final}} \\ E_{\text{initial}} &= E_A + U_{BC} \\ E_{\text{final}} &= U_{AB} + E_{AB} + E_o \\ E_A + U_{AB} &= U_{AB} + E_{AB} + E_o \quad . \end{aligned} \tag{65}$$

U_{AB} and U_{BC} are the internal energies of the diatomic AB and BC, respectively. In the case where the internal energy of BC is zero, then

$$U_{AB} = -E_o + \frac{m_B}{m_A + m_B} E_A \tag{67}$$

The spectator stripping model predicts increasing internal excitation with increasing relative energy of the reactants. Whenever the internal energy becomes greater than the dissociation energy of the product, the product can no longer be formed. An example of this behavior is discussed later (see Section V-A) for the system $N^+(H_2,H)\ NH^+$ as it relates to work done by Gislason et al.[3]

Several other simple direct mechanisms have been proposed for other systems[15] and they are generally some type of variation on the spectator stripping model. One of the most prominent variations was proposed by Wolfgang[16] and is called the "polarization stripping model". It is basically a stripping model with the inclusion of ion-induced dipole forces for the reactants as they approach and then again as they recede. This model has been applied to the system $N_2^+(D_2,D)\ N_2D^+$ and was found to agree quite well. The polarization stripping model leaves the product N_2D^+ less internally excited than the spectator stripping model by about 0.15 eV.

B. $t_{scat}/t_{rot} > 1$

The characteristic feature of this process is that the intermediate exists longer than several rotational periods of the complex. When the lifetime of the intermediate is long compared to the rotational period, the products, which flyoff as the intermediate decompose, will have a direction that is totally unrelated to the initial center-of-mass velocity vectors of the reactants. This leads to a symmetry around ±90° for the reactive scattering distributions in the center-of-mass reference frame.

In order for a complex to be held together for several rotational periods, a deep potential well in the potential energy hypersurface must be present. An estimate of the lifetime of the complex may be made from the following equation[17]

$$\tau = \nu^{-1}\left(\frac{E}{E - D}\right)^{s+\frac{1}{2}-1} \qquad (68)$$

where τ is the lifetime, ν the characteristic vibrational frequency, E, the total energy, D, the well depth, s, the number of "active" vibrations, and r, the number of rotations. Equation (68) was derived from a classical degenerate oscillator and rotator model and has very limited validity when E is approximately equal to D. The characteristic period of rotation may be calculated from[18]

$$\tau_{rot} = 2\pi(I/L) \quad . \qquad (69)$$

where I is the moment of inertia and L the angular momentum.

If a long lived complex exists, the velocity and angular distributions may be calculated by statistical or phase space theories.[19-21] This calculation assumes a statistical partitioning of energy among the various active modes of the intermediate.

C. $t_{scat}/t_{rot} \simeq 1$

Whenever the lifetime of the intermediate is approximately the same magnitude as the rotational lifetime, a nebulous situation arises. A direct impulsive reaction occurs in a much shorter period of time and a long lived complex exists for a much longer period of time. When the lifetime is shorter than several rotational periods, there is no longer time for the internal energy to be partitioned completely randomly throughout the various internal modes of the intermediate. The intermediate will then decay, yielding products that depend markedly on the original orientation of the collision partners in momentum and position space.

One of the criteria for having an intermediate that exists longer than several vibrational periods is the existence of a well in the potential energy hypersurface, so that there is some attractive force that holds all of the atoms together. If the intermediate exists long enough for the energy to mix in a pseudorandom fashion throughout the internal modes, but shorter than several rotational periods, a situation arises which has been described as an "osculating complex".[22] The complex will then decay in a fashion that may or may not be completely statistical in nature. An extremely rough approximation to the angular distribution may be calculated by multiplying the results for a statistical decay by a fall-off function (Fig. 22) that depends on the ratio of the lifetime of the intermediate to the minimum rotational period. Use of the fall-off function assumes that during rotation about its total angular momentum vector the complex is subject to decomposition with a random lifetime distribution, exp(-t/τ).

In the case where the ratio of the lifetimes is larger a long lived complex results and the angular distribution will be symmetric around ±90°, but as the ratio of the lifetimes decreases, the angular distribution will become more and more asymmetric around ±90°.

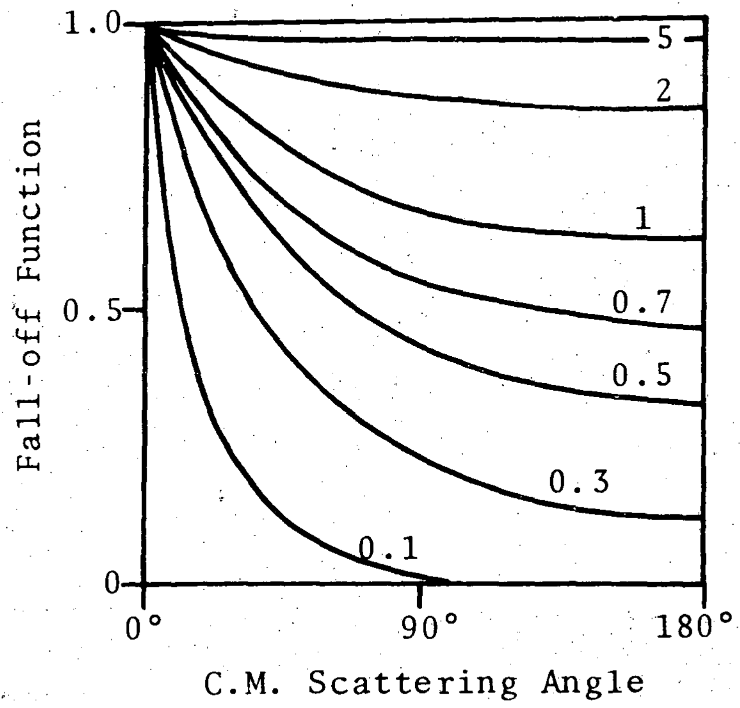

XBL 749-7262

Fig. 22. Fall-off function.

V. REACTIVE SCATTERING OF N^+ BY H_2

A. Background

At the present time no work on the system $N^+(H_2,H)\ NH^+$ has been done in the energy range covered in this experiment. However, Fehsenfeld, Schmeltekopf and Ferguson[2] have studied this system at lower energies and Gislason, Mahan, Tsao and Werner[3] have studied this system at higher energies.

Fehsenfeld et al. have measured the rate constant for this reaction in a pulsed-discharge, flowing-afterglow reaction tube. In the flowing-afterglow tube the reaction occurred in a 300°K thermalized plasma. A rate constant of 0.56×10^{-9} cm^3/sec was determined at 300°K. As a comparison a rate constant was calculated for collisions that yielded orbiting. The collision rate is given by[23]

$$k = 2\pi e(\alpha/\mu)^{1/2} \quad , \tag{70}$$

where α is the polarizability of H_2 and μ is the reduced mass. The collisions arise from the long range charge-induced-dipole interaction to cause orbiting or collisions which spiral inward. A rate constant of 1.57×10^{-9} cm^3/sec was calculated by this method.

Gislason et al. studied this reaction in a beam apparatus similar to the one employed in this work. The reaction was studied in a region of relative energy ranging from 2.50 eV to 8 eV. The work that was done below 3.7 eV has questionable validity.

In all the experiments performed by Gislason et al. the velocity spectra showed an intense NH^+ peak with a velocity greater than that of the center-of-mass velocity, and a second less intense peak at a velocity less than that of the center-of-mass. The reaction is accredited to occur by a direct interaction, where the forward scattered NH^+ is slightly more excited internally than would be expected from the spectator stripping model. There is evidence that at initial relative energies below 4 eV, the principal product is NH^+ in the $^4\Sigma^-$ ground state, while at initial relative energies above 6.5 eV the $^2\pi$ state is formed predominantly. Their results are tabulated in Fig. 23.

B. Experimental Results

The reactive scattering of N^+ by H_2 was examined at relative energies ranging from 0.78 eV to 4.02 eV, while concentrating mainly on the scattering below 2.78 eV. The velocity spectra are given in the form of contour maps, whose derivation has been given earlier (see Section III-B). The contour maps are shown in Figs. 24 through 35.

All of the contour maps show only one peak and with one exception the intensity maximum occurs at a velocity greater than the velocity of the center-of-mass. In general, as the relative energy decreases, the NH^+ intensity maximum gradually moves towards a lower and lower center-of-mass velocity, until it actually coincides with the center-of-mass velocity. For the most part the energy of the NH^+ product is more highly excited than that expected from a spectator mechanism (Eq. (67)).

The absence of any significantly intense backward scattered peak and a high degree of assymmetry around ±90° in the center-of-mass reference frame indicates that no intermediate complex exists with a lifetime greater than several rotational periods. The symmetry around ±90° gradually increases as the relative energy decreases until it becomes highly symmetric at the lowest energy investigated.

E_o(eV)	E_{rel}(eV)	V/V_o[*]	Q
20.14	2.52	(0.923)	(-1.7)[**]
30.09	3.76	9.23	-2.59
31.84	3.98	0.927	-2.50
35.36	4.42	0.926	-2.83
40.09	5.01	0.923	-3.43
45.05	5.63	0.924	-3.70
49.80	6.22	0.929	-3.70
50.09	6.26	0.932	-3.50
53.39	6.67	0.931	-3.76
56.61	7.08	0.932	-4.04
60.16	7.52	0.931	-4.31
65.41	8.18	0.934	-4.27

[*] Ratio of NH^+ product velocity to initial projectile velocity. For the spectator stripping model, V_{ss}/V_o = 0.933.

[**] Location of the peak quite uncertain.

Fig. 23. NH^+ energy from Gislason et al.[3]

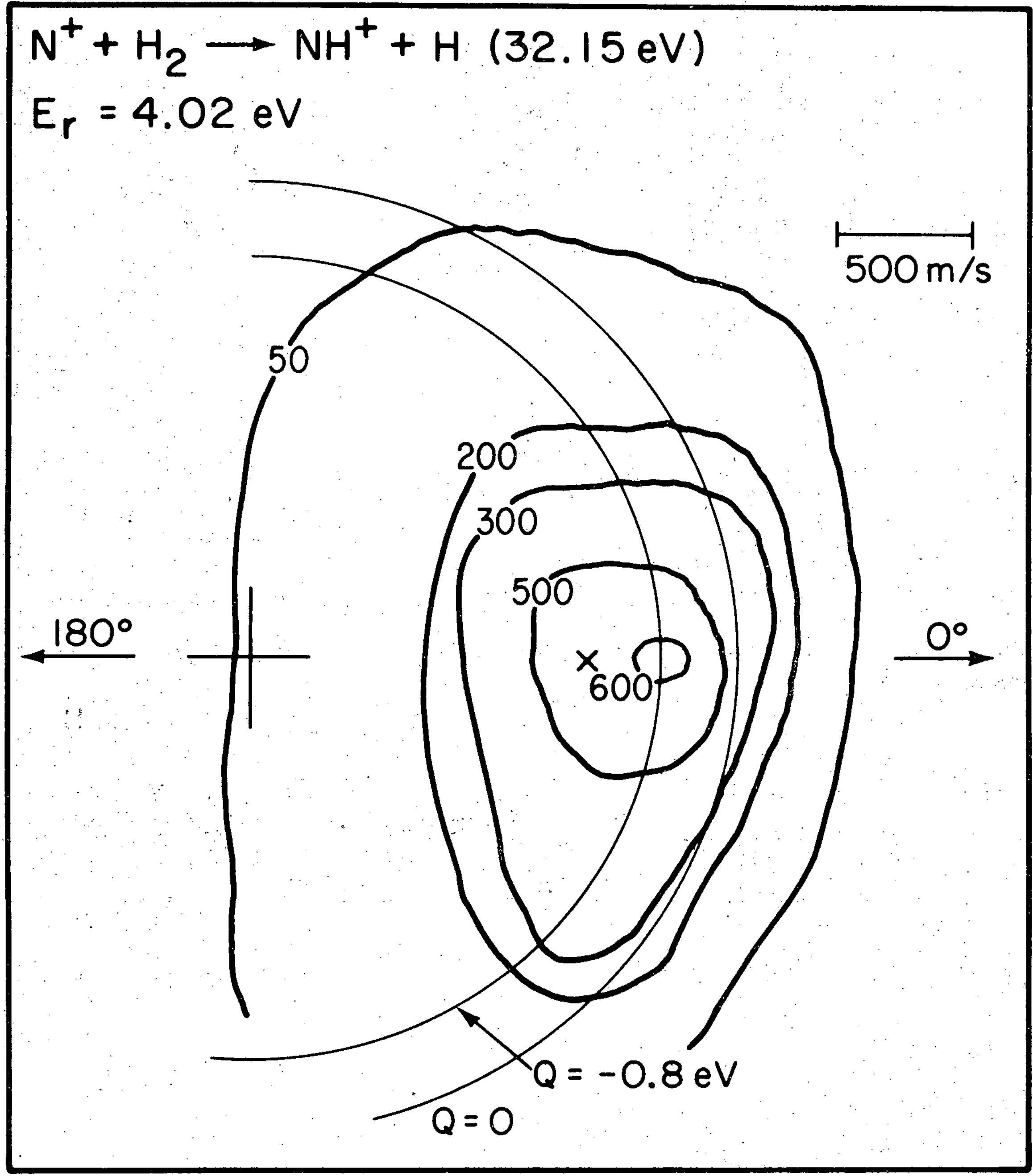

XBL 749-7355

Fig. 24. These figures show the relative intensity of the NH^+ formed by the reactive scattering of N^+ from H_2. The large cross indicates the location of the center of mass and the X indicates the location of product predicted by the spectator stripping model. Circles indicating various values of the translational exoergicity (Q in eV) are also shown. The lowest energy contour map is accurate to within 50 meters/sec and the highest energy map is accurate to within 100 meters/sec.

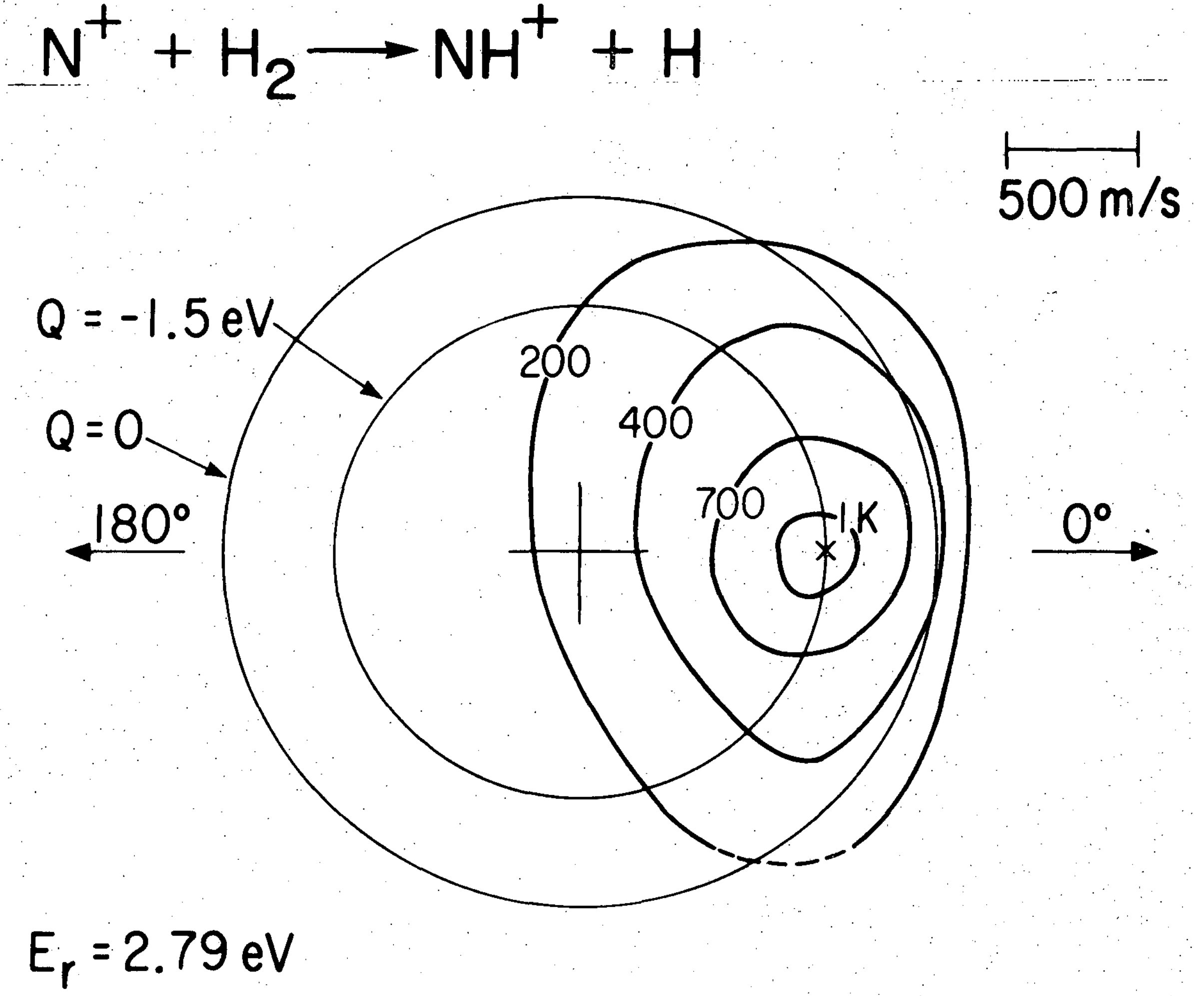

XBL 749-7347

Fig. 25. See Fig. 24.

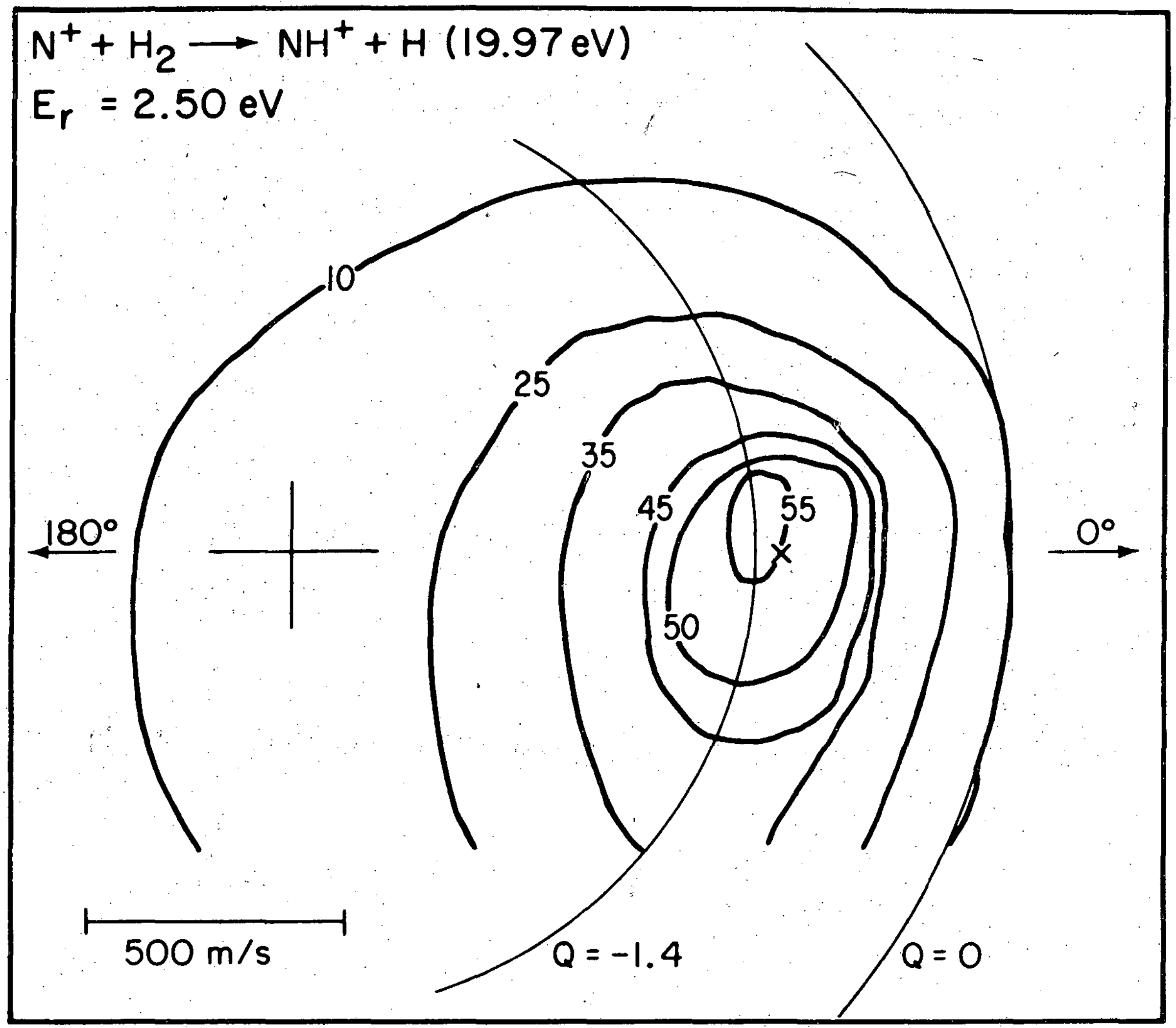

XBL 749-7356

Fig. 26. See Fig. 24.

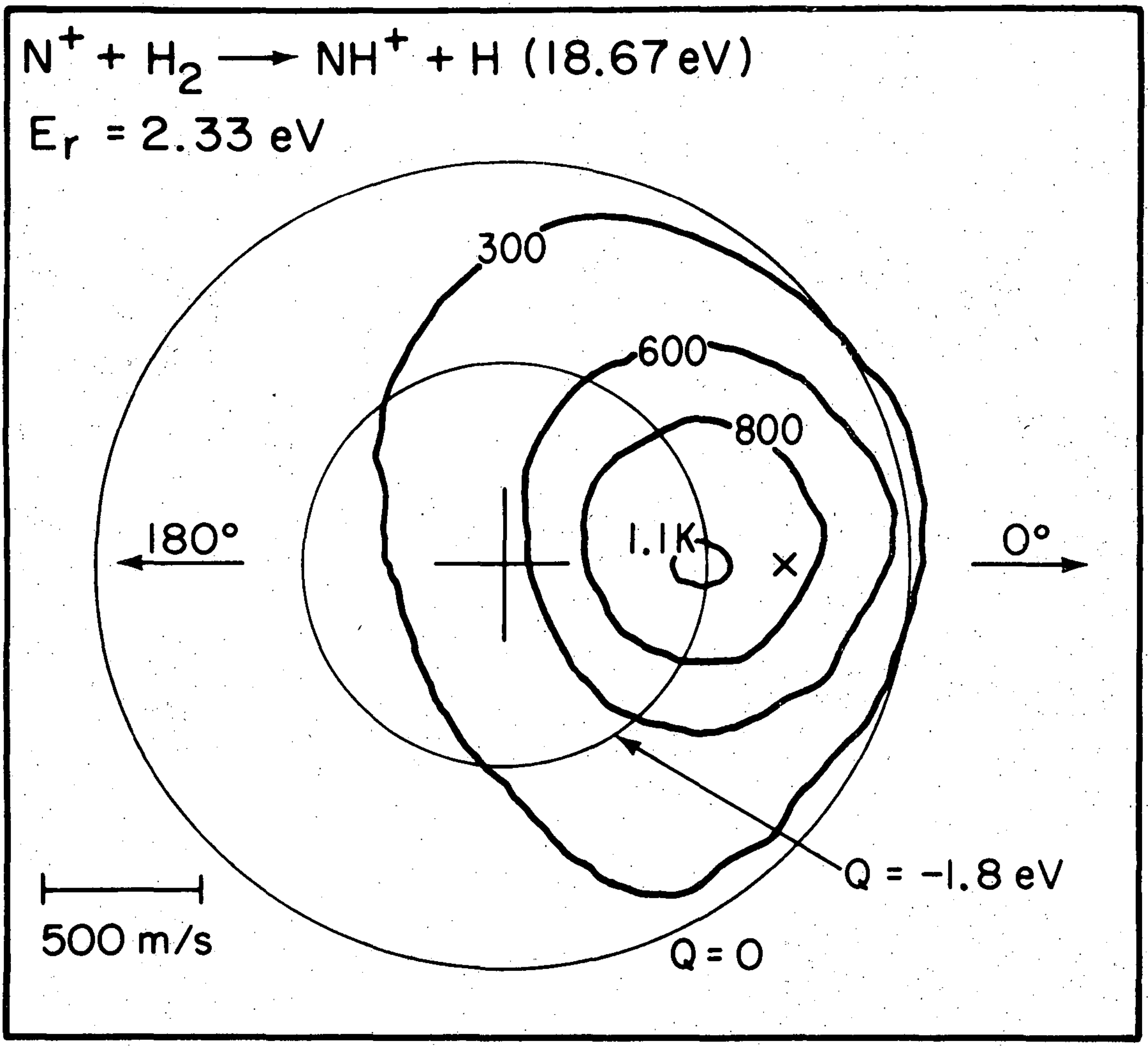

XBL 749-7357

Fig. 27. See Fig. 24.

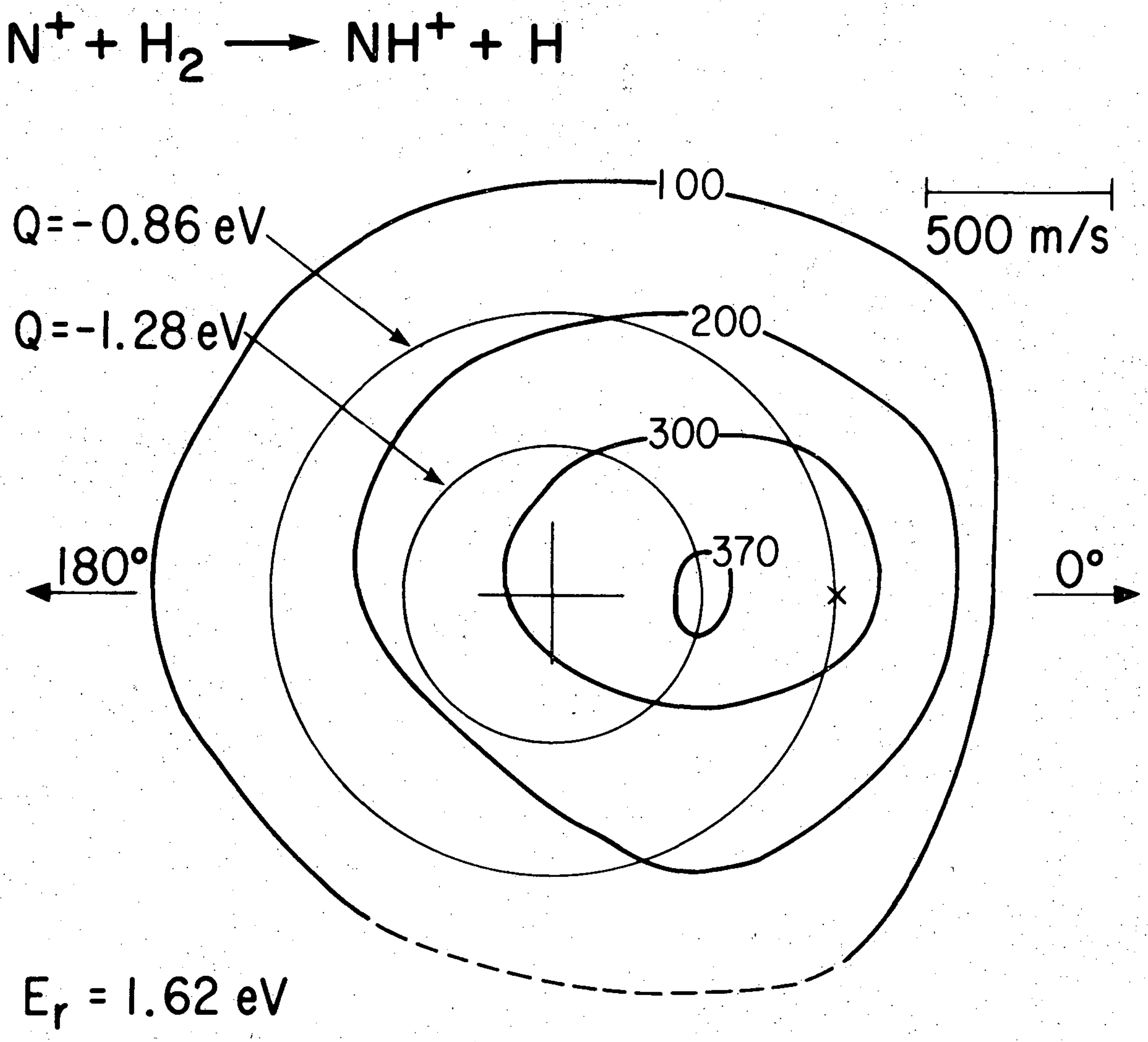

XBL 749-7350

Fig. 28. See Fig. 24.

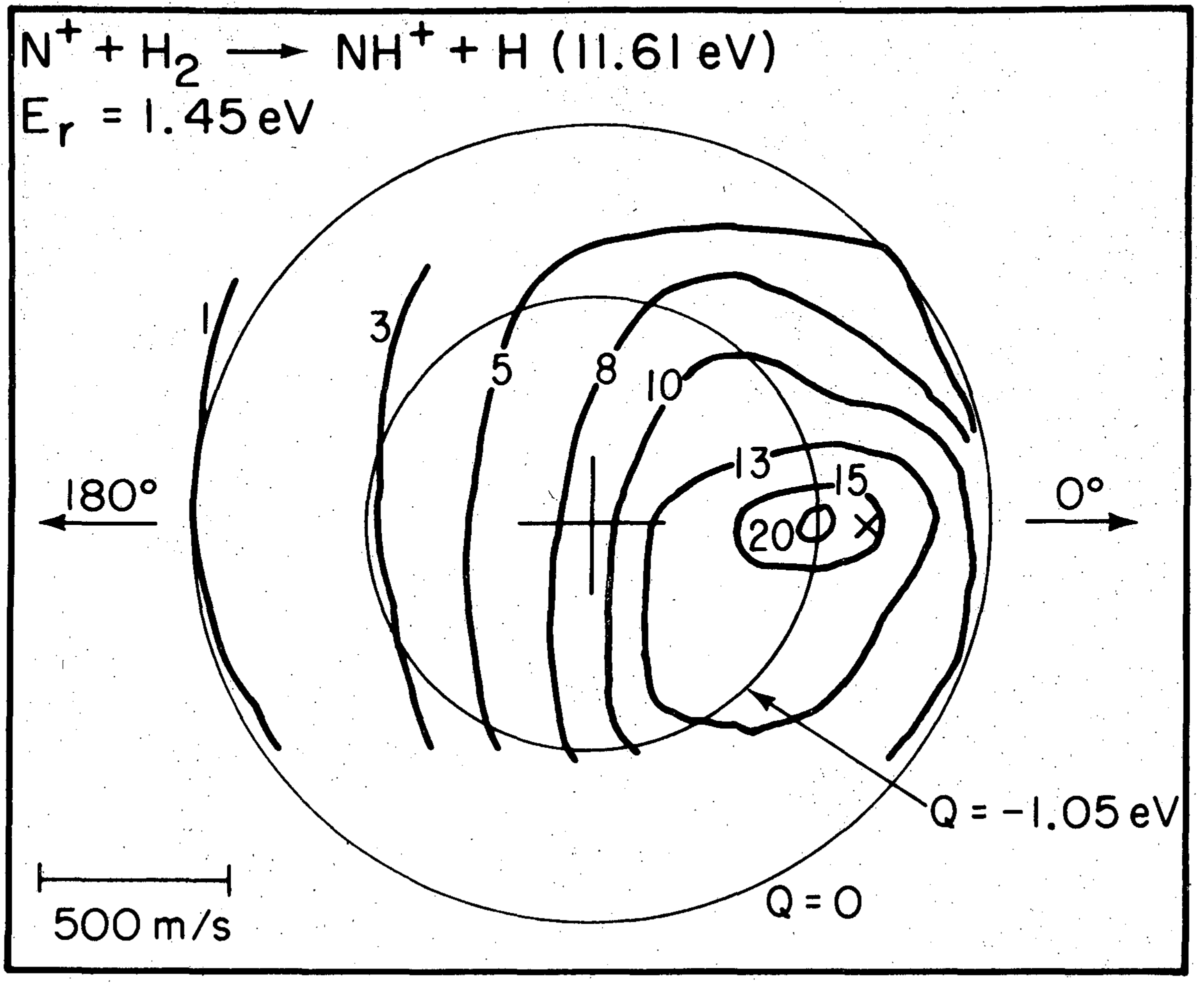

XBL 749-7358

Fig. 29. See Fig. 24.

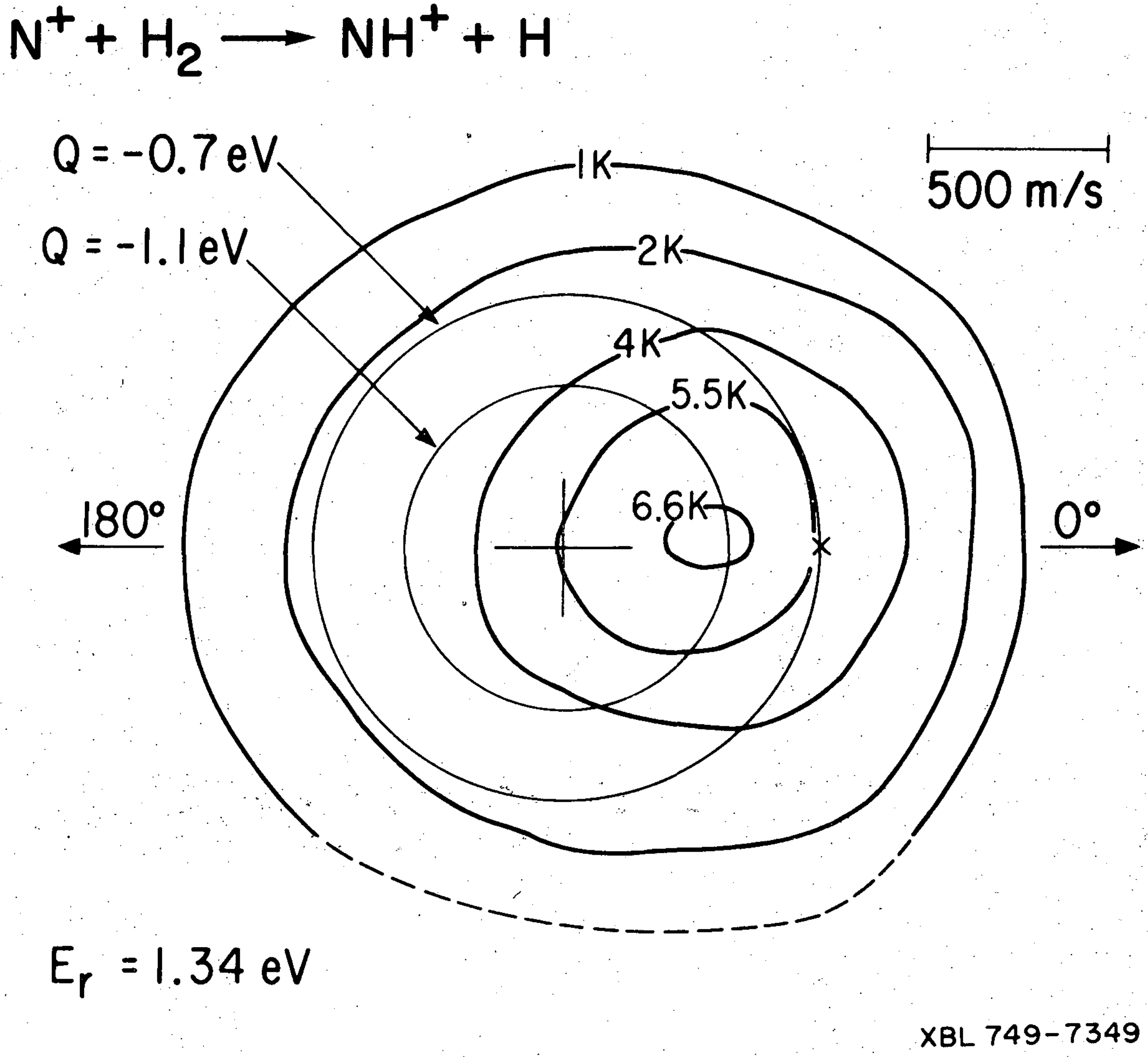

Fig. 30. See Fig. 24.

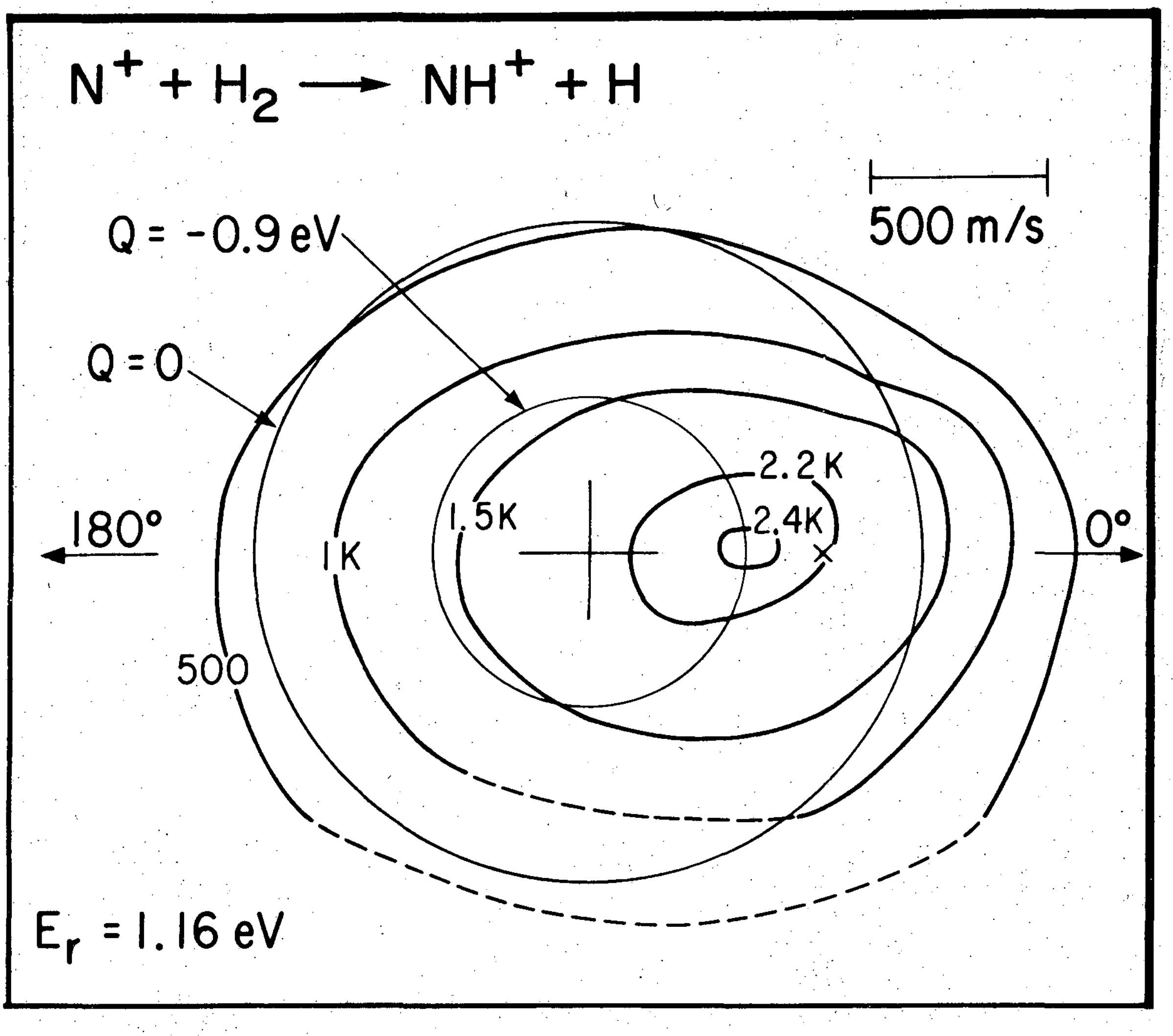

XBL 749-7348

Fig. 31. See Fig. 24.

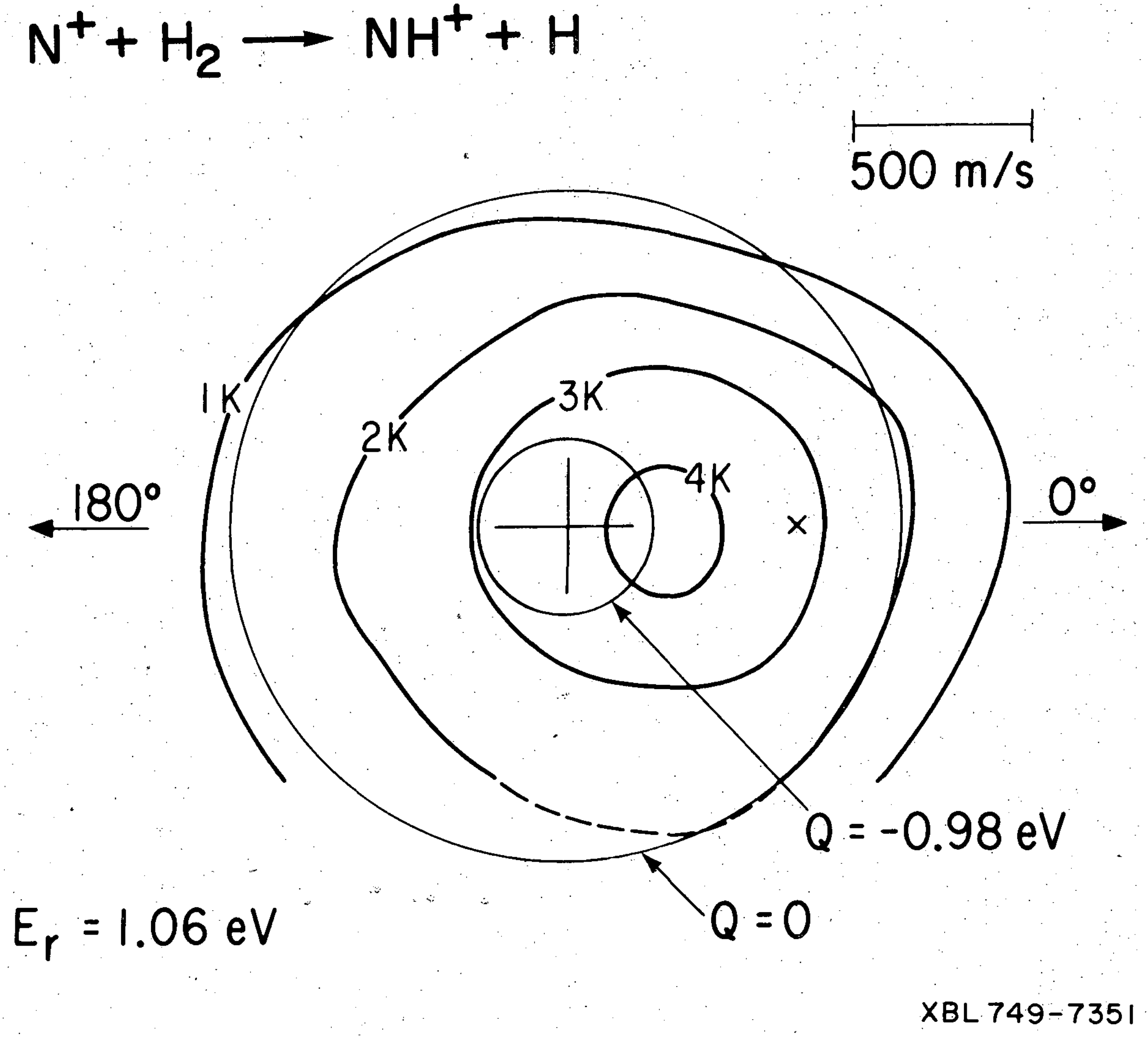

Fig. 32. See Fig. 24.

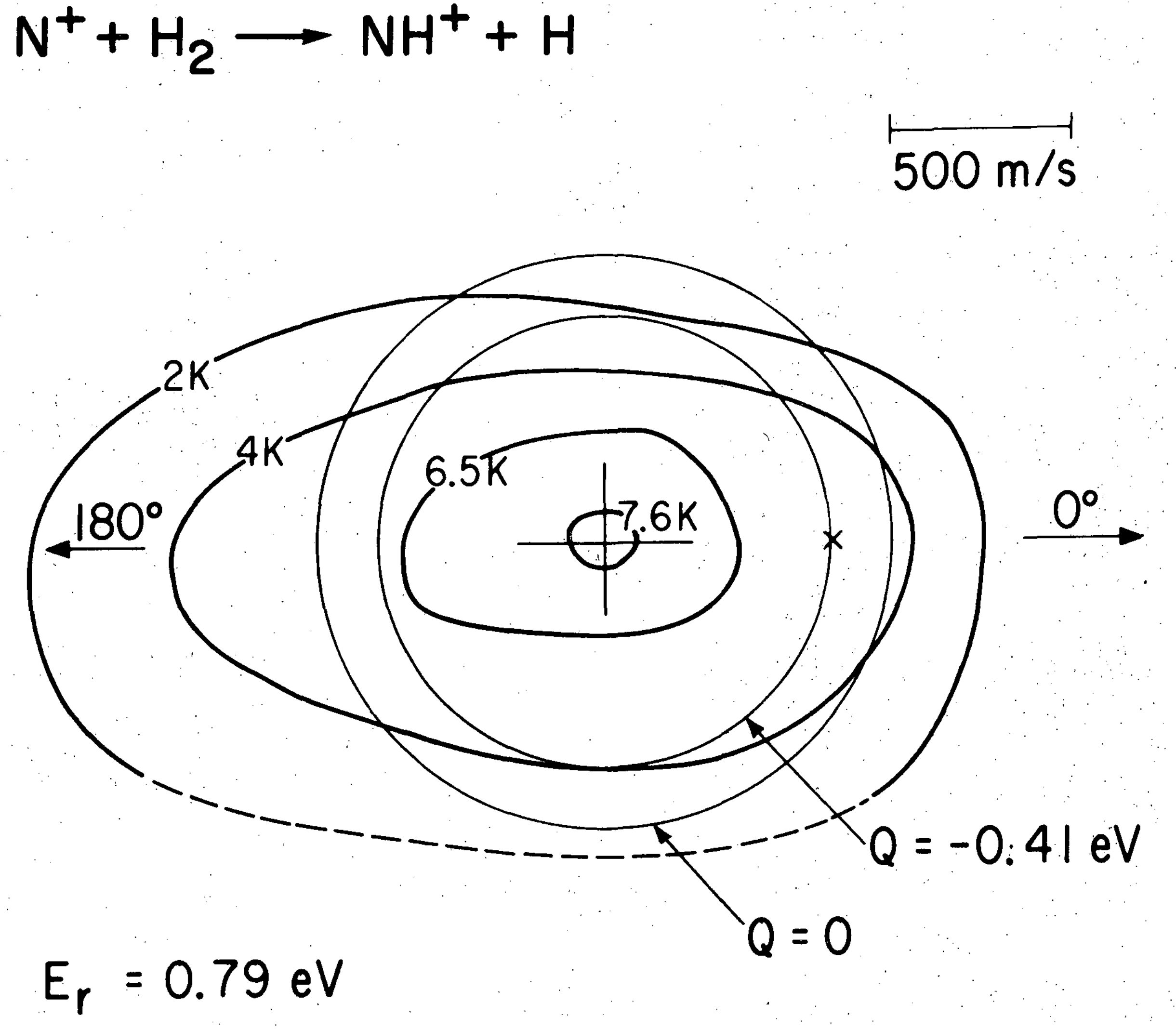

XBL 749-7352

Fig. 33. See Fig. 24.

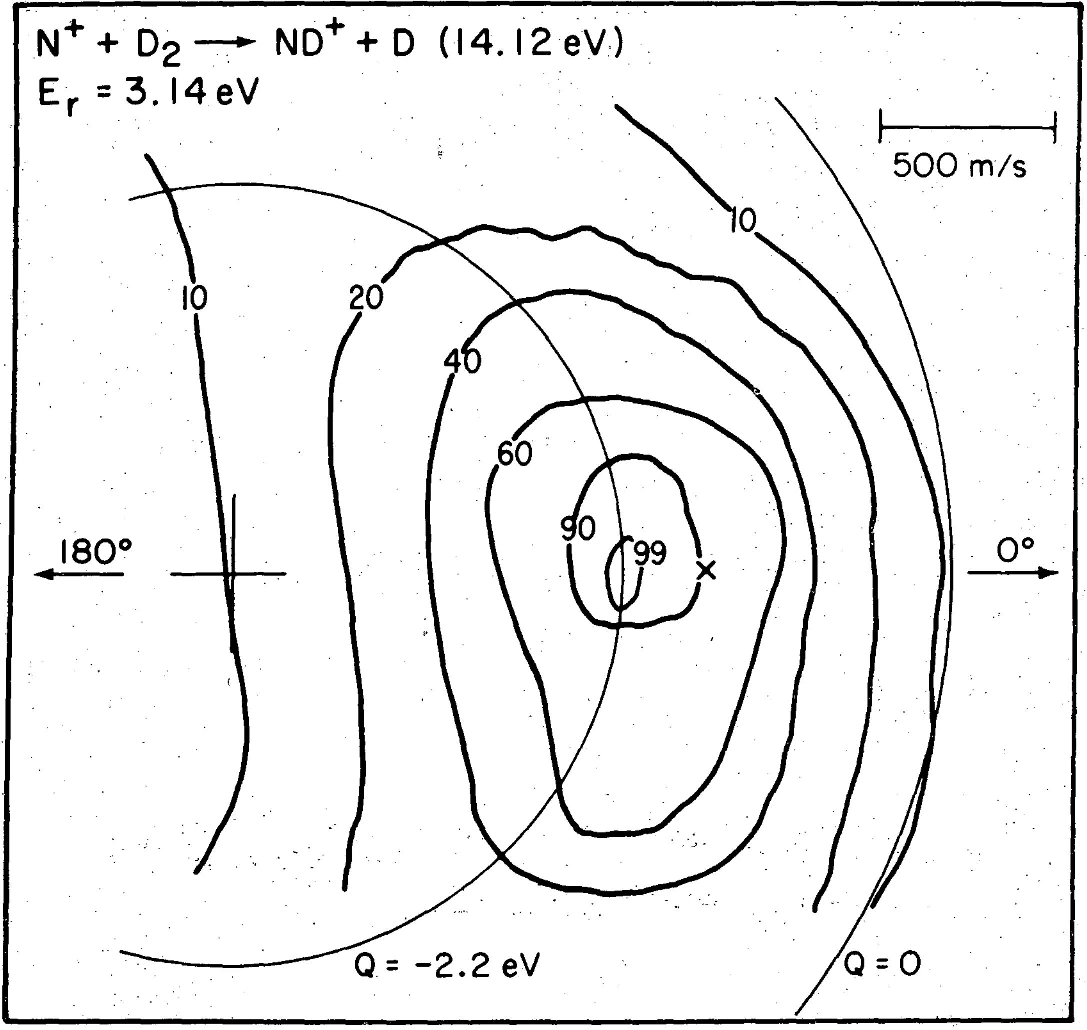

XBL 749-7354

Fig. 34. Reactive scattering from D_2.

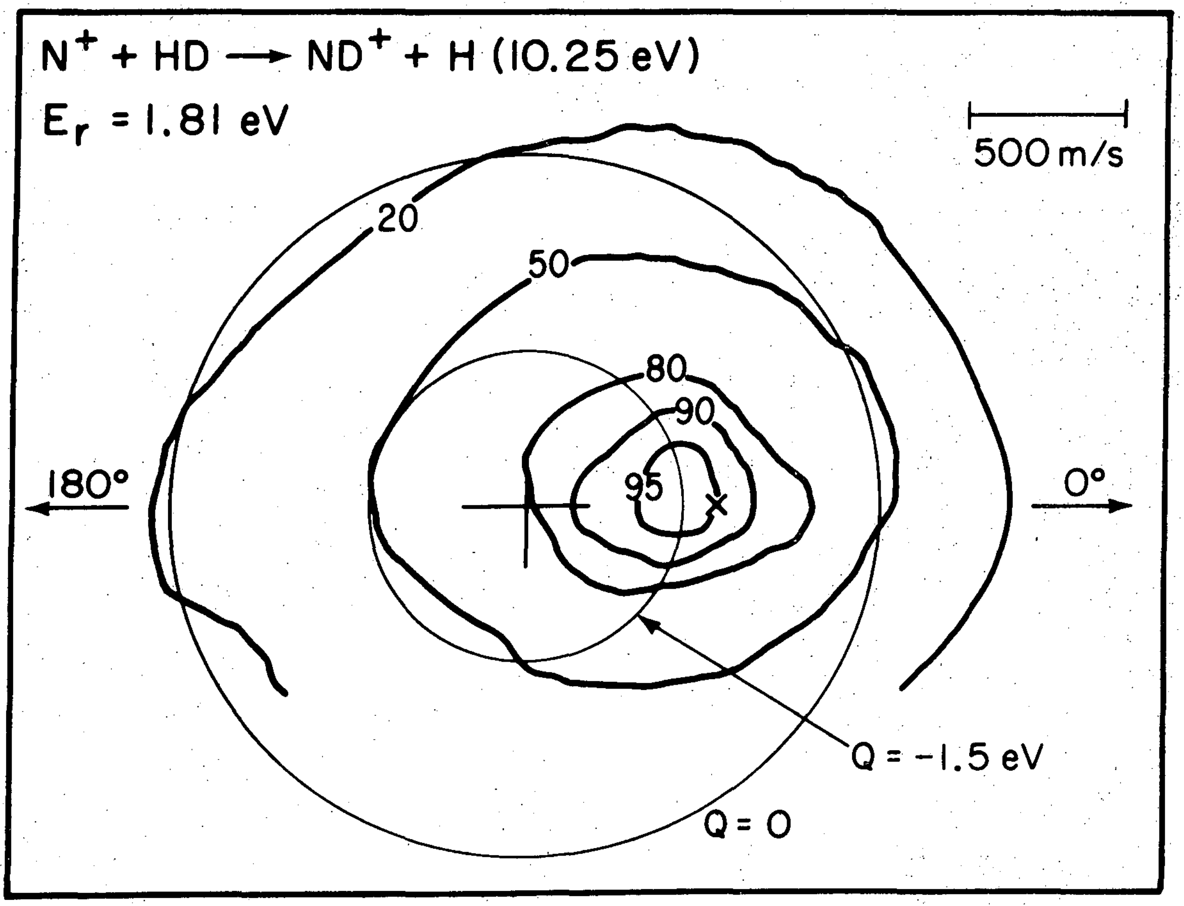

XBL 749-7353

Fig. 35. Reactive scattering from HD.

The data obtained in this work may be compared with low energy work done by other experimenters. Wolfgang and co-workers[16] studied the systems $Ar^+(D_2,D)\ ArD^+$ and $N_2^+(D_2,D)\ N_2D^+$ at relative energies down to 0.1 eV. Both of these systems were very strongly forward peaked with little or no large angle scattering and the dynamics agree with those predicted by the polarization stripping model (see Section IV-A).

Mahan and Sloane[24] studied the system $C^+(H_2,H)\ CH^+$ at relative energies ranging from 2.8 eV to 7.1 eV. Their work shows results which are very similar to the results obtained in this work. At the higher energies the CH^+ product distribution is very asymmetric around ±90° with an intense forward peak accompanied by a significant amount of large angle scattering. As the energy is decreased the forward peak gradually moves toward the center-of-mass and the product distribution becomes less asymmetric around ±90°. Mahan et al. attribute this phenomenom to the exsistence of a strongly interacting complex where there is an attractive force between all three atoms.

It can be seen that the dynamics of the system $N^+(H_2,H)\ NH^+$ do not proceed by way of a long lived complex that exists for several rotational periods. The ion NH_2^+ has been observed quite extensively in mass spectrometric studies, so there has to be a deep potential well somewhere in the NH_2^+ potential energy hypersurface. It is then evident that criteria, other than a deep potential well, must be satisfied in order for products to be formed by a long lived complex, such as that observed in the reaction[25]

$$C_2H_4^+ + C_2H_4 \rightarrow C_4H_8^+ \rightarrow CH_3 + C_3H_5^+ \rightarrow C_3H_3^+ + H_2 \quad .$$

C. Discussion

As any bimolecular reaction occurs, the molecular orbitals of the reactants gradually interact and evolve into the orbitals of the collision complex. The orbitals then evolved into those of the products. One may construct a correlation diagram which shows the connection between the reactants and products. The technique involved in constructing a correlation diagram has been recently discussed in an article by Mahan.[26]

The procedure involved in constructing a correlation diagram is fairly simple and to the point. An appropriate collision geometry with some reasonable symmetry is chosen and the molecular orbitals of the reactants, intermediate complex, and the products are resolved into the symmetry species of the appropriate point group. The states are ordered according to their energy. States or orbitals of the same symmetry species are then connected.

For the purposes of this discussion, two collision geometries were chosen: one being the approach of N^+ along the perpendicular bisector of H_2 to form a bent or linear $(H - N - H)^+$ intermediate complex and the other being a linear head-on approach to form a linear or near linear $(N - H - H)^+$ intermediate complex. Both intermediate complexes are then followed as they dissociate into the products for the reaction.

1. Perpendicular Bisector Approach

The first step in obtaining an actual correlation diagram is to determine the relative energies of the various states and orbitals that participate in bonding. The relative energy of various electronic states of H^+, N^+ and H_2^+ were obtained from tables given by C. E. Moore.[27] The energy of the $^2\pi$ ground state of NH^+ was also obtained from Moore. Information on the excited states of NH^+ came from Liu and Verhaegen,[28] who did an ab initio calculation on NH^+.

The energy of $^3B_1$ ground state of NH_2^+ was also obtained from tables given in Moore. Chu, Sui and Hayes[29] performed some theoretical studies of the low-lying electronic states of NH_2^+. Chu et al. also studied the effect of the change of angle of the H - N - H bond on the energy of the low lying electronic states of NH_2^+. Potential energy curves for the change of bond angle from 90 to 180° are shown in Fig. 36.

A. D. Walsh[30] has described the shapes and energies of AH_2 molecules. The electronic orbitals possible for an AH_2 molecule, when linear, can be correlated with those possible for the molecule when in a bent configuration. Gimarc[31] has performed extended-Hückel molecular orbital calculations on the various orbitals in AH_2 molecules. His results on the relative energies of the orbitals were used in establishing the molecular correlation diagram that was used in this thesis. Figure 37a shows drawings of molecular orbitals and a qualitative orbital correlation diagram for bent and linear AH_2 molecules. Figure 37b shows a more quantitative correlation diagram that was derived from extended-Hückel calculations.

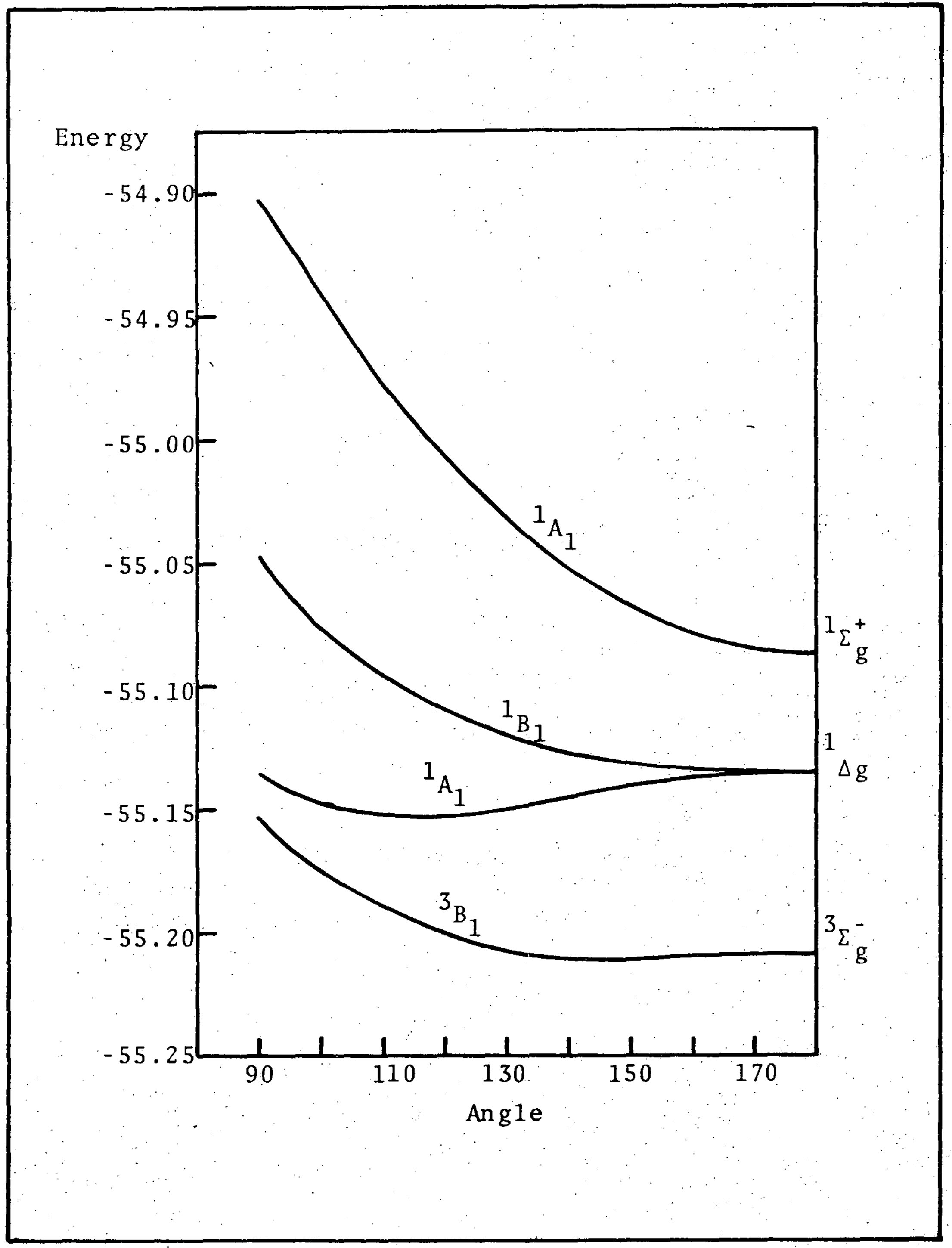

XBL 749-7263

Fig. 36. Potential energy vs angle for NH_2^+.

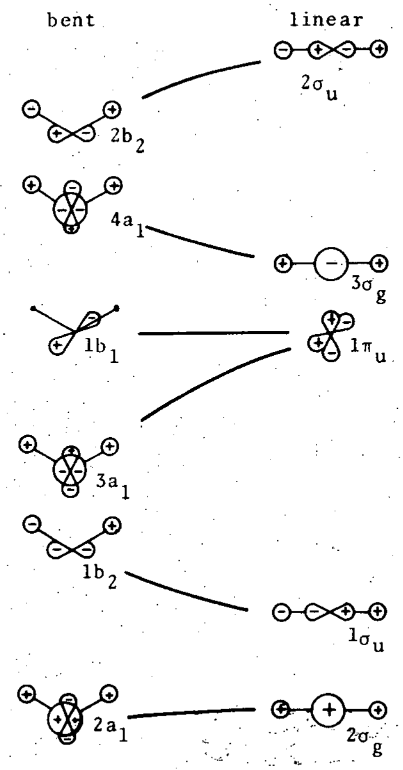

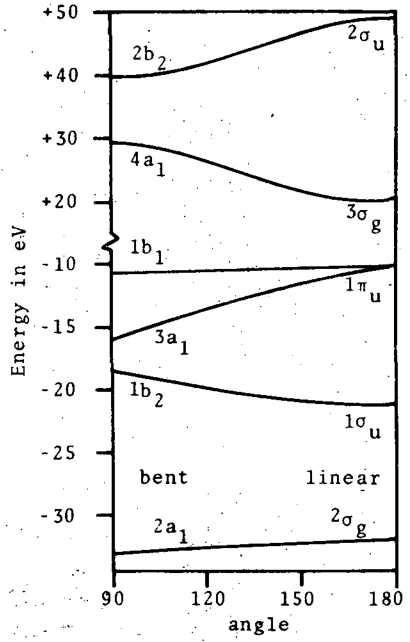

XBL 749-7264

Fig. 37a. Molecular orbitals of AH_2.

Fig. 37b. Theoretical Walsh diagram.

After the energies of the various states have been determined, the next step is to resolve the orbitals of the N^+ ion and H_2 molecule into the species of the appropriate point group, in this case C_{2v}. This is done either by using the tables provided in Herzberg[32] or merely by inspection through use of the character tables given in Cotton.[33] The σg and σu orbitals transform as a_1 and b_2 in C_{2v}. The P orbitals of the heavy atom transform as a_1, b_1 and b_2 in C_{2v} symmetry.

For the case where the N^+ ion is initially in its ground state, ^3P_g, and H_2 is initially in its ground state, $^1\Sigma_g^+$, three states arise in C_{2v} symmetry. By supplying the restriction that all the electronic must remain in orbitals that have the same symmetry as the orbitals of the reactants, three states with the following orbital occupancy are formed.

$$^3A_2 = (2a_1)^2\ (1b_2)^1\ (3a_1)^2\ (1b_1)^1 \tag{71}$$

$$^3B_2 = (2a_1)^2\ (1b_2)^1\ (3a_1)^2\ (1b_1)^0\ (4a_1)^1 \tag{72}$$

$$^3B_1 = (2a_1)^2\ (1b_2)^0\ (3a_1)^2\ (1b_1)^1\ (4a_1)^1 \tag{73}$$

The $^1a_1$ orbital, which arises from the 1s orbital in N^+, is always filled, so it will be disregarded for the purpose of this discussion.

The $^3A_2$ state is missing a bonding electron, so it is not expected to be particularly attractive. It will not correlate with any of the states that have an attractive well. O'Neil, Schaefer and Bender[34] performed a theoretical calculation on the isoelectronic system CH_2 and found that the $^3A_2$ state was repulsive by approximately 2.8 eV with respect to the reactants in their ground states. The $^3B_2$ state has one electron in the $4a_1$ antibonding orbital and will only correlate with one of the higher excited states of NH_2^+, so it will also not give access to a deep potential well.

A comparison may also be made between the energy levels of CH_2^+ and NH_2^+ by examining the result when one additional electron is put into various orbitals of CH_2^+. When C^+ initially reacts with H_2, $^2A_1$, $^2B_1$ and $^2B_2$ states will arise.[34] The $^2A_1$ state is initially very repulsive. If an additional electron is put into the $1b_2$ orbital, one would expect the $^3B_2$ state that is formed to still be repulsive. The $^2B_2$ state in CH_2^+ is slightly attractive. If an additional electron is put into the non-bonding $1b_1$ orbital one would expect the $^3A_2$ state that is formed to be fairly flat.

The $^3B_1$ state of NH_2^+ also has one electron in the antibonding $4a_1$ orbital, so it is expected to initially correlate with a higher excited state. This state may also be compared with the $^2A_1$ orbital of CH_2^+. If an additional electron is put into the $1b_1$ non-bonding orbital, one would expect the $^3B_1$ state that was formed to still be very repulsive.

The $^3B_1$ state of NH_2^+ that is formed when the reactants initially approach each other crosses the state that leads to the $^3B_1$ ground state of bent NH_2^+. By application of the non-crossing rule,[35] this leads to an avoided crossing. This implies that there is at least one adiabatic potential energy surface that provides access to the ground state of NH_2^+.

The non-crossing rule states that states of different symmetry can cross unless the direct product of the two states contains the elements of the totally symmetric representation. In other words, mathematically, the condition for crossing of two states i and j is that both

$$H_{ii} = H_{jj} \quad , \tag{74}$$

and

$$H_{ij} = 0 \quad , \tag{75}$$

where H_{ii}, H_{jj} and H_{ij} are the matrix elements of the perturbation Hamiltonian H. When the two states have different symmetries in C_{2v}, the term H_{ij} must always be zero, so there is no mixing between the states and they cross. In other words, the reaction will stay on the original potential energy surface i and the probability for avoiding the crossing and proceeding on surface j is zero.

In the example that concerns this discussion, the two states both have $^3B_1$ symmetry, so the direct product between them has elements of the totally symmetric species, A_1. This means that H_{ij} is nonzero, so there is an avoided crossing with the mixing of the two states being proportional to H_{ij}. By comparing the configuration of the incoming $^3B_1$ state (Eq. (73)) with that of the $^3B_1$ ground state (Fig. 38), one notes that the spatial configuration is quite different. This implies that H_{ij} will probably be quite small and little mixing of the two states will occur.

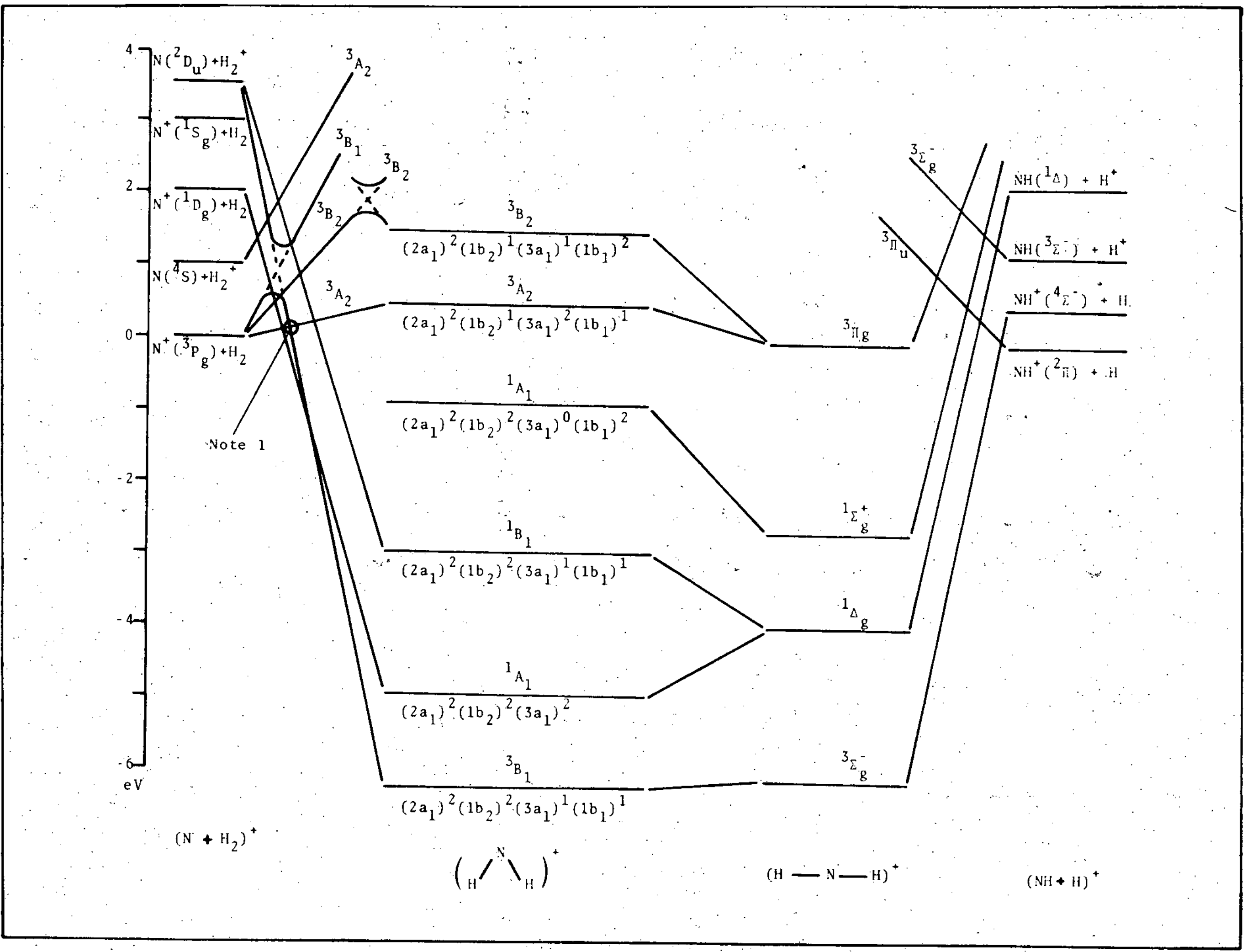

Fig. 38. C_{2v} correlation diagram. An approach of N^+ along the perpendicular bisector of the H_2 bond is assumed. Note 1. This becomes an avoided crossing when the symmetry is reduced to C_s.

XBL 749-7265

2. Deviations from C_{2v} Symmetry

Symmetry arguments concerning C_{2v} symmetry will hold only so long as the incoming N^+ ion remains on the perpendicular bisector of the H_2 molecule. If there is deviation from the perpendicular bisector, the symmetry is reduced from the C_{2v} point group to the C_s point group.

In C_s symmetry there is still an avoided crossing between the two $^3B_1$ states ($^3B_1$ becomes $^3A''$ in C_s symmetry), but there is also now an avoided crossing, when the $^3A_2$ state ($^3A_2$ becomes $^3A''$ in C_s) crosses the $^3B_1$ state. Both the $^3B_1$ and the $^3A_2$ states can then possibly provide access to the $^3B_1$ ground state of NH_2^+.

The $^3B_1$ ground state of NH_2^+ has two electrons in the $1b_2$ orbital. The $1b_2$ orbital has one nodal plane that runs through the central nitrogen atom and also extends between the two hydrogen atoms (see Fig. 37a). In C_s symmetry the orbital loses its C_{2v} symmetry, but it will still retain its basic structure of having one node between the two hydrogen atoms and containing the nitrogen atom. The only way that two electrons may end up in an orbital of this structure, other than massive rearrangement as the atoms approach, is to start off in an orbital or orbitals of this shape in the separated reactants. The ground state reactants only have one electron between the two of them that is in an orbital of the required nodal structure. This electron is in a P orbital in the N^+ ion. Therefore, the term H_{ij} will be fairly small.

The Landau-Zener formula,[36]

$$P = \exp(-\omega)$$

$$\omega = \frac{2\pi}{hv} \frac{H_{ij}^2}{|H_{ii} - H_{jj}|} , \qquad (76)$$

has been used to describe the probability of remaining on the diabatic potential energy surface; P is the probability, v, the radial velocity at the crossing point, and H, the various matrix elements of the perturbation Hamiltonian. For the case under consideration, where the spatial structure of the electron densities must change considerably to allow access to a deep well, the off-diagonal term, H_{ij}, will be small. H_{ij} will probably be small for the avoided crossings in both C_{2v} and C_s symmetry. This generally gives a probability of approximately unity of remaining on the diabatic surface. The only time that the probability of making the transition from one diabatic surface to the other is large when the velocity v is small.

The situation where the velocity v is small may arise in low energy collisions. As the velocity decreases, the probability of remaining on the adiabatic surface that leads to the deep well increases as opposed to the probability of staying on the diabatic surface which decrease. At low energies the velocity will eventually reach a low enough value to keep the trajectory entirely on the adiabatic surface.

The above situation seems to be indicated by these experiments. At the higher velocities the dynamics of the reaction seem to proceed by a spectator stripping mechanism, as shown in the work done by Gislason et al. Only at the lower relative energies done in this work is a deviation away from a direct impulsive mechanism observed. This implies that a different type of trajectory is involved at the lower energy collisions. Different overall dynamics will result as more and more trajectories start to sample the deep NH_2^+ potential well.

If the increased access to the deep well is held responsible for the change in dynamics at lower energies, the next question to be answered is why the production of a long-lived complex that results in symmetry around ±90° in the center-of-mass frame is not observed in the contour maps. This question might most easily be answered by examining the characteristics of the $(H - N - H)^+$ intermediate.

The minimum rotational period of an intermediate complex may be estimated through the use of Eq. (69). A rotational period of approximately 2×10^{-13} secs is obtained. Use of RRK theory of unimolecular reactions (Eq. (68)) to calculate the lifetime of the NH_2^+ intermediate complex yields 6×10^{-13} secs at 0.8 eV relative energy and 1×10^{-13} secs at 2.0 eV relative energy. These lifetimes are at least only approximate due to the fact that RRK theory is of doubtful accuracy at such low lifetimes.

The lifetime of the complex can be seen to vary from 0.5 to 3 rotational periods. Even if the complex were to decay statistically, which it probably does not due to the short lifetime, the angular distribution should be strongly forward peaked, as indicated by the fall off function shown in Fig. 22.

The percentage of available energy that goes into internal excitation increases dramatically with decreasing energy. This indicates that the N^+ and H_2 pass through regions in the potential surface in which strong interactions between all three particles occur. This differs from an impulsive model like spectator stripping where there is little or no interaction between all three particles i.e., there is zero momentum imparted to the spectator atom.

3. Collinear Approach

Figure 39 shows a correlation diagram for the head-on linear approach of the reactants, which then pass through a linear or near linear $(N - H - H)^+$ intermediate complex to form the products. Little or no information is known about this linear complex, which suggests that it is not a stable intermediate with a deep well.

The relative positions of the various energy levels of the intermediate were determined mainly by intuition and a rough knowledge of the energies of the individual orbitals that are present. The exact positions of the energy levels of the intermediate do not matter for the purposes of this discussion. The only thing that is really important is their symmetry, which is easily determined through the use of elementary group theory.

It can be seen from the correlation diagram that NH^+ in either its $^2\Pi$ or $^4\Sigma^-$ state can be formed directly from the reactants in their ground state. There is no intermediate that has a deep well, so that reactive scattering resulting from a long-lives complex and symmetrical around ±90° should not be observed.

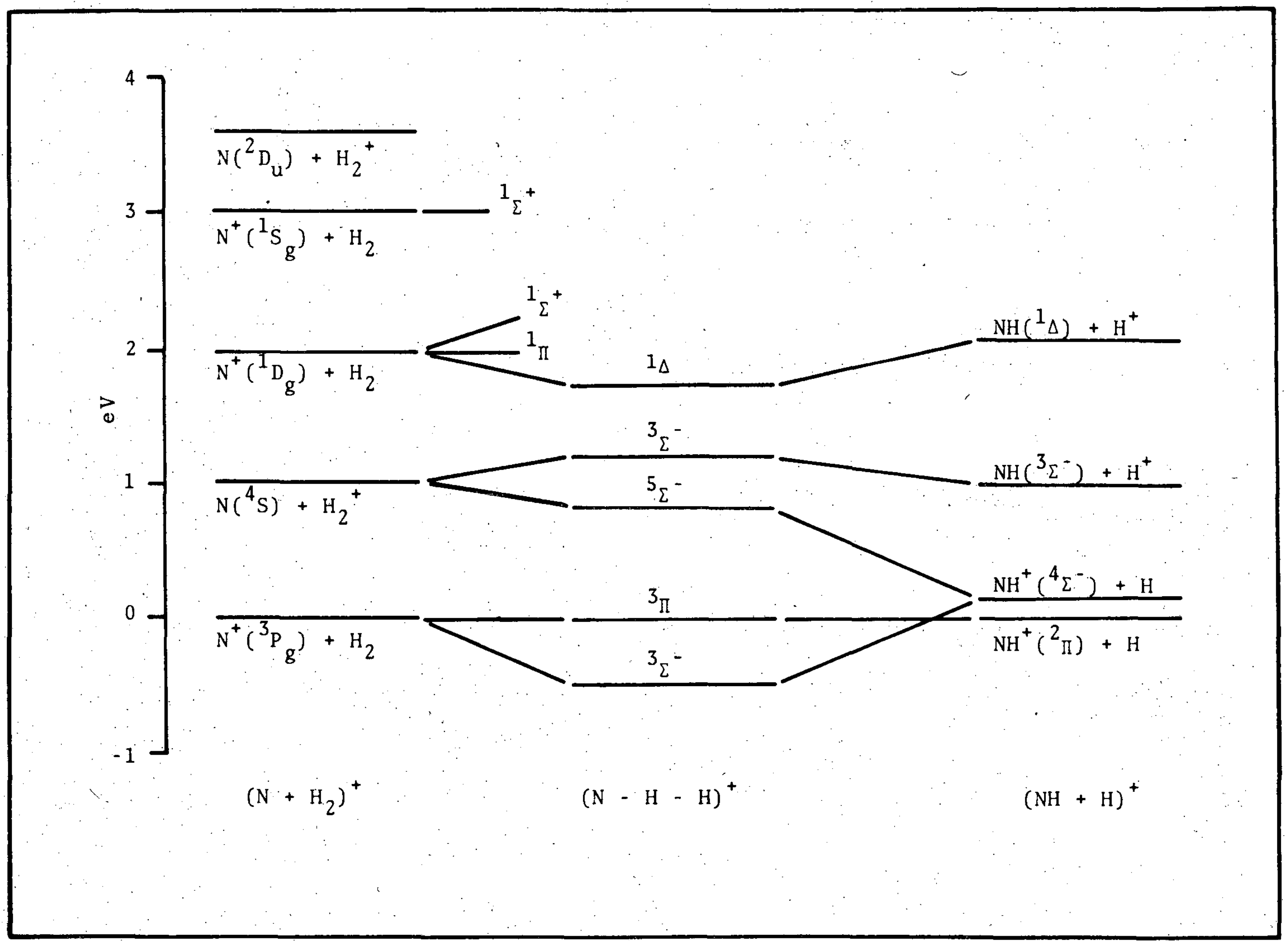

Fig. 39. $C_{\infty v}$ correlation diagram. A heat-on collinear approach of N^+ is assumed.

XBL 749-7251

D. Summary

The data that have been collected for the $N^+(H_2,H)\ NH^+$ system clearly show that the molecular dynamics for the formation of NH^+ may proceed by at least two different pathways. The actual pathway that is taken depends highly on the initial relative energy of the reactants.

Formation of NH^+ at the higher energies proceeds by a direct impulsive mechanism with the maximum intensity appearing at approximately the spectator stripping velocity. Along this pathway there appears to be very little attraction between the product ion NH^+ and the H atom. As the relative energy was decreased, a change in the product velocity distribution was observed with the distribution becoming more symmetrical around the center-of-mass. This indicates that the reaction pathway is starting to sample some type of attractive well where there is a mutual attractive force present between all three particles.

Use of electronic state correlation diagrams facilitates the explanation of the reaction dynamics. It can be seen from the correlation diagrams that there are primarily two potential energy surface pathways open to reactive scattering. One of these pathways ($C_{\infty v}$) passes over a fairly flat surface. The other pathway has access to a fairly deep (6 eV) potential well. The probability of the reaction path extending into the deep well has been shown to be velocity dependent with the probability increasing with decreasing energy. Thus the correlation diagrams in part explain the transition from a direct to an increasingly long-lived mechanism as the relative energy decreases.

This work was done under the auspices of the U. S. Atomic Energy Commission.

REFERENCES

1. P. Knewstub, Mass Spectrometry and Ion-Molecule Reactions (Cambridge University Press, 1969).
2. F. Fehsenfeld, A. Schmeltekopf, and E. Ferguson, J. Chem. Phys. 46(7), 2802 (1967).
3. E. Gislason, B. Mahan, C. Tsao, and A. Werner, J. Chem. Phys. 54, 3897 (1971).
4. W. Gentry, University of California, Lawrence Radiation Laboratory, UCRL-17691, 1967.
5. J. D. Carette and L. Kerwin, Rev. Sci. Instr. 36(4), 537 (1965).
6. L. McDowell, Mass Spectrometry (McGraw-Hill Book Co., Inc., New York, 1963), Chap. 5.
7. D. Heddle, J. Phys. E. Sci. Instr. 2, 1046 (1969).
8. S. Dushman and J. Lafferty, Scientific Foundations of Vacuum Techniques (John Wiley and Sons, Inc., New York 1962), Chap. 2,3.
9. W. Legler, Z. Physik 171, 424 (1963).
10. K. Ogilvie, R. Kittredge, and T. Wilkerson, Rev. Sci. Instr. 39(4), 459 (1968).
11. K. Wilson and R. Ivanetich, University of California, Lawrence Radiation Laboratory, UCRL-11606.
12. J. Hasted, Physics of Atomic Collisions (Butterworth, London, 1964), p. 158.
13. G. Goodrich and W. Wiley, Rev. Sci. Instr. 32(7), 846 (1961).
14. B. H. Mahan, Accounts Chem. Res. 1, 217 (1968).
15. C. Tsao, Dynamics of Ion-Molecule Reactions: N^+ and O_2^+ with Hydrogen Isotopes (Ph.D. Thesis), UCRL-19140, Dec. 1969.

16. Z. Herman, J. Kersetter, T. Rose, and R. Wolfgang, Trans. Faraday Soc. 44, 123 (1968).

17. S. Safron, N. Weinstein, D. Herschbach, and J. Tully, Chem. Phys. Lett. 12(4), 564 (1972).

18. S. Riley and D. Herschbach, J. Chem. Phys. 58(1), 27 (1973).

19. W. Miller, S. Safron, and D. Herschbach, Disc. Faraday Soc. 44, 108 (1968).

20. W. Miller, S. Safron, and D. Herschbach, J. Chem. Phys. 56(7), 3581 (1972).

21. Z. Herman, A. Lee, and R. Wolfgang, J. Chem. Phys. 51, 452 (1969).

22. G. Fisk, J. McDonald, and D. Herschbach, Disc. Faraday Soc. 44, 228 (1968).

23. G. Gioumousis and D. P. Stevenson, J. Chem. Phys. 29, 294 (1958).

24. B. H. Mahan and T. Sloane, J. Chem. Phys. 59(10), 5661 (1973).

25. Z. Herman, A. Lee, and R. Wolfgang, J. Chem. Phys. 51, 452 (1969).

26. B. H. Mahan, University of California, Lawrence Radiation Laboratory, UCRL-20550, 1971.

27. C. E. Moore, Circ. Nat. Bur. Stnds. 1(1), 467 (1948).

28. H. Liu and G. Verhaegen, J. Chem. Phys. 53(2), 735 (1970).

29. S. Chu, A. Siu, and E. Hayes, J. Amer. Chem. Soc. 94(9), 2969 (1972).

30. A. Walsh, J. Chem. Soc., 2260 (1953).

31. B. Gimarc, J. Amer. Chem. Soc. 93(3), 593 (1971).

32. G. Herzberg, Electronic Spectra of Polyatomic Molecules (Van Nostrand Reinhold Co., New York, 1963), p. 575.

33. F. Cotton, Chemical Applications of Group Theory (Interscience Publishers, New York, 1963).

34. S. O'Neil, H. Schaefer, and C. Bender, J. Chem. Phys. 55(1), 162 (1971).

35. G. Herzberg, Electronic Spectra of Polyatomic Molecules (Van Nostrand Reinhold Co., New York, 1966), p. 442.

36. L. Landau and E. Lifshitz, Quantum Mechanics (Addison-Wesley, 1965), p. 322.

TECHNICAL INFORMATION DIVISION
LAWRENCE BERKELEY LABORATORY
UNIVERSITY OF CALIFORNIA
BERKELEY, CALIFORNIA 94720